University of Catania

Department of Electrical, Electronics
and Computer Engineering

Modeling of Advanced Energy Storage Systems: the compressed hydrogen and the latent heat approaches

Emanuela Privitera

Philosophiæ Doctor Europæus

in

Systems, Energy, Computer and Telecommunications Engineering

XXXV cycle

UNICT Advisor: **Prof. Dr. Riccardo Caponetto**

CNR Advisor: **Dr. Eng. Fabio Matera**

Acknowledgements

I want to express my gratitude to my supervisor, Professor Riccardo Caponetto, for his support throughout the last three years and for all the enriching and inspiring experiences he allowed me to have. Most of the research activity reported in this thesis would not have been possible without my CNR supervisor, Dr. Eng. Fabio Matera. Deep thanks to him and his guidance in the research project. I wish to thank Hydron Engineering and all the people who work for it, particularly the CEO, Dr. Eng. Aldo Testa, for his valuable support from both industrial and human perspectives.

I wish to extend my sincere thanks to Dr. Eng. Salvo Vasta, whom I had the pleasure of collaborating with. Thanks to him, I had the opportunity to participate in the most exciting activity of the Ph.D. course: the mobility scheme in the German Aerospace Center (DLR) in Stuttgart. Furthermore, Salvo allowed me to participate through the EERA JP ES, to whom I'm grateful for the prestigious collaboration.

Lastly, I would like to acknowledge all the people I met at the DLR, in particular Dr. Dan Bauer, Dr. Andrea Gutierrez and Dr. Wolf-Dieter Steinmann, that provided me with the help I needed to finalize my research work.

I wish to thank all my friends, in particular Giulia Sapienza, Federica Spica, Giulio Greco, Daniele Maglitto, Claudio Tosto and Filiberto, for supporting me during these years of intensive effort and for the fun times spent together when the research work was too hard. Thanks also to Muk

Amiri for improving my English through lengthy discussions and enriching my life with valuable advice.

I could not have undertaken this journey without the people I met in the robotics lab, Dario Guastella, Giuseppe Sutera, Giovanna Stella, Concetta Barcellona, Emanuele Murgano, Massimo Mattina, Giuseppe Caruso and, last but not least, Dario Messina, my boyfriend; a special thanks to him for always being and helping me proofread this thesis.

I am deeply indebted to my parents, my sisters, Carlo and all my family for their understanding, and I'm grateful for their encouragement always to go on.

Abstract

Environmental degradation and the increase in the world population made it necessary to develop new green solutions in recent days. The key strategy seems to be using renewable energies, but their fluctuation over time and geography needs to realize efficient long-term storage. Researchers all over the world are working on solutions to this topic to develop cost-effective, virtually lossless Energy Storage Systems able to absorb and release large amounts of electrical energy. Accordingly, the main goal of the research activity reported in this thesis is to investigate the most promising solutions for long-term energy storage to increase the use of renewable energy.

Power-to-X-to-Power solutions convert electrical energy into different energy forms (compressed hydrogen, thermal energy, compressed air), which are efficiently storable, and reconverted into electrical energy when needed.

Large-scale hydrogen storage is a promising green solution for energy storage in balancing intermittent renewable electricity production. The Ph.D. research activity started by investigating hydrogen and its technologies, first of all, fuel cell systems. These devices convert the chemical energy of a fuel directly into electricity and are already used in many applications (e.g., hybrid electric vehicles, portable devices, marine powerplants and stationary off-grid or UPS). Fuel cells were studied firstly considering how to design a stack, then focusing on strategies for improving diagnostics. To this end, fuel cells were mathematically modeled by a Fractional-Order Transfer Function in order to identify the fuel cell behavior in a set of working points; furthermore, fuel cell fault was

analyzed for developing a neural network algorithm able to predict the degradation curve of a stack.

In addition to fuel cell systems, the research involved the Electrochemical Hydrogen Compressor to overcome problems about hydrogen's small volumetric energy density and mechanical compressors' low efficiency. The Electrochemical Hydrogen Compressor was studied, first from an electrochemical point of view, then performing the structural analysis of a system operating at 700 bar.

The third part of the Ph.D. research activity focused on Power-to-Heat-to-Power storage systems. The Latent Heat Thermal Energy Storage alternative is investigated, first modeling a phase change process from an analytical point of view, then numerically simulating the same physical problem and comparing results in order to validate the numerical model. Finally, the discharging process was simulated in order to evaluate the most efficient structure in terms of maximum average discharging power. Some Thermal Energy Storage systems allow to ideally reach roundtrip efficiency of up to 100% and are therefore potentially suitable to resolve the energy storage issue.

Contents

List of Acronyms

ANN Artificial Neural Network

ESS Energy Storage Systems

EECM Equivalent Electric Circuit Model

AIP Air-Independent Propulsion

ARMA AutoRegressive Moving Average

CNLS Complex Nonlinear Least Square

CAES Compressed Air Energy Storage

CHEST Compressed Heat Energy Storage

CSP Concentrated Solar Power

CPE Constant Phase Element

DLR Deutsches Zentrum für Luft- und Raumfahrt e.V.

EAF Electric Arc Furnace

EHC Electrochemical Hydrogen Compressor

EIS Electrochemical Impedance Spectroscopy

EOL End of Life

EERA JP ES European Energy Research Alliance Joint Programme for Energy Storage

FNN False Nearest Neighbors

FEM Finite Element Method

FOC Fractional-Order Calculus

FCT-TS Fuel Cell Technologies Testing Station

FC Fuel cells

GA Genetic Algorithm

HE Heat Engine

HTF Heat Transfer Fluid

HEA Hhigh Entropy Alloy

HT-HP High-Temperature Heat Pump

IOC Integer-Order Calculus

LH-TES Latent Heat Thermal Energy Storage

LSTM Long Short-Term Memory

ML Machine Learning

MAE Mean Absolute Error

MEA Membrane Electrode Assembly

MEPCM MicroEncapsulated Phase Change Materia

CNR National Research Council

CNR-ITAE National Research Council - Advanced Energy Technology Institute "Nicola Giordano"

NRMSE Normalized Root Mean Square Error

OCV Open Circuit Voltage

ORC Organic Rankine Cycle

PF Particle Filter

PCM Phase Change Material

PEFC Polymer Electrolyte Fuel Cells

PXP Power-to-X-to-Power

PM Predictive Maintenance

PEMFC Proton Exchange Membrane Fuel Cell

PHES Pumped Hydro Energy Storage

PTES Pumped Thermal Energy Storage

FOTF ractional-Order Transfer Function

RUL Remaining Useful Life

RES Renewable Energy Sources

SOFC Solid Oxide Fuel Cell

TES Thermal Energy Storage

UTS Ultimate Tensile Strength

UUV Unmanned Underwater Vehicle

ZEV Zero-Emission Vehicles

List of Figures

List of Tables

Chapter 1

Introduction

One of the most pressing challenges of modern society is the Energy Transition. In 2018, emissions from power were 13Gt CO2, making up 40% of global energy-related carbon emissions [1]. Global temperature rise, drought, wildfires, world population increase and high electricity demand put stress on energy infrastructures. All these causes made it necessary in recent days to develop new green solutions. The key strategy to address the effects of climate change seems to be decarbonization, gained through a mass expansion of renewables, electrification of end-use sectors and a shift from fossil to carbon-neutral liquid and gaseous fuels.

By the year 2030 (Fig. 1.1) the industry should aim to achieve the Race to Zero breakthrough outcome of at least 60% renewable energy share (in combination with fossil fuels) in power generation. Renewables have made up the majority of capacity additions for the last nine years [1]: increased integration of high shares of renewables will be enabled by greater grid flexibility through storage technology and market solutions.

With the growing share of renewables in the energy mix and greater electrification of end-use sectors, renewable must cover 100% of energy generation by the year 2050 [2]. A low-cost, reliable, resilient, and 100% zero-carbon energy system is possible with sectoral integration across energy and industry sectors [1].

Some forms of renewable energy, like wind or sunlight, fluctuate over time and geography [3], so it is not easy to realize efficient long-term storage [4]. So far, there has been a lack of location-independent, cost-effective storage on a power plant scale. Still, it is believed that Energy Storage Systems (ESS) will play a relevant role in achieving energy systems based on Renewable Energy Sources (RES). Worldwide, researchers are working on solutions to this topic to develop cost-effective, virtually lossless ESS able to absorb and release large amounts of electrical energy.

	By 2021	By 2025	By 2030	By 2040
Decarbon -ised Power	• 20% of major utilities by revenue join the Race to Zero	• 100 countries have targets for 100% clean power	• At least 60% global renewable energy share in power generation, in line with UNFCCC Race to Zero Breakthroughs	• Global decarbonised power system
Sectoral Integration	• Majority of new COVID recovery funding supports efficiency, integration technologies such as heat pumps and EVs, and demonstration and deployment of smart technologies	• Green hydrogen 25 GW capacity under construction, achieving $1.5/kg, in line with UNFCCC Race to Zero Breakthrough	• 51% of energy end-use is electrified – including electrification of 20% of passenger vehicles, 50% in buildings, and 30% in industry and heavy transport. • Green hydrogen deployment of 500-800 GW capacity, achieving $1.5/kg and cumulative investment of USD 1 trillion	• Green hydrogen and innovative production routes are mature and mainstreamed
Fossil Fuel Structural Change	• No new unabated coal power plants are being approved for development anywhere in the world • No exploration for new oil resources is required and, other than fields already approved for development, no new oil fields are necessary.	• At least 20% of major oil and gas companies have verified science based 2050 net zero targets, are taking steps to transition to low carbon business models, and reduced methane emissions by over 40% from 2020 values	• All OECD countries have successfully phased out unabated coal in their power sectors and emerging economies are well advanced in their phase out plans • Oil and gas companies have made significant progress in their transition strategies, including a 75% reduction in methane emissions (from 2020 values) • All major O&G companies have verified science based 2050 net zero targets and are have made significant progress transitioning to low carbon business models.	• All countries have phased out unabated coal power • The O&G industry is playing a critical role in scaling clean energy technologies such as, green hydrogen and offshore wind and CCS.

Figure 1.1: Milestones towards 2050. The picture is taken from [1].

1.1 Overview about Energy Storage Systems

PXP (Power-to-X-to-Power) solutions convert electrical energy into different energy forms (compressed hydrogen, thermal energy, compressed air), which are efficiently storable, and reconverted into electrical energy when needed.

Hydrogen holds a key role in the so-called green revolution as a possible energy carrier for renewable energy storage [5, 6] thanks to is high specific energy. Unfortunately, the hydrogen low energy density by volume requires highly-efficient compression methods.

Another energy storage solution (Power-to-Fuel-to-Power) stores surplus energy as synthetic fuel, such as methanol. Methanol can be produced as a net carbon-neutral fuel from green hydrogen and captured CO2. Synthetic fuels are easy to store and do not require great infrastructure investment.

Compressed Air Energy Storage (CAES) works by using electricity (during the periods of low energy demand) to compress air to high pressure and then store it in large reservoirs (typically placed in underground caverns or underground salt layers). Stored compressed air is released on demand burning in this air a small amount of fuel (typically natural gas) and expanding the combustion products through a turbine to generate electricity [7, 8].

Today, the main electrical energy storage technologies are the well-known electrochemical batteries and Pumped Hydro Energy Storage (PHES) systems. In pumped hydroelectricity storage systems, the turbine can act as a pump: in periods of low demand and high availability of electrical energy, it is possible to supply electricity to the generator which makes the turbine rotate in reverse direction and pumps the water from a lower level to an upper reservoir. The stored energy can be recovered at a later time by transforming it again into electrical energy [9].

PHES is already mature and widely used [10], but geological constraints usually limit it. CAES systems suffer geographical restrictions too and environmental concerns [10].

Storage options also include thermal-based systems. Carnot Batteries are an emerging technology for the inexpensive and site-independent storage of electric energy at medium to large scale. Also referred to as Pumped Thermal Energy Storage (PTES) or Pumped Heat Energy Storage (PHES), Carnot Battery transforms electricity into heat, stores the heat in inexpensive storage media (like water or molten salt) and transforms the heat back to electricity when required (Fig. 1.2).

Among these solutions, the Ph.D. research activity investigated two of the main innovative approaches in the energy storage field: hydrogen technologies (Fuel Cell system and Electrochemical Hydrogen Compressor)

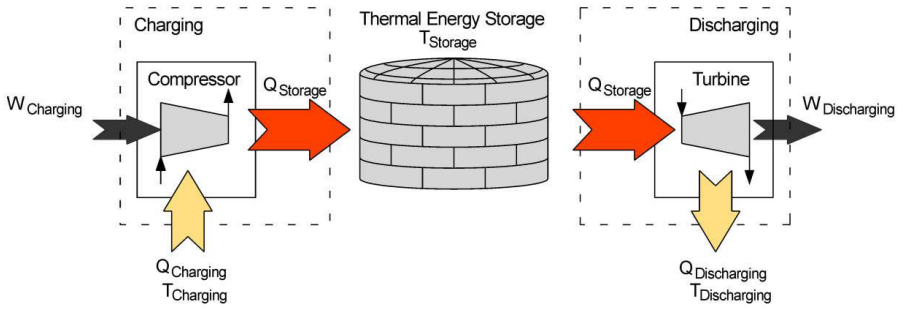

Figure 1.2: Working principle and main components of a Carnot Battery.

and the Thermal Energy Storage (TES) Systems.

1.1.1 Power-to-*Compressed Hydrogen*-to-Power

Fuel cells (FC) are taking a predominant role in sustainable mobility due to their high efficiency and zero emission - if hydrogen is used as fuel - compared to the internal combustion engine. They convert the chemical energy of a fuel directly into electricity (X-to-Power system), without thermal combustion: the waste products are only water and heat. These systems are already used in many applications (e.g., hybrid electric vehicles, portable devices, marine powerplants and stationary off-grid or UPS).

Hydrogen has a specific energy of approximately 120 MJ/kg (almost three times more than gasoline). Still, it has the lowest energy density by volume as gaseous hydrogen at room temperature and pressure [11, 12]. Except for stationary fuel cells that utilize a fixed platform to store the energy, it is essential to use highly-efficient hydrogen storage methods from both gravimetric and volumetric points of view [13, 14] to increase hydrogen usage in the future.

Hydrogen can be stored under the following states to satisfy range and weight requirements [12, 15, 16]:

1. gaseous form in highly pressurized tanks (from 20 MPa to 100 MPa);
2. liquid form in cryogenic tanks (at -253 °C);
3. cryo-compressed form (about 20 K and at least 30 MPa);
4. solid form in metal hydrides or nanostructured materials (e.g., carbon or boron nitride nanotubes, nano-magnesium-based hydrides, complex hydride/carbon or polymer nanocomposites [17]).

The compressed form is the most utilized in transportation applications. The typical pressures required to have the same range of traditional vehicles are 350 bar and 700 bar [18, 19] (hydrogen refueling stations have

to be capable to compress hydrogen up to 1000 bar [20]), with a refueling time of about 5 minutes [21].

The compression of a gas in a mechanical compressor is an adiabatic process that needs more than one stage to reduce temperature [20] and has low efficiency when used to compress low quantities of gas to high pressure. In the best case, it requires energy approximately 1.4 times above the ideal isothermal compression [22]. Furthermore, the contamination of the compressed gas is a risk for such application as fuel cells that requires a 99.99% hydrogen purity [23]. For these applications, the Electrochemical Hydrogen Compressor is more suitable: it works electrochemically, without moving parts, vibrations and noise, operating at lower hydrogen flux than traditional compressors [24]; furthermore, its process is isothermal in principle [25] and can operate in a single stage, so the EHC is simpler and more efficient than mechanical compressors [26]. While compressing, it also operates the purification of hydrogen from carbon monoxide if it is present after the reforming process [27].

Large-scale compressed hydrogen storage is a promising green solution for energy storage in balancing intermittent renewable electricity production. Elberry et al. [28] discussed different compressed hydrogen storage technologies such as storage vessels, geological storage and other underground storage alternatives, concluding that a techno-economic chain analysis is needed to establish which storage option is more suitable for a specific case.

1.1.2 Power-to-*Heat*-to-Power

When surplus electricity occurs, it is used to generate high-temperature heat that charges a Thermal Energy Storage system. The stored heat can be reconverted when electricity is required (discharging process) through a thermal power cycle.

Thermal Energy Storage systems have been successfully applied worldwide in very different applications.

Hofmühl Brewery in Eichstatt, Germany, uses the Merlin' gentle brewery' process, which requires heating for evaporation. The solar TES system replaced a gas boiler and stores pressurized hot water up to 115 °C, enabling the smart utilization of heat at different temperatures (90 °C hot water for the bottle washer, 60-90 °C preheating for brewing and domestic hot water and 45-65 °C for space heating). The TES system increased the share of renewable energy in the plant and reduced carbon emissions, energy consumption and operating costs [29, 30].

CIC Energigune (RESlag project [31, 32]) demonstrated a packed bed

TES for waste heat recovery at ArcelorMittal in Spain. Steel slag, a low-cost by-product produced in the same plant, was used as storage material. The storage volume is 3 m^3 and uses approximately 6 tons of steel slag for a demonstrator at a 1/10 scale required for the whole plant. In steel recycling, a significant amount of heat is wasted in the exhaust gases from an Electric Arc Furnace (EAF). The 1200 °C exhaust gases heat air, subsequently used to heat the packed bed TES to 700 °C. The stored heat can be used for scrap preheating, steam production or other recycling plant applications. Heat discharge stops when the material temperature drops to 40 °C, which gives a storage capacity of 1 MWh. RESlag project estimated that the total usage of 2.9 Mton slags in EU steel industrial for waste heat recovery will lead to 71 kg CO_2 reduction per ton produced steel.

The Andasol Solar Power Station in Spain [33] is a 150 MW Concentrated Solar Power (CSP) station, the first commercial plant in Europe to use parabolic troughs. During the daytime, part of the solar heat is stored using 28 500 tons of molten salt, resulting in a temperature rise of the molten salt from 290 °C to 390 °C. The stored energy ensures the continuous operation of the plant during the night and during periods of low solar radiation for up to 7.5 hours.

Molten salt TES can also be used for high-temperature industrial process heating. A modular, scalable system concept is under development by the Norwegian company Kyoto Group [34].

In general, thermal system efficiency is limited by Carnot efficiency, which defines the maximum roundtrip efficiency (typically 40% for real systems) [10]. However, a Carnot battery concept variant, called Pumped Thermal Energy Storage (PTES) system, allows to ideally reach roundtrip efficiency of up to 100% and is therefore potentially suitable to resolve the storage issue [35]. Heat pumps seem to defy the laws of thermodynamics, delivering much more than one unit of heat per unit of electrical energy consumed, using the large amount of energy stored or released when the working fluid changes phase between gas and liquid [36]. They take electricity as input not to produce heat directly (for example, in a resistive electric radiator) but to transfer thermal energy between two locations (Fig. 1.3), extracting heat from around the evaporator and concentrating heat to a higher temperature to the environment around the condenser. This characteristic allows more thermal energy to be produced than the amount of electric energy used to pump it (thanks to the heat contribution taken from the external environment) and the heat pump operates more efficiently, well over 100% [37].

Accordingly, PTES systems use surplus electricity during the charging process to increase the temperature level of a heat source through a high-

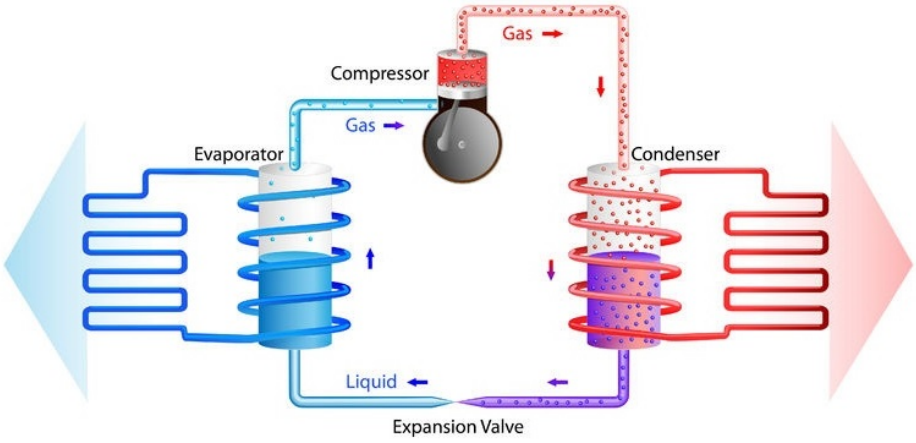

Figure 1.3: Main components of a heat pump. The figure is taken from [36].

efficient heat pump. Then, the discharging phase uses the heat from the storage to operate a thermal power cycle [38].

Inside the PTES systems group, there is the Compressed Heat Energy STorage (CHEST) system that has three main components: a High-Temperature Heat Pump (HT-HP), a high-temperature Thermal Energy Storage system (with both latent and sensible heat storage), and a Heat Engine (HE), which is an Organic Rankine Cycle (ORC).

1.2 Objectives of the research activity

The main goal of the research activity reported in this thesis is to investigate the most promising solutions for long-term energy storage to increase the use of renewable energy. These are hydrogen technologies and Carnot batteries.

FC systems were studied, firstly considering how to design a stack, then focusing on strategies for improving diagnostics. To this end, fuel cells were mathematically modeled by a Fractional-Order Transfer Function in order to identify the fuel cell behavior in a set of working points; furthermore, FC fault was analyzed for developing a neural network algorithm able to predict the degradation curve of a stack.

To overcome problems about hydrogen's small volumetric energy density and mechanical compressors' low efficiency, the Electrochemical Hydrogen Compressor was studied, first from an electrochemical point of view, then performing the structural analysis of a system operating at 700 bar.

Thanks to the opportunity offered by the EERA JP ES (European Energy Research Alliance Joint Programme for Energy Storage) Mobility Scheme,

the research about Thermal Energy Storage systems was carried out at the DLR (Deutsches Zentrum für Luft- und Raumfahrt e.V.) - German Aerospace Center, located in Stuttgart, Germany. The Mobility Scheme was developed within the CHESTER project, started in 2018 with the aim to develop an innovative CHEST system. The latent heat alternative is investigated, first modeling a phase change process from an analytical point of view, then numerically simulating the same physical problem and comparing results in order to validate the numerical model. Finally, the discharging process was simulated in order to evaluate the most efficient structure in terms of maximum average discharging power.

The remainder of the present thesis is organized as follows:

- Chapter 2 is dedicated to fuel cell systems, from the design of a fuel cell stack to the mathematical modeling of the process and the algorithm for fuel cell fault prediction;
- Chapter 3 focuses on the Electrochemical Hydrogen Compressor, from its polarization curve at different compression ratios to the investigation of possible chaotic behavior, finally analyzing the mechanical stress for a system operating at very high pressures;
- Chapter 4 describes latent heat TES system and phase change materials, simulating the phase change process first in a simplified one-dimensional problem, then in a more interesting application study;
- Chapter 5 summarizes all the results described in previous chapters, providing an overview of the three-year-long research activity. Furthermore, it proposes future research activities for all the discussed topics.

Chapter 2

Fuel Cell System[1]

Nowadays, environmental problems and the depletion of fossil fuels have led to the development of new solutions in the energy field [11]. For a long time, improved fuel efficiency has been the goal for hybrid power-train technologies. Only recently, hybrid vehicles were also considered a solution for reducing carbon-emitting, but they still need a certain amount of fossil fuels to work [12]. For Zero-Emission Vehicles (ZEV), the key is to use hydrogen as a fuel in a fuel cell system [13], which is very promising, especially if renewable sources (i.e., wind energy [41] or solar energy [42]) generate hydrogen.

A fuel cell is an electrochemical device that converts the chemical energy of a fuel (typically hydrogen) directly into electricity, without thermal combustion: the waste products are only water and heat. Fuel cells consist of two porous electrodes and catalysts (one for the anodic side and one for the cathodic ones) and a solid proton conductive polymeric electrolyte that separates the anode and cathode. These elements constitute a single cell in which electrochemical reactions occur. Multiple cells can be stacked into a fuel cell stack to give the required electric power as direct current.

The difference from a battery is that the energy is stored in the fuel, which allows separating the endurance of the system from the power. Compared with an internal combustion engine, where the efficiency can rarely be higher than 30%, a fuel cell system is not limited by Carnot cycle limitations: its efficiency can be very high (from 50% up to 95% in high-pressured systems [43]).

Fuel cells are already used in many applications (e.g., hybrid electric vehicles, portable devices, marine powerplants and stationary off-grid or UPS), but proper use of this technology is required to avoid fast degradation and reliability issues. In order to propose a valid alternative to

[1]This chapter is taken from [39]nd [40] of which the Ph.D. candidate is an author.

technologies, such as internal combustion engines, it is essential to carry out strategies for improving FC diagnostics. Electrochemical Impedance Spectroscopy (EIS) is an effective technique for understanding the degradation status of systems such as fuel cells [44] and batteries [45, 46].

Accordingly to these considerations, the Ph.D. research activity about fuel cell systems dealt with experimental impedance measurements in order to obtain a mathematical model of the fuel cell process. EIS measurements also led to a suitable fault prediction algorithm using a Long Short-Term Memory (LSTM) neural network for measuring the degradation curve (cell voltage through cycles of usage) of a fuel cell stack.

FC research was carried out with the industrial work for the company Hydron Engineering SRL, which financed the Ph.D. course together with the CNR (National Research Council). In this context, a Matlab/Simulink model was developed as a tool for designing fuel cell systems.

The chapter is organized as follows: Section 2.1 describes two of the most used techniques for fuel cell characterization, the polarization curve and the Electrochemical Impedance Spectroscopy; in Section 2.2 formulas for designing a fuel cell power module are shown, together with a brief description of the applications dealt with; in Section 2.3, a Fractional-Order Transfer Function (FOTF) is considered in order to model the fuel cell behavior in a set of electric currents. Finally, Section 2.4 shows an algorithm for fuel cell fault prediction, able to measure the degradation state and the Remaining Useful Life of a PEM fuel cell using an LSTM architecture.

2.1 Fuel Cell characterization

Polarization curve

The polarization curve is one of the most used techniques for investigating electrochemical processes. It represents the voltage output of the fuel cell for a given current density loading [47], being the most used electrochemical technique to characterize single and stacked fuel cells [48]. It describes at a glance the performance of the device under fixed operating conditions (temperature, pressure, humidity, concentration) as the efficiency is directly proportional to the voltage for a fixed current density.

In general, the steady-state polarization curve can be obtained through current as a function of cell voltage. Once the cell is connected to an electronic load, the current is registered as the voltage varies (amperometric mode). The advantage of this method is that the voltage of the cell, being the controlled input, can not assume negative values because of an excessive current output.

The example of a PEMFC (Proton Exchange Membrane Fuel Cell) polarization curve is shown in Fig. 2.1. It was obtained for a cell of $25\,\mathrm{cm}^2$ active area at the Advanced Energy Technology Institute "Nicola Giordano" (CNR-ITAE) laboratory in Messina. Generally, for increasing current density, the output voltage of a loaded cell is less than the OCV (Open Circuit Voltage), which is the nearest value to the ideal voltage (about $1.23\,\mathrm{V}$ according to the Nernst equation).

There are three distinct regions of a fuel cell polarization curve, corresponding to three polarization phenomena [49, 50]:

- at low current densities, the cell potential drops as a result of the activation polarization, which is the energy barrier that must be overcome for the start of the chemical reaction;
- at moderate current densities, the cell potential decreases linearly with the current due to ohmic losses (membrane resistance);
- at high current densities (not represented in Fig. 2.1), the cell potential drop departs from the linear relationship with the current density as a result of pronounced concentration polarization due to the too low spreading of reagents inside the electrolyte for the given current level.

The main problem of FC performance through the polarization plot is that phenomena like kinetic, ohmic and mass transfer issues, caused by degradation or operation issues (flooding, drying, etc.), are not immediately detected.

Another effective technique for electrochemical characterization is Electrochemical Impedance Spectroscopy, described in the following

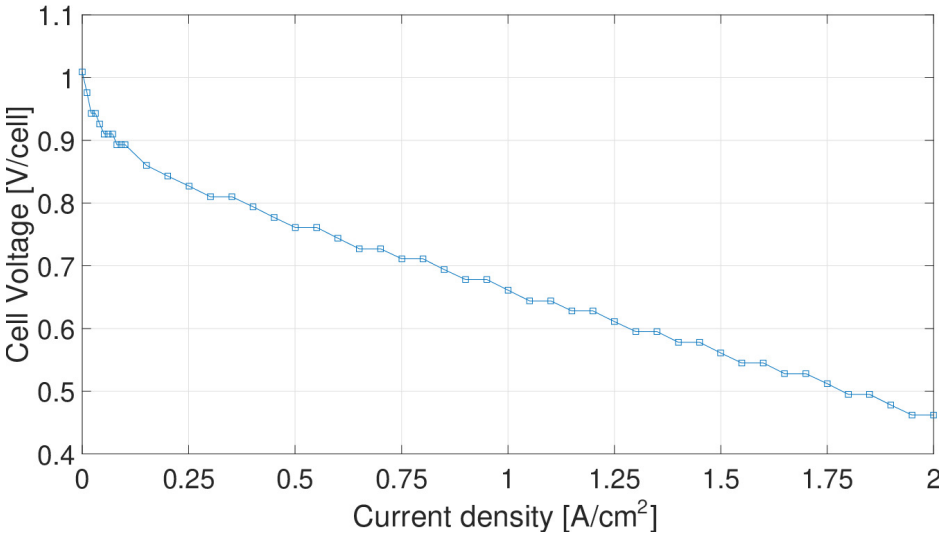

Figure 2.1: PEMFC polarization curve, obtained for a cell of 25 cm^2 active area at the CNR-ITAE laboratory.

paragraph. It can distinguish between different processes, especially when the system involves multiple-step reactions, parallel reactions or processes such as adsorption.

Electrochemical Impedance Spectroscopy

The Electrochemical Impedance Spectroscopy method has recently played an essential role in the characterization of physical and chemical phenomena (e.g., ion diffusion across membranes and corrosion phenomena) that govern systems such as fuel cells [51] and batteries [52].

The base principle of EIS is to perturb with a variable sinusoidal frequency the work-point of a fuel cell to get its response and use the impedance $Z(j\omega)$ to characterize the system. Impedance measurements can be performed by applying a sinusoidal voltage (potentiostatic method) or current (galvanostatic method) signal and measuring the corresponding dual quantity.

The impedance is obtained from voltage and current ratio:

$$Z(\omega) = \frac{E(\omega)}{I(\omega)} = \Re\{Z(\omega)\} + j \cdot \Im\{Z(\omega)\} \tag{2.1}$$

where $\Re\{Z(\omega)\}$ is the real part of the fuel cell impedance and $\Im\{Z(\omega)\}$ is the imaginary part [53].

The spectrum of the impedance can be represented by the Nyquist plot.

Commonly, EIS measurements are extracted by an equivalent electric circuit model made by resistances, capacitance, inductance and specific electrochemical elements such as the Warburg diffusion component.

To obtain representative measurements of electrochemical processes, three main conditions have to be verified:

- linearity. Typically, the current-voltage characteristic of the electrochemical systems has a non-linear shape. To consider it linear, the amplitude ΔE of the perturbation must be small; at the same time, it should be the maximum possible to reduce the noise-to-signal level on the measurement;
- stability: the system does not have significant changes during data acquisition. The choice of the frequency range can influence this condition;
- causality: the system's response is a direct consequence of the signal applied as input.

All these considerations have been taken into account in the experimental setups described in the following sections.

2.2 Fuel Cell design

A significant part of the Ph.D. research activity was dedicated to the design of FC systems. The high interest in this topic was motivated by the CNR and Hydron Engineering SRL, funders of the Ph.D. project.

CNR-ITAE develops environmentally-friendly innovative solutions. Its expertise is linked to developing components and systems for generating, transforming or storing energy, from computer-aided and model-based design to testing on complete devices. In particular, one of the research lines concerns Polymer Electrolyte Fuel Cells (PEFC) technology. The main goals are performance enhancement and cost reduction.

Hydron Engineering SRL specializes in designing, developing and constructing electricity production systems based on advanced technologies, including fuel cells, systems for hydrogen production and energy storage. These systems are used in various high-tech applications in aerospace, land and marine field: military devices/vehicles, cruises, ferries, on-shore/off-shore plants, automotive. The company's goal is to improve the performance of these systems in terms of endurance, efficiency and environmental impact.

Accordingly to the common interest, research focused on developing a Matlab/Simulink model (Fig. 2.2) to size FC stacks, starting from power requirements for a specific application. Based on the cell polarization curve obtained at the CNR-ITAE laboratory, the model calculates the consumption of FC reagents, which means the hydrogen and oxygen/air masses needed to be stored on board the platform for the system's requested endurance. A third module of the Matlab/Simulink model (still under development) contains a database of the available commercial tanks for reagent storage. It allows selecting the most suitable tank based on pressure, volume and mass technical requirements.

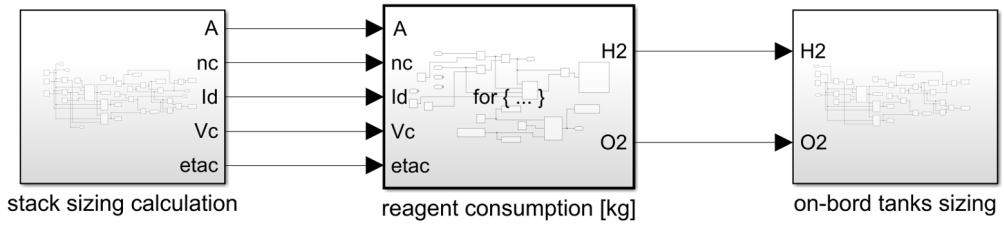

Figure 2.2: Modules of the Matlab/Simulink model for fuel cell stack design: A is the active area of the cell [cm^2], n_c is the number of cells the stack consists of, I_d is the current density [A/cm^2], V_c is the cell voltage [V] and η_c ($etac$) is the efficiency of the cell [%].

2.2.1 Fuel cell stack sizing

Engineering a fuel cell stack starts with knowing the power requirements to be met. In general, power and voltage requirements are often known depending upon the specific application.

The power P represents the expected output of the fuel cell stack. Actually, the stack sizing has to be performed also taking into account the stand-by power P_{stby} (e.g., due to auxiliaries and electronic control system), so calculations are based on the average power P_{ave}:

$$P_{ave} = P + P_{stby}$$

Recalling that the power is the product of voltage and current, it is possible to know the current through the fuel cell stack, known the average power and the nominal voltage V requirements:

$$I = \frac{P_{ave}}{V}$$

As individual fuel cells are arranged in series, the FC stack current I is the same as each individual cell current, while the FC stack voltage V is equal to the product of an individual cell voltage and the number of cells. Accordingly to this and choosing a working point I_d^*, V_c^* (corresponding to the desired efficiency η_c^*) on a reference polarization curve (Fig. 2.3), it is possible to calculate:

- the number of cells of the FC stack as:

$$n_c = \frac{V}{V_c^*}$$

- the active area of each individual cell as:

$$A = \frac{I}{I_d^*}$$

2.2.2 FC reagent consumption calculation

Because the stack current passes through n_c cells arranged in series, the mole flow rate of hydrogen, expressed in mol/s and consumed within the fuel cell stack, is [54]:

$$\dot{n}_{H_2} = \frac{I}{2F} n_c$$

where F is the Faraday constant (96 487 C/mol).

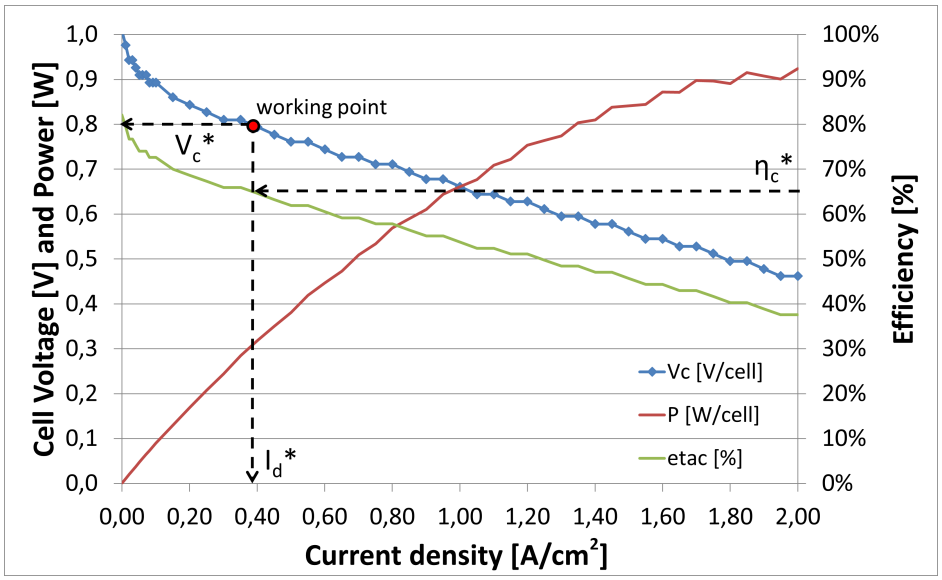

Figure 2.3: Example of a PEMFC polarization curve, obtained for a cell of 25 cm^2 active area, for fuel cell stack sizing: based on the desired efficiency η_c^*, the corresponding working point I_d^*, V_c^* is chosen for calculating the active area and the cell number.

The mass flow rate of hydrogen in g/s can be calculated as:

$$\dot{m}_{H_2} = \dot{n}_{H_2} MW_{H_2}$$

where MW_{H_2} is the molar weight of hydrogen.

The hydrogen content (expressed in g) to be supplied to the fuel cell working Δt time at P power is:

$$m_{H_2} = \dot{m}_{H_2} \Delta t$$

For AIP (Air-Independent Propulsion) applications, also oxygen needs to be stored on board. As, at the cathode, the following reaction occurs:

$$H_2 + \frac{1}{2} O2 \rightarrow H_2O \tag{2.2}$$

the stechiometric ratio of hydrogen to oxygen is 2 to 1 for H_2O, so the mole flow rate of oxygen consumed within the fuel cell stack is:

$$\dot{n}_{O_2} = \frac{\dot{n}_{H_2}}{2}$$

and the mass flow rate can be calculated as:

$$\dot{m}_{O_2} = \dot{n}_{O_2} MW_{O_2}$$

The oxygen content to be supplied to the fuel cell working Δt time at P power is:

$$m_{O_2} = \dot{m}_{O_2} \Delta t$$

2.2.3 Application studies

During the Ph.D. course, many activities were carried on about FC system development.

In 2020 Hydron Engineering and the CNR-ITAE participated to the PNRM (Piano Nazionale della Ricerca Militare, National Program of Military Research) with the project "SEAL": SistEmi Avanzati per l'aLimentazione di fuel cell a impiego sottomarino (Advanced System for Fuel Cell reagent supplying for Underwater Systems). SEAL project aims to develop an innovative power supply system in which a fuel cell stack operates downstream of an integrated chemical generator. The chemical generator can produce hydrogen and oxygen by controlled chemical reactions directly in the operating environment, continuously and on-demand, as long as it is supplied with reagents. The project, while not funded, was awarded the "Seal of Excellence" signed by the Secretary General of Defence / DNA. The project, improved with a supervision system that controls the integrated PEFC-chemical generator system, was proposed for 2021 PNRM in partnership with the University of Catania.

The Matlab/Simulink model described in Section 2.2 was used to design the FC stack for three underwater applications: replacing an Unmanned Underwater Vehicle (UUV) battery pack, powering a UUV developed inside a research project, and powering underwater laboratories for monitoring water and environmental parameters.

In general, the main components of a fuel cell power plant for AIP applications are (Fig. 2.4):

- fuel cell stack;
- H_2 and O_2 storage tanks;
- cooling system;
- recirculation pumps;
- reaction water tank.

The first study related to a UUV was carried out for a customer of Hydron Engineering in May 2020. The target was to replace the UUV battery pack with a FC power module for longer endurance missions (from 60 hours with

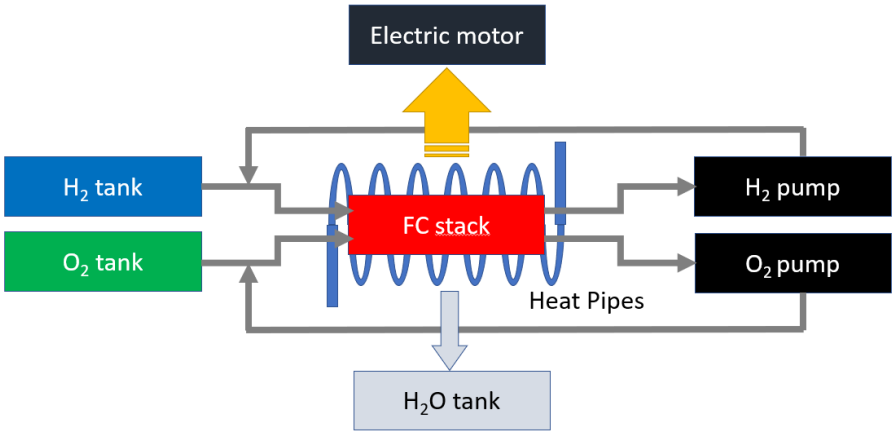

Figure 2.4: Main components of FC power plant for AIP applications.

battery-powered UUV to 90 hours with FC-powered UUV). The following steps were followed:

1. sizing the FC power module;
2. sizing storage systems for neutral buoyancy in water;
3. system integration within the available volumes (including storage systems).

Research contributed to developing a fuel cell stack for an Unmanned Underwater Vehicle inside the "TETI" project: innovative technologies for control, monitor and safety at sea [55].

TETI is a research project that involves the CNR-ITAE, other research institutes, companies and universities under the coordination of NAVTEC. The aim is to develop innovative technologies for protecting the coastal and open sea (marine environmental monitoring, navigation and risk control). These are the main objectives:

- to develop advanced sensors to be used in remote platforms and innovative buoys, linked to each other in real-time;
- to develop an integrated system for environmental surveillance and maritime traffic control;
- to develop a UUV for environmental monitoring.

As CNR-ITAE, the FC stack for the marine drone was designed, choosing an air-breathing solution to be used inside an airtight chamber. The design specifications to be met were:

- Nominal power: 850 W;
- Nominal voltage: 18 V.

TETI FC stack has 24 cells, each with a 190x95 mm^2 active area. Also, the

drawings of the bipolar plate were developed (Fig. 2.5 and Fig. 2.6).

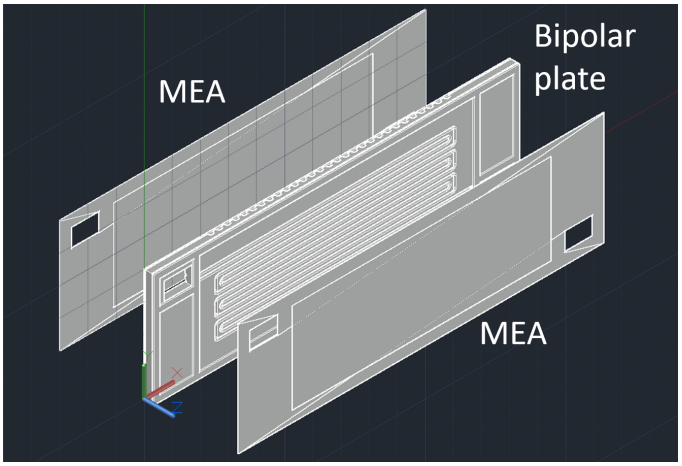

Figure 2.5: Drawing of the bipolar plate of TETI project stack (anode side).

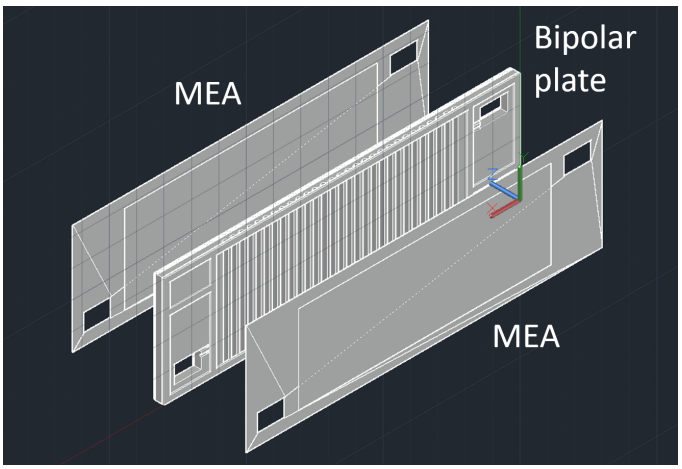

Figure 2.6: Drawing of the bipolar plate of TETI project stack (cathode side).

2.3 Fuel Cell Fractional-Order Model Via EIS[2]

The knowledge of the electrochemical processes inside a fuel cell is useful for improving FC diagnostics, and Electrochemical Impedance Spectroscopy is one of the most used techniques for electrochemical characterization.

This thesis aimed to propose the identification of a Fractional-Order Transfer Function, able to represent the fuel cell behavior in a set of working points. The model was identified by using a data-driven approach. Experimental data were obtained by testing a Proton Exchange Membrane Fuel Cell to measure the cell impedance. A genetic algorithm was firstly used to determine the sets of fractional-order impedance model parameters that best fit the input data in each analyzed working point. Then, a method was proposed to select a single set of parameters, which can represent the system behavior in all the considered working conditions. The comparison with an equivalent circuit model taken from literature was reported, showing the advantages of the proposed approach.

This section is organized as follows: firstly, state of the art is presented, then the theoretical background on Fractional-Order Calculus (FOC); Subsection 2.3.3 describes the impedance of Constant Phase and Warburg elements which are used in the literature; in Subsection 2.3.4 the experimental setup is presented; Subsection 2.3.5 describes in details the proposed FOTF and the two applied approaches in order to validate the model and to find the interpolating laws which relate the identified parameters with the analyzed working points; finally, Subsection 2.3.6 illustrates and discusses the final results and the comparison with the high-current Dhirde et al. model [56].

2.3.1 State of the art

Electrochemical Impedance Spectroscopy is an effective technique for understanding the degradation status of systems such as fuel cells [44] and batteries [45, 46].

About fuel cell systems, Huaxin Lu et al. [57] proposed a method for PEMFC fault diagnosis (drying, flooding, air starvation), using a fast EIS measurement system for online monitoring, and Zhiani et al. [58] studied the effect of MEA (Membrane Electrode Assembly) activation under low and high thermal and pressure stresses by EIS spectra.

[2]This section is taken from [39], of which the Ph.D. candidate is an author.

There are two approaches to model the impedance response of the cathode and anode FC in literature: the continuum-mechanics approach and the equivalent-circuits ones [59].

Junxiang et al. [60] developed the mechanistic EIS model consisting of a set of conservation laws using a proton-conducting SOFC (Solid Oxide Fuel Cell) button cell and associated experimental setup as physical bases, which link the multi-physicochemical processes to SOFC impedance responses. They employed a genetic algorithm to determine the model parameters so that the impedance curves predicted by the model match with the experimental data under identical operating conditions.

Yahia et al. [53], based on the equivalent-circuits approach, divided the frequency spectrum (from 90 mHz up to 12 kHz) into three bands (low, average, and high frequencies) according to the behavior of a 1200 W PEMFC and identified the model circuit parameters for 1 A current value, using a genetic algorithm.

Pan et al. [61] used EIS as an indicator of FC state of health, and combined it with an analytical equivalent circuit model, identifying the model parameters by CNLS (Complex Nonlinear Least Square) method in order to estimate future EIS and predict the voltage degradation of the cell.

In particular, Dhirde et al. [56], according to the high or low current applied to the cell, developed two equivalent circuit models of a PEM fuel cell to simulate the fuel cell's dynamic behavior and determine various performance losses by using Constant Phase Elements (CPE) and the Warburg impedance.

This thesis proposed a Fractional-Order Transfer Function to identify the fuel cell behaviour for a set of electric currents (1 A, 4 A, 5 A, 7 A, 10 A and 15 A) and a large frequency spectrum (from 0.1 Hz up to 10 kHz). Accordingly with Yahia et al. [53], the experimental data of impedance were used in a genetic algorithm to find out the impedance model parameters that best fit the input data. This preliminary work aimed to find a mathematical model able to represent the system behavior in all the considered working conditions. More specifically, this was obtained by adopting a model with a low number of parameters. As first step, the parameters identification was applied to the different working conditions to obtain the best performing parameters corresponding to each working point. With two different methods, these sets of parameters were then manipulated to obtain a unique set. The final model exploited only five parameters: two were fixed, while the others were computed as a fuel cell current density function. In this way, by simply defining the working point, it was possible to represent the fuel cell dynamics using a single model. This avoided the identification of a different set of parameters for each

working condition. A comparison with an equivalent electric circuit model from the literature [56] was performed in order to show the efficiency of the proposed fractional-order model.

2.3.2 Theoretical background on Fractional-Order Calculus

Fractional-Order Calculus can be considered an extension of the common Integer-Order Calculus (IOC). In this framework, it is possible to evaluate an $\alpha - th$ order derivatives or integral, considering $\alpha \in \mathbb{R}$. The following operator, i.e. ${}_a\mathcal{D}_t^\alpha$ with a, $t \in \mathbb{R}$ as operation limits, defines, in a compact way, the possibility to evaluate both a fractional-order derivative (if $\alpha > 0$) or integral (if $\alpha < 0$). Obviously, if $\alpha = \pm 1$ the canonical first-order derivative or integral is obtained. The fractional-order operator $\mathcal{D}^\alpha$ can be formally defined as follows:

$$ {}_a\mathcal{D}_t^\alpha = \begin{cases} \frac{d^\alpha}{dt^\alpha} & : \alpha > 0 \\ 1 & : \alpha = 0 \\ \int_a^t (d\tau)^{-\alpha} & : \alpha < 0 \end{cases} \tag{2.3} $$

In the literature, several definitions were proposed to evaluate properly the afore discussed operator [62, 63, 64]. They can be divided into two main sections, according to the type of numerical analysis that can be done, i.e., continuous-time domain and discrete-time domain. The most commonly used definitions in the continuous-time domain are the Riemann-Liouville (RL) and Caputo (CP). In the discrete-time domain the Grunwald-Letnikov (GL) [62] is adopted.

Given a time-varying function $f(t)$, the RL and CP definitions can be described by the following equations:

$$ \{{}_a\mathcal{D}_t^\alpha\}_{RL} f(t) = \frac{1}{\Gamma(n-\alpha)} \frac{d^n}{dt^n} \int_a^t \frac{f(\tau)}{(t-\tau)^{\alpha-n+1}} d\tau \tag{2.4} $$

and:

$$ \{{}_a\mathcal{D}_t^\alpha\}_{CP} f(t) = \frac{1}{\Gamma(n-\alpha)} \int_a^t \frac{f^{(n)}(\tau)}{(t-\tau)^{\alpha-n+1}} d\tau \tag{2.5} $$

where $n \in \mathbb{N} : \; n-1 < \alpha \leq n$ and $\Gamma(\cdot)$ is the *Euler Gamma* function.

Although Eq. 2.4 and Eq. 2.5 appear quite similar, the CP definition is more used because, in the Laplace domain, the initial condition still maintains a physical meaning, while with the RL one it does not occur. Analyzing deeply the CP definition in the time domain and considering a state-space

fractional-order system $x(t)$, the initial condition at $t = t_0$ is $x(t_0) = x_0$. This assumption leads to a loss of the non-locality and the infinite memory of the fractional-order operator, i.e., the future states depends on all the past state. In conclusion, some adjustments and considerations have to be made for the initial conditions of Eq. 2.5 in the state-space representation [65].

The following relation gives the GL definition:

$$\{{}_a\mathcal{D}_t^{\alpha}\}_{GL} f(t) = \lim_{h\to 0} h^{-\alpha} \sum_{j=0}^{[\frac{t-a}{h}]} (-1)^j \binom{\alpha}{j} f(t-jh) \tag{2.6}$$

where $[\cdot]$ evaluates the integer part of its argument.

Nowadays, FOC is widely used in several application fields, from describing more accurately the analyzed physical phenomena [66] to reducing the order of a system transfer function [67], from improving control performances [68] to describing economic processes [69].

In particular, taking into account the modeling of physical phenomena by means of the Equivalent Electric Circuit Model (EECM), different studies apply the FOC in order to describe the behavior of electronics components [70], electrical bio-impedance [71], or electrochemistry [72, 73]. It must be pointed out that also the fuel cell dynamics were modeled by means of FOC [61, 56] and further explanations are given in the following.

2.3.3 FC Equivalent Electric Circuit Model

FC Equivalent Electric Circuit Model tries to represent the FC components and the polarization phenomena with circuit elements, so a resistor represents the ohmic loss of the membrane and the transfer resistances of each electrode [53], a rectifying diode is associated with the electrode polarization and the load resistance can be a simple resistor or a more complex impedance, such as an inductor [74]. Other elements (inductor or Warburg element) make sense depending on the frequency range [53].

Dhirde et al. [56] describe the behavior of the fuel cell by using Constant Phase Elements and the Warburg impedance, which are now briefly analyzed.

The following impedance can describe the CPE:

$$Z(s) = \frac{1}{T_{CPE} s^{\alpha}} \tag{2.7}$$

where, in general, $\alpha \in [0; 1]$. Looking at the frequency response of Eq. 2.7, it is possible to obtain different magnitude slopes and different asymptotic phase values by simply changing the fractional-order α.

The Warburg impedance [75] models the diffusion process of charges inside the cell. The following equation can represent it:

$$Z_W(s) = R_W \cdot \frac{\tanh\left(s \cdot T_W\right)^{\varphi}}{\left(s \cdot T_W\right)^{\varphi}} \tag{2.8}$$

where R_W, T_w represent the Warburg parameters and φ is the fractional-order of the impedance.

Constant Phase Element and Warburg impedance responses are represented in Fig. 2.7. The parameters of Eq. 2.7 and Eq. 2.8 for this simulation are taken from [56] in order to simulate their response for a typical fuel cell. More specifically, the following parameters were exploited: $T_{CPE} = 0.156$, $\alpha = 0.5$, $R_W = 181.04\,m\Omega$, $T_W = 0.356$ and $\varphi = 0.67$. It is possible to notice that the CPE has a magnitude slope of about $-10\,\text{dB}$ dec and a phase constant to $-45°$ in all its frequency domains. At the same time, the Warburg impedance shows a decreasing trend in phase at very low frequencies and then it assumes a constant behavior.

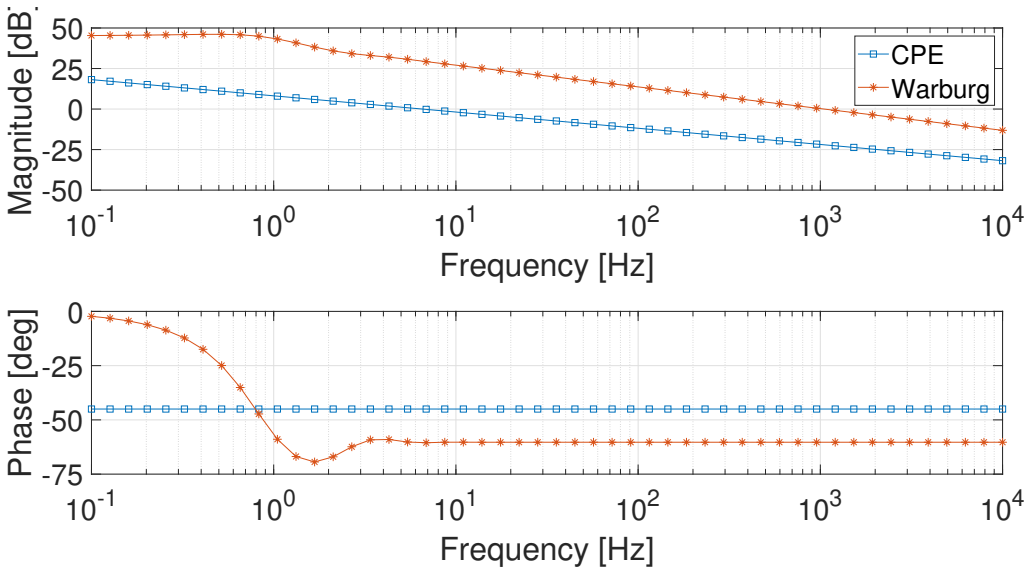

Figure 2.7: Constant Phase Element and Warburg impedance, described by Eq. 2.7 and Eq. 2.8.

These elements were exploited by Dhirde et al. in order to realize an Equivalent Electric Circuit Model able to simulate the fuel cell behavior (Fig. 2.8). Two different EECM were defined according to the value of the working point. The main circuital difference between the low-current and high-current models is represented by the presence of an inductor as in

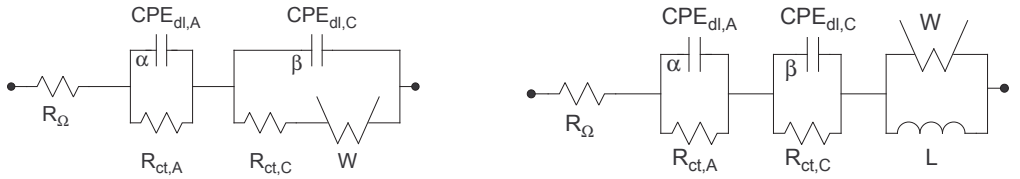

(a) Low-current EECM. (b) High-current EECM.

Figure 2.8: Dhirde et al. Equivalent Electric Circuit Models.

Fig. 2.8b: such a component, indeed, allows improving the FC modeling at high frequencies. Analyzing the other components for both the EECM of Fig. 2.8, R_Ω represents the ohmic resistance of the entire stack, R_{ct_A} and $R_{ct,C}$ the ohmic resistance for the cathode and the anode of the fuel cell, respectively. The two CPEs, $CPE_{dl,A}$ and $CPE_{dl,C}$, describe the behavior of the double-layer capacitors at the cathode and anode, respectively. In conclusion, the Warburg impedance allows defining, as said before, the charge diffusion process. These models require a large number of parameters (10 or 11) that need to be identified for each working condition.

Considering the current working points analyzed in the following, the high-current EECM depicted in Fig. 2.8b (and referred to as Dhirde et al. model) is taken as a reference with the aim of validating the proposed model.

2.3.4 Experimental setup

The experimental fuel cell impedance measurements were carried out at the CNR-ITAE laboratory using the EIS technique. Fig. 2.9 represents the experimental setup. The cell is a PEMFC in which the electrolyte is a proton-conducting membrane of Nafion® by Dupont. It has an active area of 25 cm^2 and impedance measurements come from different load values, corresponding to different points of the polarization curve.

The CNR-ITAE laboratory is provided with a specific station called Fuel Cell Technologies Testing Station (FCT-TS), shown in Fig. 2.10. It monitors the flow, temperature, humidity and pressure for anode and cathode gases, and includes an electronic DC load from Agilent Technologies [47]. The polarization curve is obtained experimentally from the LabView-based software of the FCT-TS. The experimental EIS measurements were made through the AUTOLAB PGSTAT302N, which interface is NOVA. This equipment is a high-current potentiostat/galvanostat, with a compliance voltage of 30 V and a maximum bandwidth of 1 MHz; it is specially designed for EIS

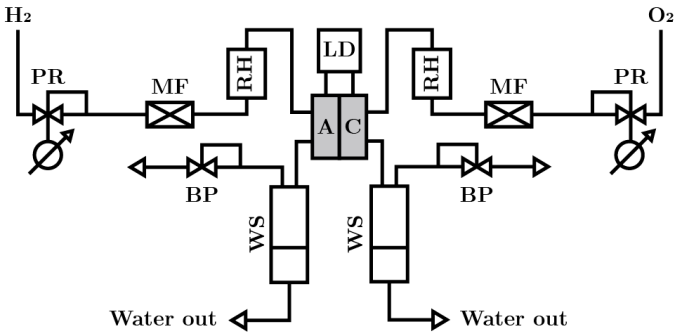

Figure 2.9: FC setup: anode (A), cathode (C), pressure regulator (PR), mass-flow controller (MF), bubble humidifier (RH), electronic load (LD), liquid water separator (WS), back-pressure (BP) [47].

measurements. The maximum current of 2 A allows analyzing a very restricted part of the polarization curve, so the PGSTAT302N was connected with the BOOSTER20A booster, which extends the maximum current up to 20 A. To perform the experiments, the cell needs that the gases coming from the FCT-TS are continuously fed to the fuel cell while the internal load is disconnected. Then, the probes of the Galvanostat were linked to the bipolar plates of the cell to draw the DC work-point and superimpose the AC signal to perturb the state. All the links are shown in Fig. 2.11 [40].

The frequency range for the EIS measurement was set from 0.1 Hz to 10 kHz, with 10 logarithmically distributed frequency values for decade, and six different points of the polarization curve, precisely for 1 A, 4 A, 5 A, 7 A, 10 A and 15 A current values for the fuel cell active area of 25 cm^2 are considered. The corresponding current densities are: 0.04 A cm^{-2}, 0.16 A cm^{-2}, 0.20 A cm^{-2}, 0.28 A cm^{-2}, 0.40 A cm^{-2} and 0.60 A cm^{-2}. Three different measurements were taken for each working point. The investigation aims to obtain a model of the process by using the obtained experimental measures. Only measurements in the range 0.1 Hz to 1000 Hz are considered in order to avoid parasitic inductive effects, that start from 1 kHz. The obtained experimental Bode diagrams are reported in Fig. 2.12.

As it can be observed from Fig. 2.12, the magnitude slope is of about −5 dB/dec, and also the phase has a different slope with respect to a canonical integer-order system. Taking into account these considerations, a Fractional-Order Transfer Function is considered in order to model the fuel cell behavior in the frequency domain.

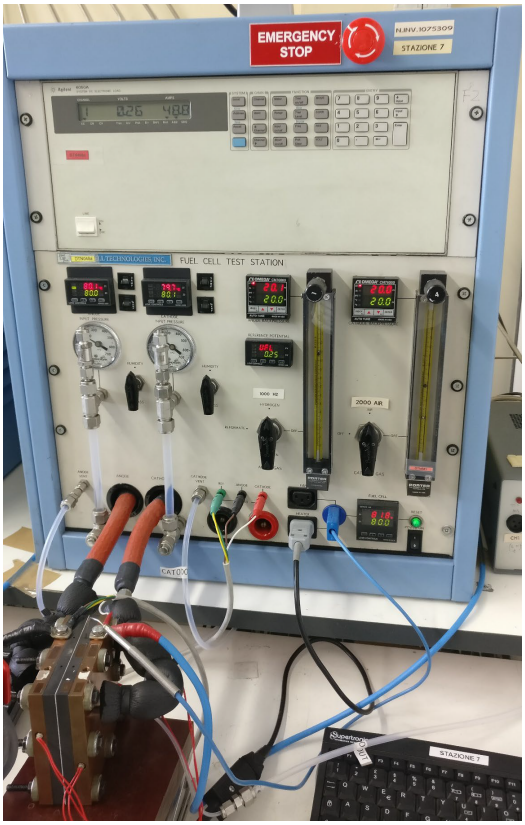

Figure 2.10: Fuel Cell Technologies Testing Station used in experiments at the CNT-ITAE laboratory.

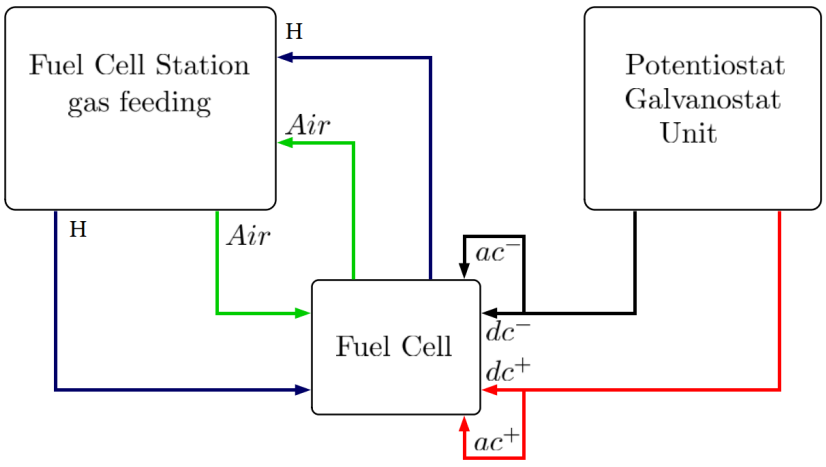

Figure 2.11: The experimental setup [40].

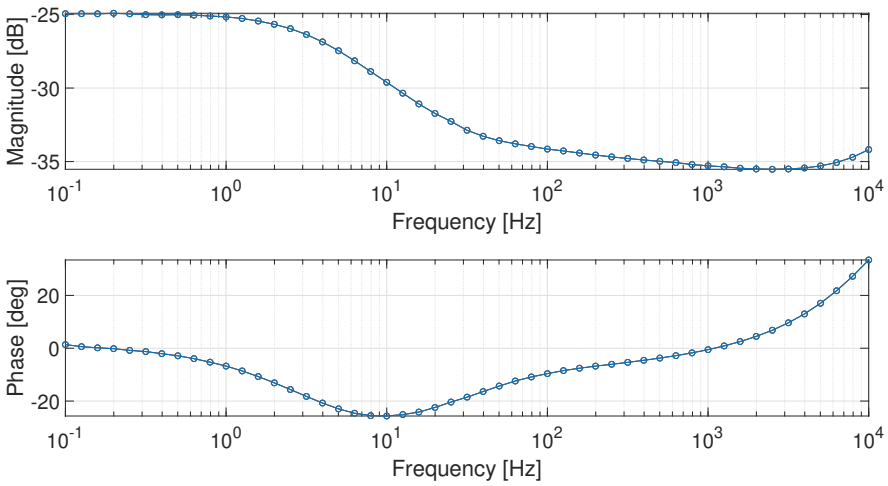

Figure 2.12: Bode diagram at the working point of 1 A in the frequency range $[0.1; 10000]$ Hz.

2.3.5 The proposed model

Analyzing the Bode diagram of Fig. 2.12, its behavior could be described by a first-order system. The proposed FOTF is reported in Eq. 2.9.

$$G(s) = k\frac{s^{\beta} + z}{s^{\alpha} + p} \tag{2.9}$$

where z and p represent the zero and pole of the system, β and α their corresponding fractional-orders and k is a gain.

To prove the validity of the proposed model, two different approaches were adopted:

- First approach: in this scenario, the first measurement (for each working point) is identified by exploiting the model of Eq. 2.9 and the other two measurements are used as validation patterns in order to verify the quality of the fitting for the proposed model. Subsequently, after collecting the acquired parameters, their relation with the corresponding operation point is investigated;

- Second approach: in this scenario, every single measurement (for each working point) is identified by exploiting the model of Eq. 2.9, and the obtained parameters are averaged and tested to verify their goodness of fit. Subsequently, a more detailed study on the relation between

parameters and the corresponding working point is performed, and the proposed interpolating laws are validated.

For both proposed approaches, the identification procedure was exploited by means of Genetic Algorithms (GA) [76, 77]. The optimization algorithm was applied, defining a proper cost function to minimize. This cost function is made up of a weighted sum of two different terms. The first one is the Normalized Root Mean Square Error (NRMSE) of the magnitude error $e_M(s)$ between the simulated and the real magnitude responses $e_M(s) = M_{ref}(s) - M(s)$. The second one of the phase error $e_P(s) = P_{ref}(s) - P(s)$, according to the following cost function $c(s)$:

$$c(s) = w_M \cdot \frac{\|e_M(s)\|}{\left\|M_{ref}(s) - \overline{M_{ref}}\right\|} + w_P \cdot \frac{\|e_P(s)\|}{\left\|P_{ref}(s) - \overline{P_{ref}}\right\|} \tag{2.10}$$

where $[\overline{\bullet}]$ evaluates the average of its argument, $\|\bullet\|$ is the absolute-value norm and $w_M = 5$ and $w_P = 20$ were empirically set in order to fit the phase behaviour of the investigated working point as better as possible.

For the sake of brevity, in the following, only the results of two working points, i.e., 1 A and 5 A, are reported. The three different acquired measurements are depicted in Fig. 2.13 and Fig. 2.14 for the working points 1 A and 5 A, respectively. They are referred to as *Meas #1*, *Meas #2* and *Meas #3*.

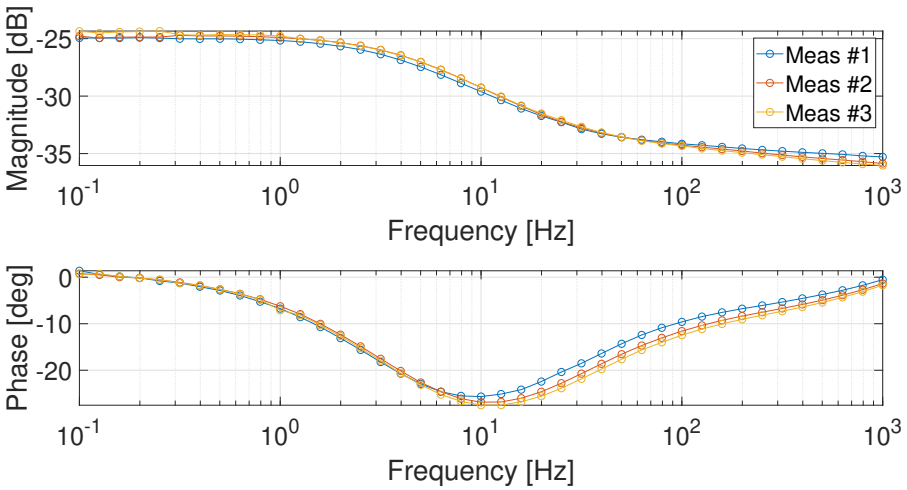

Figure 2.13: Bode diagrams @ 1 A for the three performed measurements.

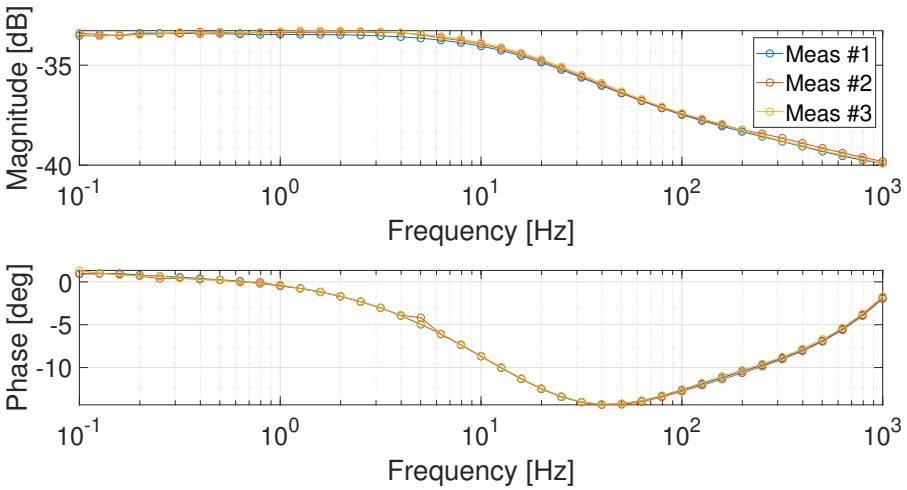

Figure 2.14: Bode diagrams @ 5 A for the three performed measurements.

First approach

The first approach scenario can be schematized by the flowchart in Fig. 2.15. It must be pointed out that, in this approach, the GA exploits the following setting variables:

- Number of variables: 5;
- Generation gap: 0.90;
- Number of individuals: 1000;
- Number of generations: 200;
- Precision: 10;
- Minimum domain range: [0 0 0 0 0]
- Maximum domain range: [110 1 180 1 0.5].

The order of parameters in the domain definition is the following one: [p, α, z, β, k]. In particular, both α and β can assume a maximum value equal to 1. In Fig. 2.16 and Fig. 2.17 the results of the identification procedure are depicted. It is possible to notice that the proposed model fits the investigated measurement well.

To validate the proposed model, the obtained system is compared with the other two measurements, taken as validation patterns. Results are reported in Fig. 2.18 and Fig. 2.19.

It is quite evident that, also for the validation pattern, the obtained models correctly describe the fuel cell behavior at the analyzed working current points. The identified parameters for each working current point were evaluated and are reported in the following (Fig. 2.20 and Tab. 2.1).

From Fig. 2.20 it can be observed that an interpolating curve can not

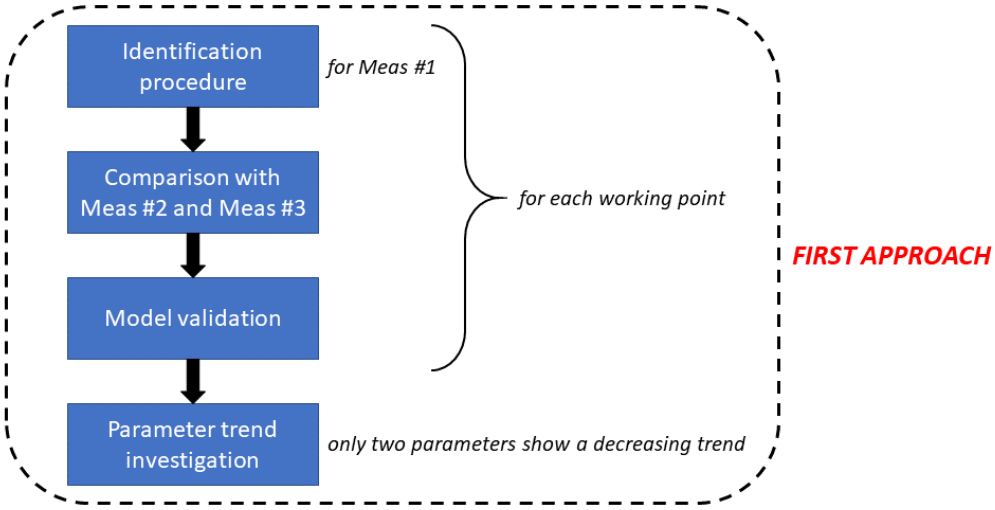

Figure 2.15: First approach flowchart.

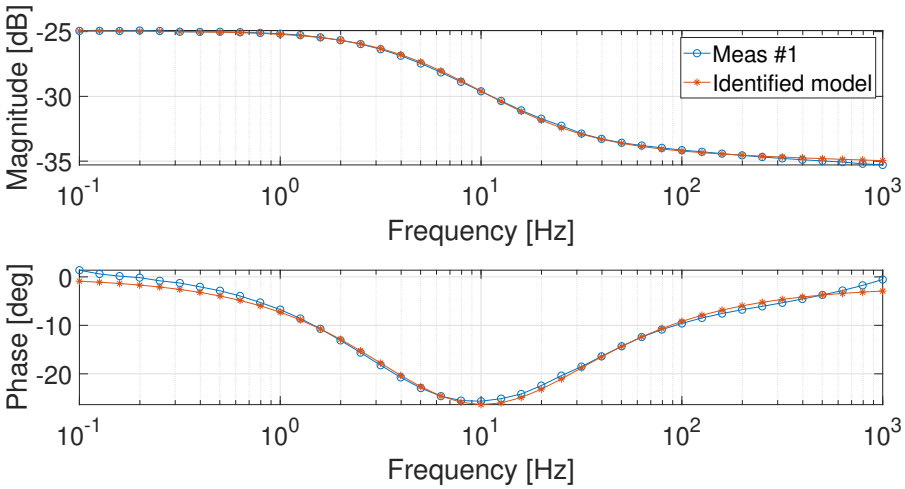

Figure 2.16: Bode diagrams of the identified *Meas #1* @ 1 A.

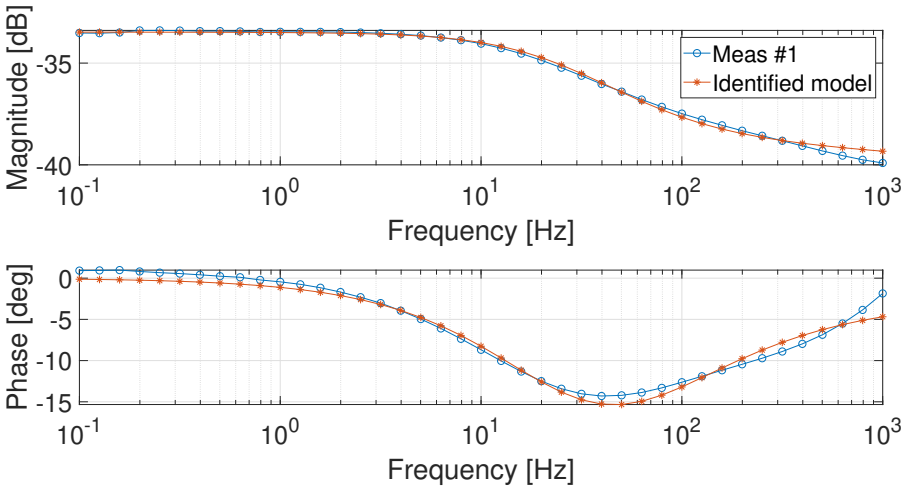

Figure 2.17: Bode diagrams of the identified *Meas #1* @ 5 A.

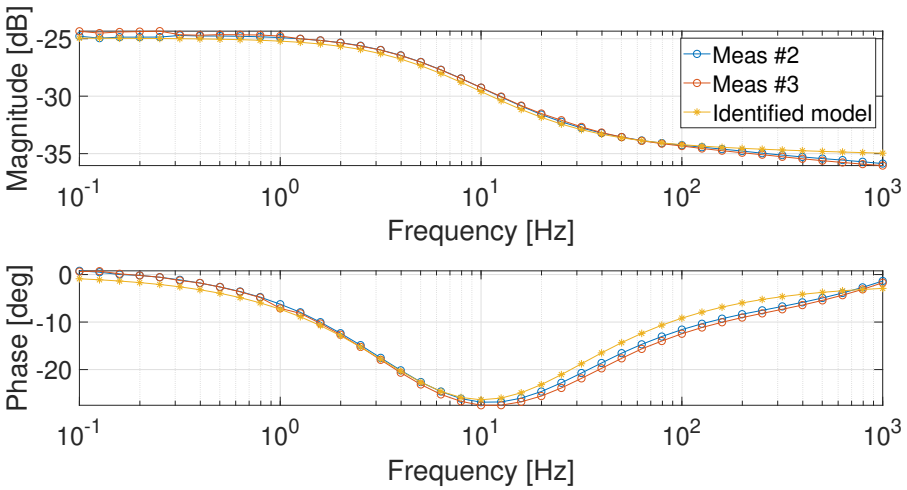

Figure 2.18: Bode diagrams of the identified *Meas #1* @ 1 A and compared with *Meas #2* and *Meas #3*.

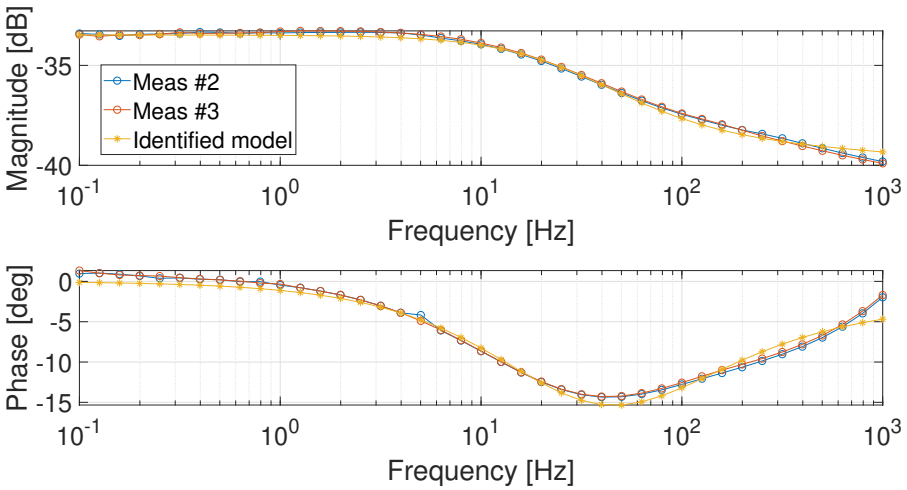

Figure 2.19: Bode diagrams of the identified *Meas #1* @ 5 A and compared with *Meas #2* and *Meas #3*.

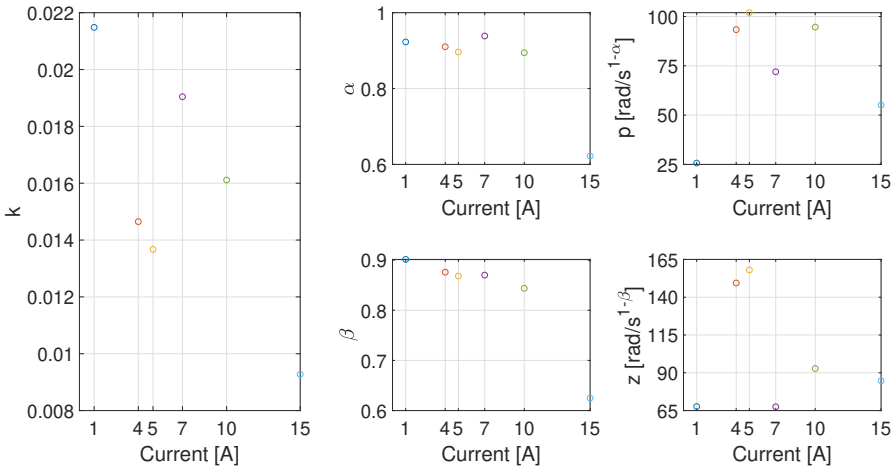

Figure 2.20: Parameters plot for each analyzed working current point.

Working point	p $[rad/s^{1-\alpha}]$	α $[-]$	z $\left[rad/s^{1-\beta}\right]$	β $[-]$	k $[-]$
1 A	25.67	0.9229	67.68	0.9014	2.148×10^{-2}
4 A	93.35	0.9102	149.4	0.876	1.465×10^{-2}
5 A	101.9	0.8965	158	0.8682	1.367×10^{-2}
7 A	71.97	0.9385	67.5	0.8701	1.904×10^{-2}
10 A	94.64	0.8945	92.81	0.8438	1.611×10^{-2}
15 A	55.11	0.6221	84.73	0.625	9.277×10^{-3}

Table 2.1: Identified parameter values for Eq. 2.9, exploiting the first approach identification strategy.

be easily obtained for k, p or z. The parameters α and β show, instead, a decreasing trend as a function of the current. Even validating the suitability of the proposed model, this approach does not lead to a single set of parameters describing the system behavior in all the working conditions.

Second approach

In the second approach, the model tested in the previous section is analyzed in detail in order to avoid parameter variability and to find, if they exist, suitable mathematical interpolating laws able to define parameters trend. Indeed, the parameter variability depicted in Fig. 2.20 could depend on the performed identification procedure. The approach can be schematized by the flowchart in Fig. 2.21.

Also in this case, the GA parameters and the cost function to minimize were evaluated as in the previous investigation analysis. For each working point and for each single measurement, the parameters of Eq. 2.9 were identified: i.e., $[\alpha_{w,i},\, p_{w,i},\, \beta_{w,i},\, z_{w,i},\, k_{w,i}]$ for the generic $i-th$ measurement of the $w-th$ working point (and the corresponding model is referred to as $S_{w,i}$). Then, their averaged values were considered: i.e., $\alpha_{w,M} = \sum_{i=1}^{3} \alpha_{w,i}/3$, $p_{w,M} = \sum_{i=1}^{3} p_{w,i}/3$, $\beta_{w,M} = \sum_{i=1}^{3} \beta_{w,i}/3$, $z_{w,M} = \sum_{i=1}^{3} z_{w,i}/3$ and $k_{w,M} = \sum_{i=1}^{3} k_{w,i}/3$ (and the corresponding model is referred to as $S_{w,M}$). The averaged parameters of the three measurements are, hence, used to describe the fuel cell behavior for the given working point. In Fig. 2.22 and Fig. 2.23 the Bode diagrams of each identified measurements (i.e., $S_{w,1}$, $S_{w,2}$ and $S_{w,3}$), the corresponding parameter-averaged-model (i.e., $S_{w,M}$) and the averaged measurement (taken as reference) are reported. As it can be observed no relevant difference exists between $S_{w,1}$, $S_{w,2}$, $S_{w,3}$ and $S_{w,M}$.

The identified parameters were collected and represented in Fig. 2.24. A

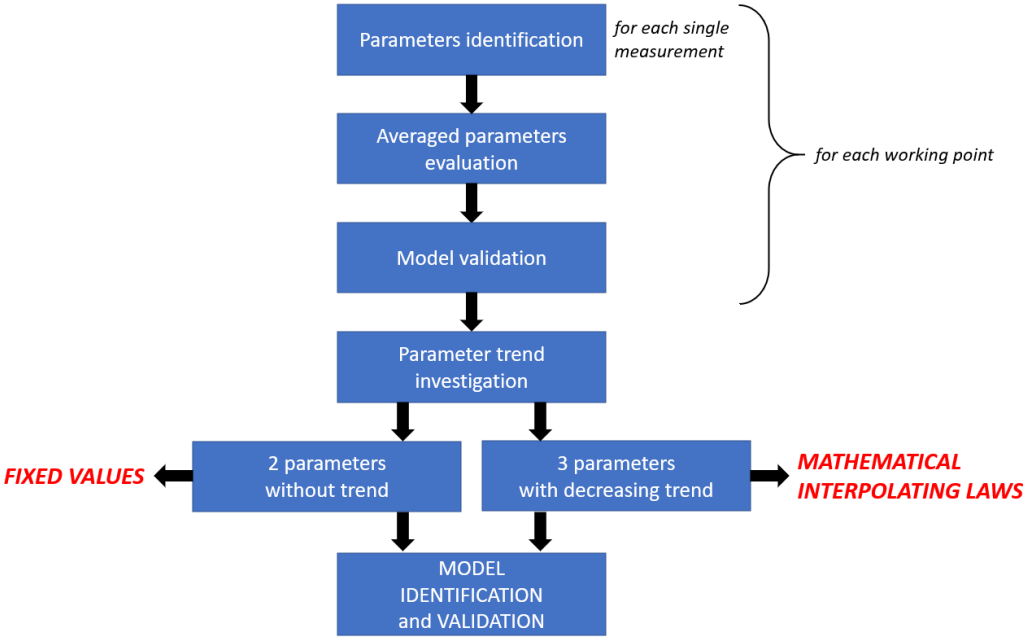

Figure 2.21: Second approach flowchart.

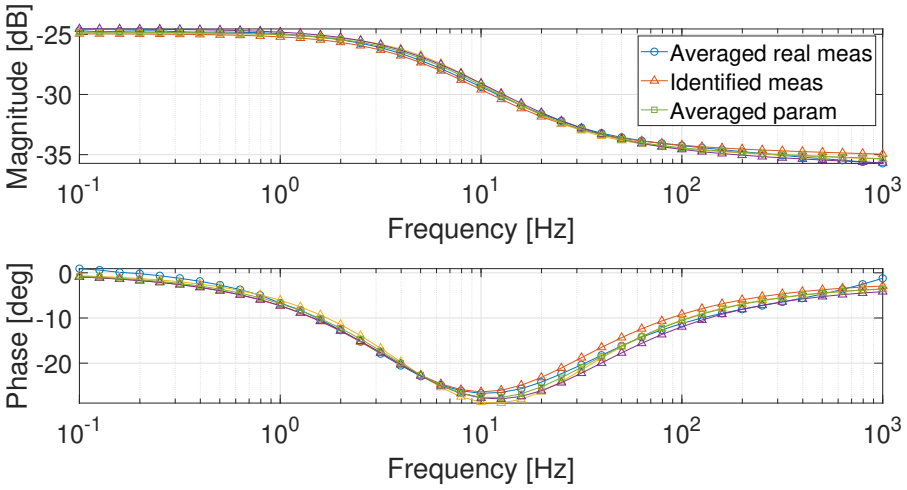

Figure 2.22: Comparison between the Bode diagrams obtained with the real averaged measurement (circle marker), the model obtained on a single measurement (triangle markers, three curves) and that obtained with the averaged parameters (square marker) @ 1 A.

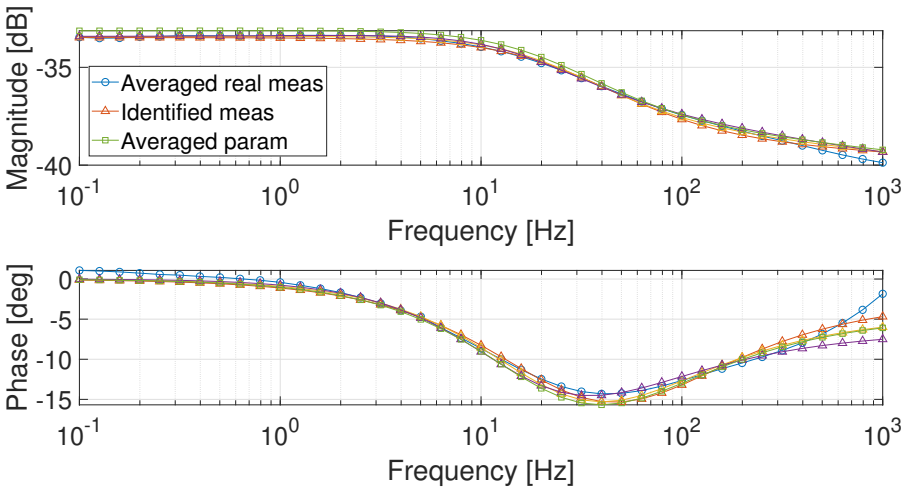

Figure 2.23: Comparison between the Bode diagrams obtained with the real averaged measurement (circle marker), the model obtained on a single measurement (triangle markers, three curves) and that obtained with the averaged parameters (square marker) @ 5 A.

decreasing trend as a function of the current value can be observed for α, β, and k.

As a first comparison, in Fig. 2.25 the measured response at 10 A and the estimation corresponding to 7 A, 10 A and 15 A, computed by using the respective set of parameters, are reported. It is possible to observe from the figure that the frequency response is qualitatively corresponding to the same transfer function for each working point, with the pole and the zero moving towards the high frequency as the current increases.

As an example, at 1 A the magnitude changes its slope at 1 Hz, at 5 A at 10 Hz, while at 15 A the slope changes at about 50 Hz. This behavior was noticed in all the working points.

Taking into account the above considerations, the model in Eq. 2.9 was again identified for each working point, fixing experimentally both the pole p and the zero z to $p = 65\,rad/s^{1-\alpha}$ and $z = 100\,rad/s^{1-\beta}$. In order to fit the experimental data, some adjustments are required for the corresponding fractional-orders α and β: indeed, their range was changed to $[0; 2]$ in order to move both pole and zero. The same cost function and the other GA parameters were also considered in the optimization procedure. Furthermore, the working point at 7 A was not considered in this second identification procedure: it is used as a validation pattern with the aim of evaluating the goodness of the interpolating laws.

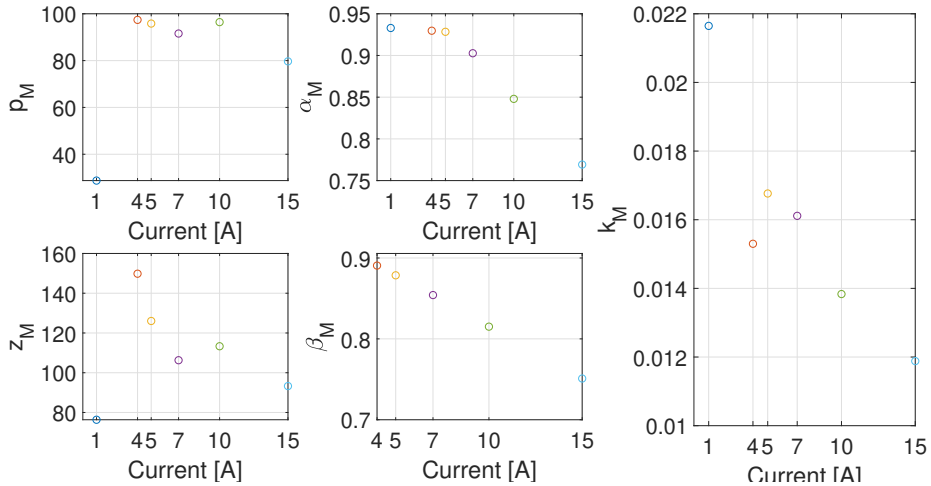

Figure 2.24: Parameters plot for each working point.

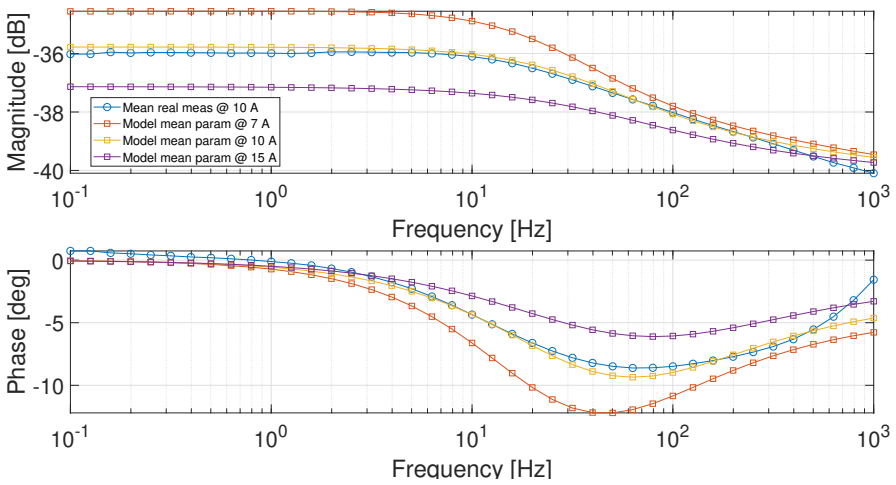

Figure 2.25: Bode diagram comparison between the averaged experimental measurement @ 10 A (circle marked) and the averaged models @ 7 A, 10 A and 15 A, respectively.

In Fig. 2.26 the three parameters which have not been fixed in this new identification procedure are represented and their values are also reported in Tab. 2.2.

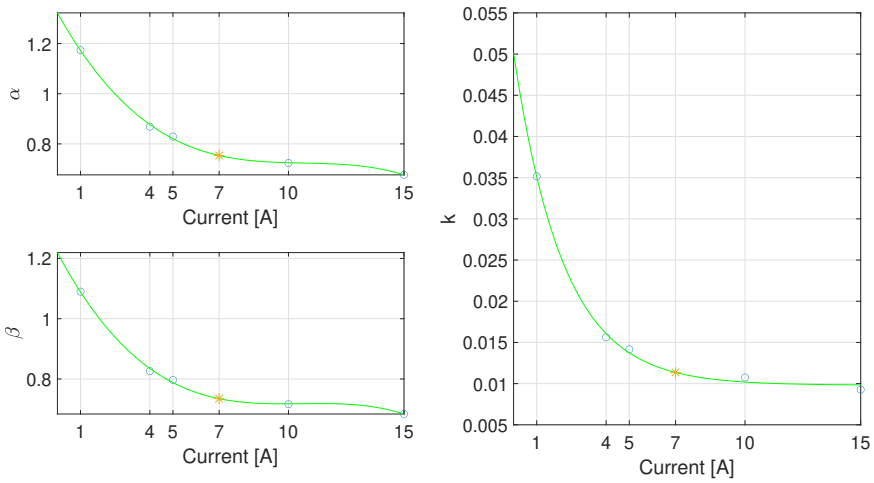

Figure 2.26: Free parameter plots with $p = 65\,rad/s1-\alpha$ and $z = 100\,rad/s^{1-\beta}$, the corresponding interpolation laws (in green) and the fitted working point at 7 A (in red).

Working point	α	β	k
1 A	1.173	1.090	3.516×10^{-2}
4 A	0.8687	0.8262	1.563×10^{-2}
5 A	0.8291	0.7969	1.416×10^{-2}
10 A	0.7236	0.7163	1.074×10^{-2}
15 A	0.6768	0.6841	9.277×10^{-3}

Table 2.2: Parameter values for the second identification procedure.

An important result can be outlined: all three parameters maintain the same decreasing trend as previously shown. The interpolating law can easily be found, as depicted in the green line of Fig. 2.26.

The interpolating laws can be evaluated as follows:

$$\alpha(I) = \alpha_1 I^3 + \alpha_2 I^2 + \alpha_3 I + \alpha_4 \tag{2.11}$$

where $\alpha_1 = -4.774 \times 10^{-4}$, $\alpha_2 = 1.527 \times 10^{-2}$, $\alpha_3 = -1.647 \times 10^{-1}$ and $\alpha_4 = 1.322$. The norm of the residuals is equal to 1.202×10^{-2}.

$$\beta(I) = \beta_1 I^3 + \beta_2 I^2 + \beta_3 I + \beta_4 \tag{2.12}$$

where $\beta_1 = -4.322 \times 10^{-4}$, $\beta_2 = 1.370 \times 10^{-2}$, $\beta_3 = -1.440 \times 10^{-1}$ and $\beta_4 = 1.219$. The norm of the residuals is equal to 1.266×10^{-2}.

$$k(I) = k_1 e^{-k_2 I} + k_3 \tag{2.13}$$

where $k_1 = 4.033 \times 10^{-2}$, $k_2 = 4.659 \times 10^{-1}$ and $k_3 = 9.810 \times 10^{-3}$. The norm of the residuals is equal to 7.08×10^{-4}.

The results of the identification procedure are depicted in Fig. 2.27 and Fig. 2.28. The Bode diagram of the model with the interpolated parameters for 7 A is reported in Fig. 2.29: the results are close to the real data and the identified model obtained from the same working point.

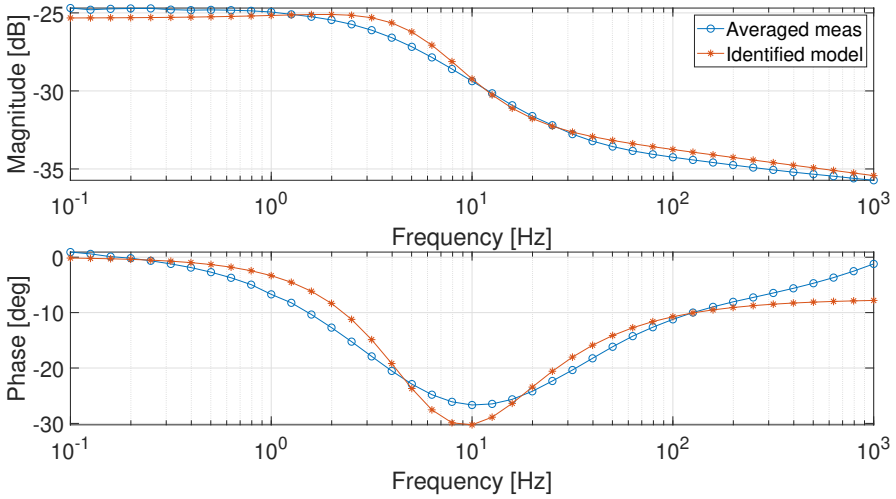

Figure 2.27: Bode diagram of the averaged measurement (circle marked) and identified model (asterisk marked) @ 1 A.

2.3.6 Model comparison

As a further comparison to support the decision to use the proposed equivalent system in Eq. 2.9, the same measurements are used to identify the parameters of the model proposed by Dhirde et al. [56], reported in section 2.3.2. In particular, the high-current model was considered because the current density of the analysed fuel cell belongs to the high-current range of the referenced model.

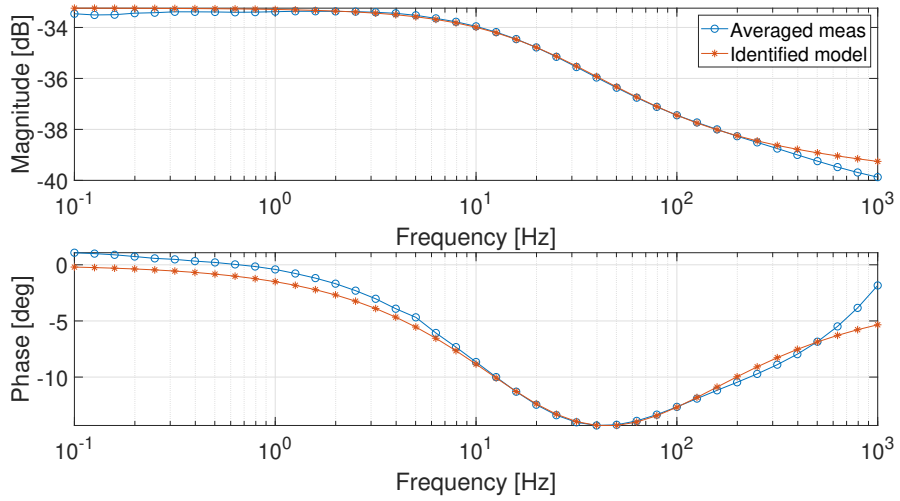

Figure 2.28: Bode diagram of the averaged measurement (circle marked) and identified model (asterisk marked) @ 5 A.

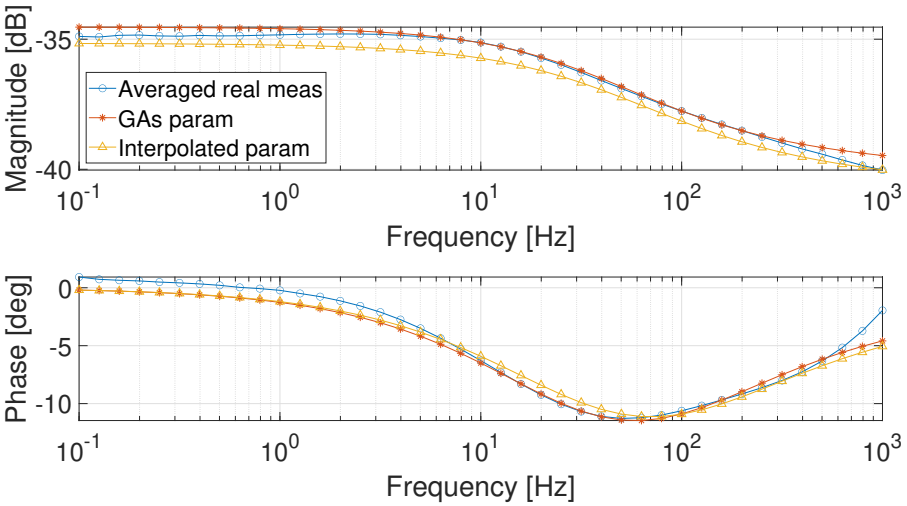

Figure 2.29: Bode diagram of the averaged real measurements (circle marked), of the identified model (asterisk marked) and the model with the interpolated parameters @ 7 A.

First of all, exploiting the same optimization procedure described in the previous sections, the high-current Dhirde et al. EECM was investigated by identifying its parameters for each working point, as depicted in Fig. 2.30.

It is possible to observe that only five parameters (i.e., R_0, R_{ctA}, R_W, T_W and α_W) follow a well-defined trend, whereas the others are scattered for the different current values. In Fig. 2.31 the model output computed with the parameters obtained for 5 A is compared with the fuel cell response at 1 A and at 15 A. From the figure, it can be observed that the parameter obtained for a given working point can not be adopted for the others. The model is able to give a good fit, however a different set of parameters should be used for each working point. Some attempts were performed to find a set of parameters able to give a good approximation on all the considered working points or to find some interpolating laws without obtaining satisfactory results.

As previously stated, the main aim of our work is to find a suitable approximated model which is able to cover all the working conditions with a low number of parameters, computed as a function of the current. The quality of the approximation should be, therefore, evaluated. A comparison between the output estimation obtained with the Dhirde et al. EECM for two working points (i.e., 1 A and 5 A), by using the two corresponding sets of parameters, is reported along with the estimation obtained by using our model in Fig. 2.32 and Fig. 2.33. Looking at the 1 A working point, it is possible to notice that the Dhirde et al. model fits better with the real data with respect to our model. A smaller difference between the two models can be observed at 5 A. As a general result, a better agreement is obtained by using our model for intermediate values of the current.

The approximation quality is evaluated using the Mean Absolute Error (MAE), reported in Tab. 2.3. MAE values under 0.5 dB and 1 deg were considered acceptable. The MAE is calculated for each current i as:

$$MAE_i = \frac{1}{n}\sum_{j=1}^{n} |y_i - \hat{y}_{i,j}|$$

where:

- n is the number of the element of the impedance vector Z_i;
- y_i is the magnitude or the phase of the Bode diagram of the averaged measurement;
- $\hat{y}_{i,j}$ is the magnitude or the phase of the Bode diagram of the FOTF or Dhirde et al. EECM Model.

As it can be observed from the table, only the MAE value computed for the phase at 1 A exceeds the fixed threshold.

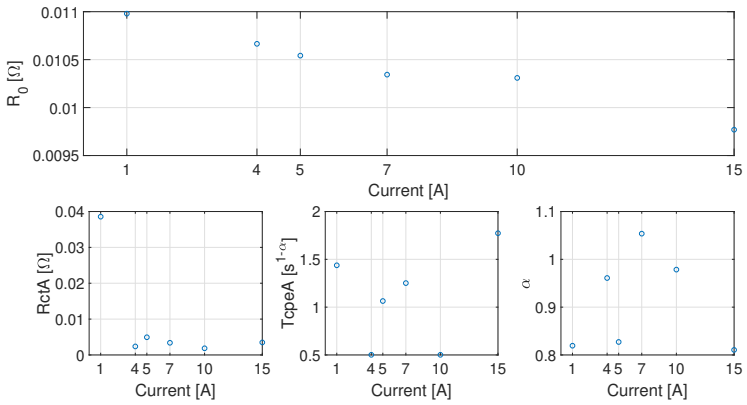

(a) High-current Dhirde et al. EECM parameters: R_0, $R_{ct,A}$, $T_{cpe,A}$, and α.

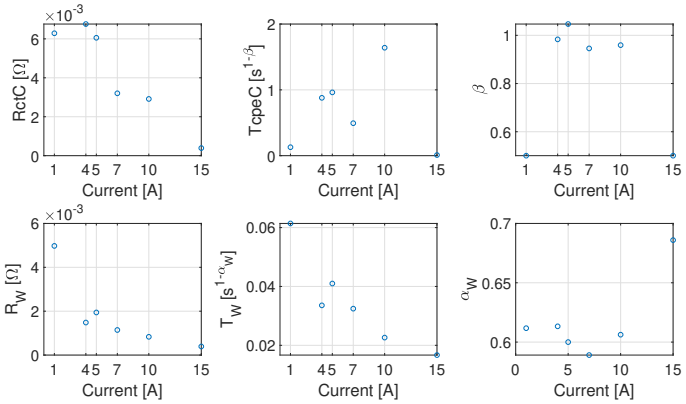

(b) High-current Dhirde et al. EECM parameters: $R_{ct,C}$, $T_{cpe,C}$, β, R_W, T_W, and α_W.

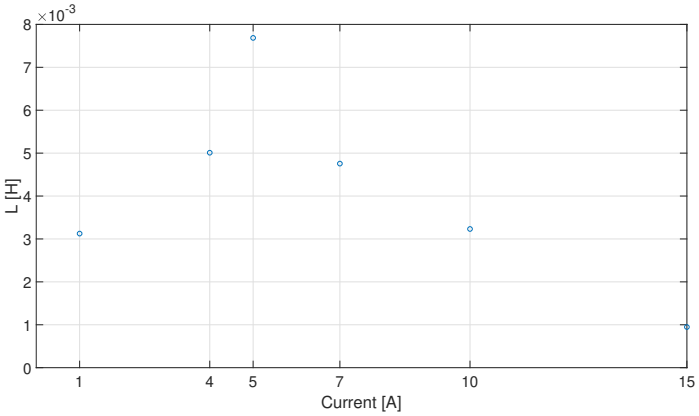

(c) High-current Dhirde et al. EECM parameters: L.

Figure 2.30: High-Current Dhirde et al. EECM parameters.

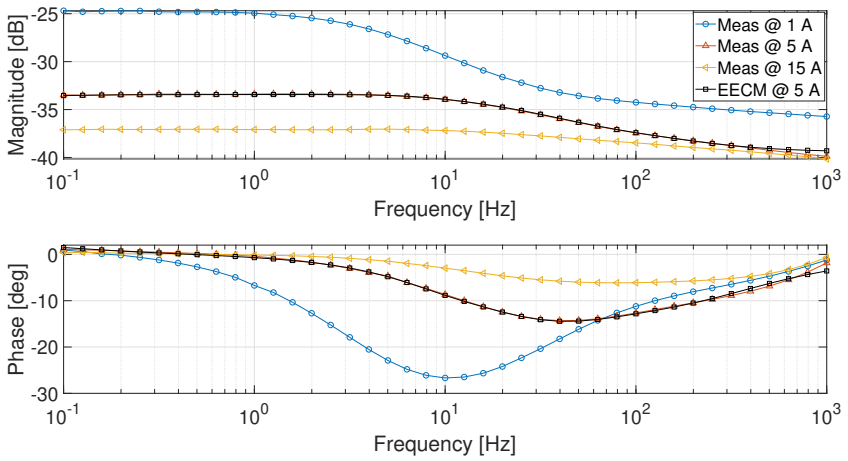

Figure 2.31: Bode diagrams of the averaged real measurements @ 1 A, @ 5 A, @ 15 A and the EECM evaluated at the current working point of 5 A.

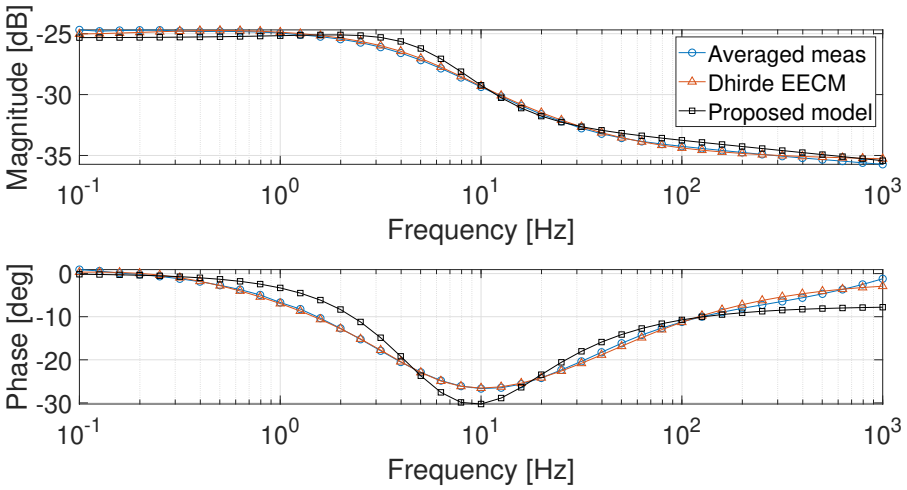

Figure 2.32: Bode diagram of the averaged measurement (circle marked), the Dhirde et al. model (triangle marked) and the proposed model of Eq. 2.9 (squared marked) @ 1 A.

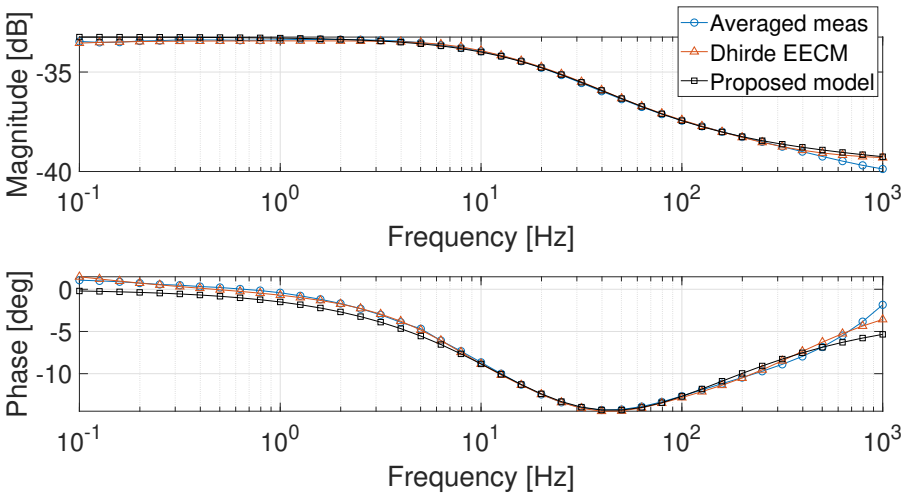

Figure 2.33: Bode diagram of the averaged measurement (circle marked), the Dhirde et al. model (triangle marked) and the proposed model of Eq. 2.9 (squared marked) @ 5 A.

Working point	**Mean Absolute Error**			
	|Eq. 2.9| [dB]	∠Eq. 2.9 [deg]	|EECM| (Fig. 2.8b) [dB]	∠(EECM) (Fig. 2.8b) [deg]
1 A	0.4271	2.1351	0.1281	0.3841
4 A	0.1398	0.7032	0.0677	0.2515
5 A	0.1169	0.7094	0.0715	0.2242
7 A	0.3877	0.7058	0.0488	0.2011
10 A	0.1567	0.6024	0.0522	0.1623
15 A	0.1117	0.4852	0.0523	0.2116

Table 2.3: The Mean Absolute Error, calculated for each current. For 7 A MAE was calculated using the interpolating laws described in Eq. 2.11 - Eq. 2.13 for the FOTF estimation.

Summarizing all the aforementioned considerations and results, the model of Eq. 2.9 can be considered as a good approximated model, able to describe fuel cell behavior for all the currents belonging to the interval 1-15 A, without the need to estimate a different set of parameters for each working point.

2.4 LSTM architecture for Fuel Cell fault prediction[3]

The reliability of fuel cell applications is essential to make this technology the most suitable choice between internal combustion engines or battery-powered vehicles. The thesis aimed to find a suitable fault prediction algorithm using a Long Short-Term Memory neural network able to measure the degradation of a fuel cell stack using a few and fast point-to-point measurements obtained by Electrochemical Impedance Spectroscopy. The final goal was to predict the fuel cell degradation curve, i.e., the health status, represented by the cell voltage through cycles of usage.

This section is organized as follows: firstly, state of the art is presented; Subsection 2.4.2 describes the experimental measurements and explains how the degradation process is simulated; in Subsection 2.4.3 the Long Short-Term Memory architecture and the learning phase are illustrated.

2.4.1 State of the art

Predictive Maintenance (PM) has gained a significant role in the fourth industrial revolution thanks to its capability to reduce the cost of maintenance, fault events and repair stops, increasing productivity and overall profits. It continuously monitors a machine or process integrity, collecting a large amount of data extracted through sensors along an industrial production line. In this way, the PM can detect early failures through predictive tools based on historical data, like Machine Learning (ML) techniques, allowing maintenance to be performed only when needed [78].

Machine Learning, and in particular deep learning, is widely used in literature to develop process models, known as Soft Sensor [79, 80], which can be used for process monitoring and fault detection applications. It is also used for smart grid development [81], for condition monitoring in wind turbines [82] and for improving the operational performance of building energy systems [83].

Industry 4.0 has to cope with the new environmental constraints in the field of clean energy production. In this view, fuel cells are taking a predominant role for their high efficiency compared to internal combustion engines. Still, they must be carefully operated and monitored to avoid faults and reliability issues. Knowledge of a stack's degradation status is helpful for an improvement strategy or diagnostic analysis.

[3]This section is taken from [40], of which the Ph.D. candidate is an author.

In the literature, many studies aimed to experimentally identify fault indicators for diagnosis purposes through the EIS method to optimize FC performance and reduce their degradation. Araya et al. [84] tested various faults (reactant starvation, flooding, drying, CO and H_2S poisoning) to identify the faults through the frequency spectrum; for example, flooding and drying are detected at the opposite ends of the frequency spectrum due to the effect of drying on the membrane conductivity and the blocking effect of flooding that constricts the reactants' flow. Huaxin Lu et al. [57] developed an online fault diagnosis algorithm for PEMFC based on a fast EIS measurement to reduce the measurement cost and time. Other studies go beyond: once caught, the degradation status of a fuel cell system was modeled through neural networks. An interesting review, made by Lin-Kwong-Chon et al. [85], introduced various adaptive neural control on FC systems; these methods concern fault diagnosis and active fault tolerant control strategy. Thanks to the Artificial Neural Network (ANN), Belmokthar et al. [86] demonstrated the capability of a neural network to model a PEMFC stack voltage characteristics. Jeppesen et al. [87] implemented a fault detection strategy involving EIS and neural networks to identify different types of faults on a FC system; they found some invariants to the degradation over time and isolated them through feature selection.

The prediction of the Remaining Useful Life (RUL), intended as the complement to the End of Life (EOL) of a device, can be approached using the Long Short Term Memory architecture to understand the long-term dependency in the modeling process, achieve a prediction on the EOL and schedule intelligent maintenance. In the FC field, according to the literature, there are some methods for predicting the health state and the RUL of a PEMFC. Prognostic approaches can be roughly divided into two categories: model-based and data-driven methods. To overcome the limitations of these methods, Ma et al. [88] developed a fusion strategy between the Particle Filter (PF, model-based) technique and LSTM architecture to improve the accuracy and precision of the forecasting. In a further research work [89], they used the cell voltage (i.e., the state of health) as FC degradation curve and a LSTM-ARMA (AutoRegressive Moving Average) model to reconstruct the degradation curve from the measured cell voltage over 400 h of degradation test; the voltage cell is represented through a time-series data stream and was split into a different learning/test sections to get multiple results of the prediction performance.

The thesis aimed to identify an algorithm able to measure the degradation state and the RUL of a PEMFC by using only a historical EIS dataset and an LSTM neural network on a simulated FC stack, starting

from real measurements on a 25 cm^2 single cell. While the dataset of EIS and polarisation curves have been obtained by extrapolation of a real dataset of a real single PEMFC cell, the degradation process was simulated from literature models to obtain a data set suitable for the LSTM architecture, starting from healthy data acquired from a fuel cell at the CNR-ITAE laboratory.

2.4.2 Experimental measurements and simulation of the degradation process

Internal processes lead to small but steady performance degradation when a fuel cell is used over time. The first step toward a data-driven degradation estimation approach is to acquire a suitable dataset to train the LSTM network. In this paper, due to the huge time-consuming process of acquiring the whole data of the degradation process, a semi-simulated approach was used to get a dataset able to describe the FC behavior along its lifetime, including the degradation process [90, 91]. The flowchart in Fig. 2.34 represents the main steps of the procedure.

Polarization curve

The polarization phase was implemented through the FCT-TS, shown in Fig. 2.10. For each polarization phase, a standard condition was chosen; the summary of them is reported in Tab. 2.4.

Table 2.4: Table of set points for polarization.

Cathode flow parameters			
Stoic flow -	Set point sccm	B.-pressure bar(g)	T. hm/pre-ht/plug ℃
2	832	2.0	80
Anode flow parameters			
1.5	260	2.0	80

The polarization curve was registered after the break-in procedure (Fig. 2.35). Tab. 2.5 shows the indicators of the main status of the FC: the OCV represents the open-circuit voltage, the Z range is the impedance measured at a fixed frequency (4 kHz) by an Agilent multimeter, and Current/Voltage ref is the test work-point under load. These parameters were followed constantly after some test cycles to keep track of the cell status and to partially "reset" the MEA after some stressing measures like the EIS itself.

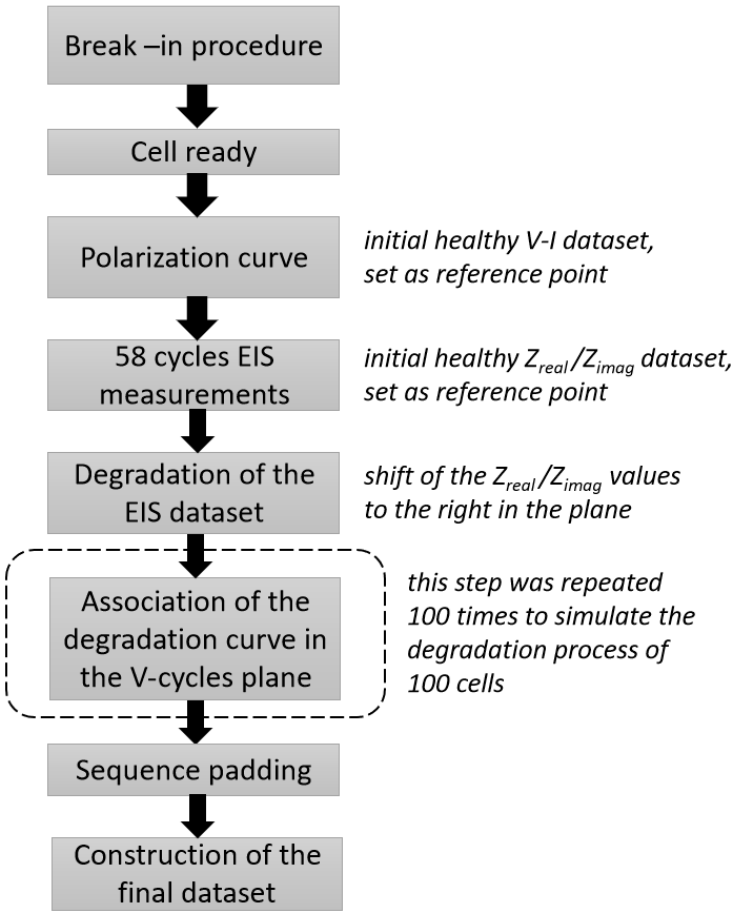

Figure 2.34: The main steps for constructing a suitable dataset to train the LSTM network.

Table 2.5: Stable values after the break-in phase.

S25 - 15 cell/ MEA CDL 129+NR212 n. 1			
OCV V	Z range mOhm	Current ref A	Voltage ref V
0.99	4.2 - 5.3	25	0.63 - 0.61

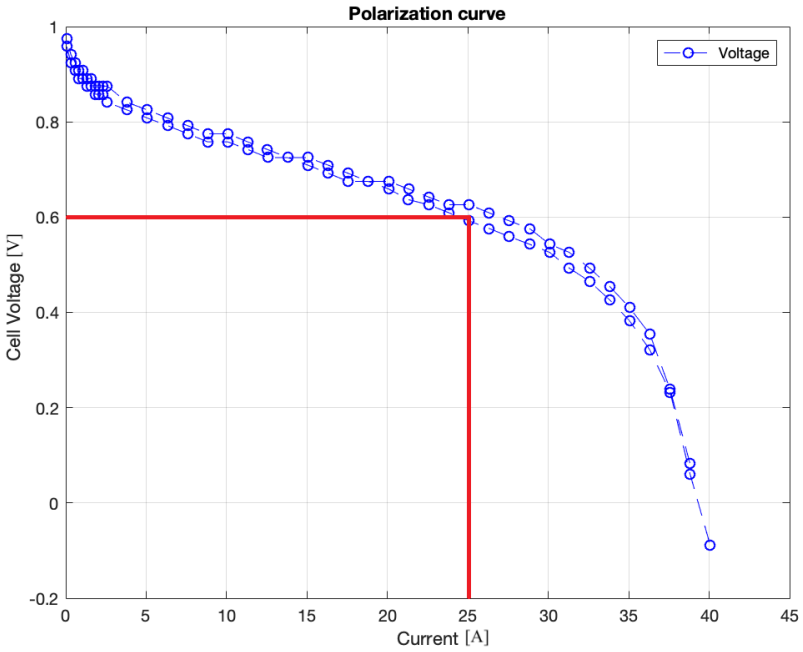

Figure 2.35: Polarization curve of a healthy fuel cell.

Electrochemical Impedance Spectroscopy measurements

Once a work-point is chosen (4 A was chosen for our test), a sinusoidal input with fixed amplitude and frequency is superimposed and Z_{re} and Z_{im} part of impedance are measured; then, the frequency is decreased to obtain the frequency response; in our case, the chosen range started from 10 kHz down to 0.1 Hz acquiring 10 points dec, then the process is repeated until the entire Nyquist plot is obtained.

The settings are shown in Tab. 2.6 and a total of 58 cycles of measures have been recorded (Fig. 2.36). It is important to note that each EIS datafile in output from NOVA was composed of 16 rows of frequency measures, which involve Z_{real}, Z_{imag} values. During the whole 58 cycles of EIS, the status of the cell is healthy; in fact, the monitored values remained mainly unchanged during the measuring process; the little differences between the real part of each cycle of measurements in Fig. 2.36 are the results of the perturbation over the cell by EIS, while this stress can be completely recovered after a short steady-state operation of the cell.

The actual EIS data recording is used as a starting point to characterize the degradation process of the FC.

Table 2.6: EIS settings in 10 kHz - 0.1 Hz range

Measures/decade n.	Signal -	Amplitude A_{rms}	N. of cycles -
10	sine	0.4	58

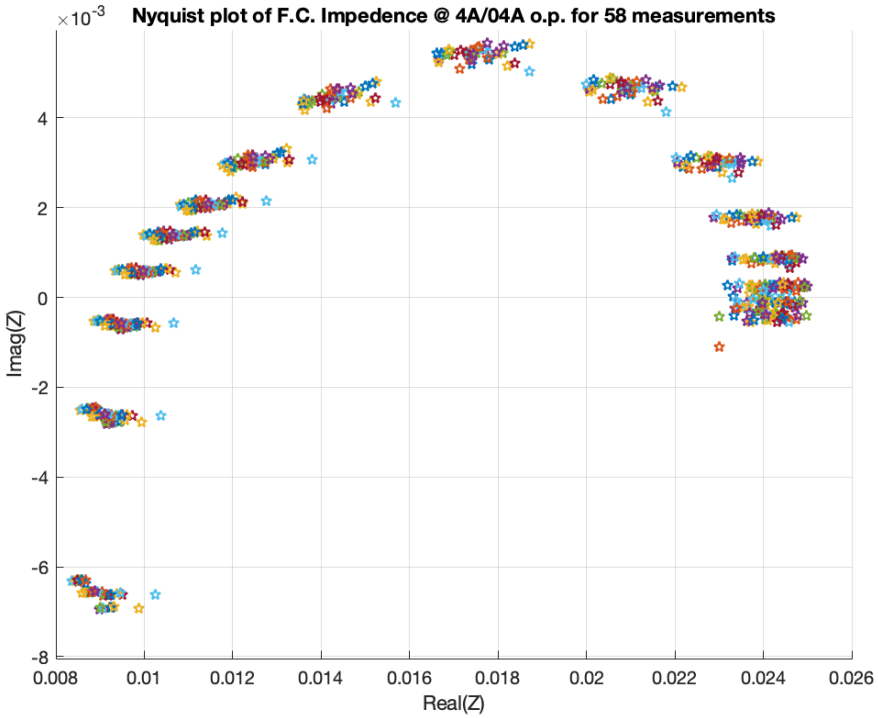

Figure 2.36: 58 cycles of EIS measurements.

Dataset building for the degradation process

When a fuel cell is used over time, the catalyst layer degrades over cycles of usage, getting the Nyquist plot shifted to the right of the plane and getting the imaginary part slightly greater over the cycles (see, for example, the results from [92]). Different cells do not behave exactly in the same way, even if they form the same stack. Indeed, the components of the cells present manufacturing differences and fluid dynamic conditions that produce slightly different behavior.

As stated before, the 58 cycles of EIS recording were representative of the healthy fuel cell; the point cloud shown in Fig. 2.36 did not present any degradation. To get a set of data that describes a degradation process, it is possible to use an accelerated degradation test, as proposed in Pivac et al. [93]. This kind of experiment, however, requires a long time, even if the test is "accelerated".

For this reason, to obtain a dataset representative of the degradation process, we started from the acquired data, shifting them to the right in the Z_{real}/Z_{imag} plane, according to the ranges reported in the literature [92]. In this way, starting from the experimental data of the CNR-ITAE healthy fuel cell, we obtained the degraded EIS dataset. As the cell degrades, the cell voltage (used as a parameter for the health of the cell) gets lower following the descending curve (Fig. 2.37 and Fig. 2.38).

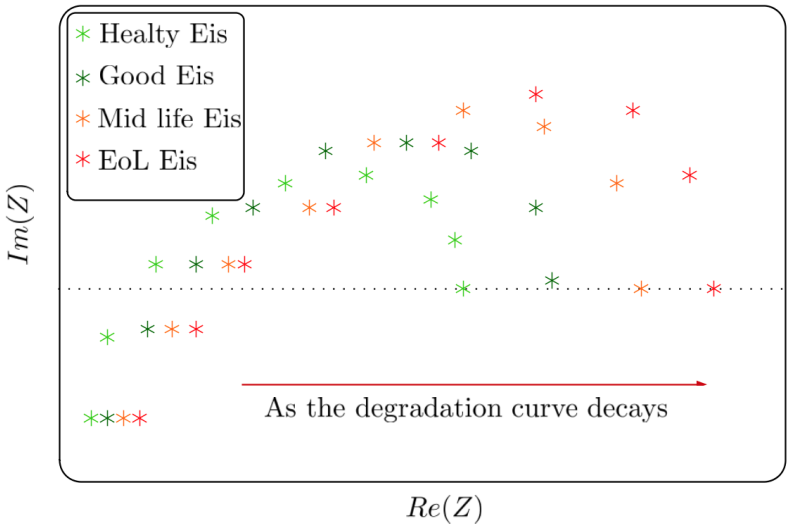

Figure 2.37: EIS trend degradation over cycles.

A reliable degradation model requires testing a wide number of cells, which is an expensive and time-consuming task. To this aim, we repeated

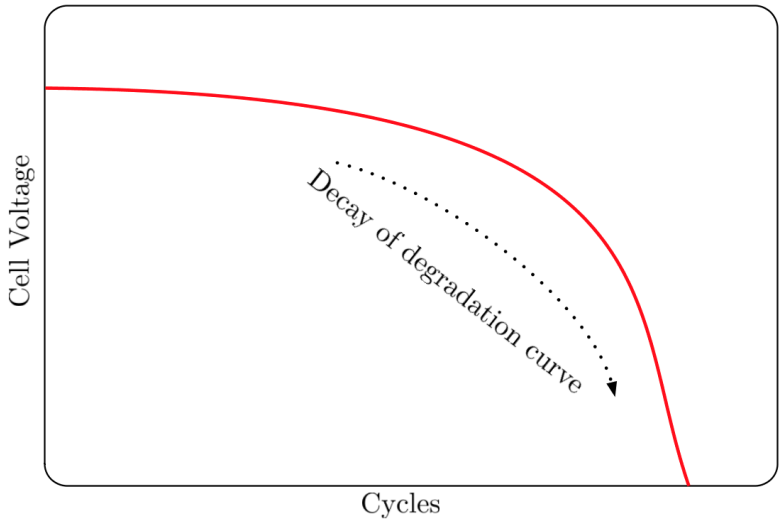

Figure 2.38: Relationship between the degradation curve of the cell and EIS measurements.

the degradation simulations starting with the same empirical data recorded and randomly changing the degradation rate of each simulation to consider the cell diversity. The complete simulation procedure is described in more detail in the following.

Simulation algorithm

The degradation process was implemented in Matlab, manipulating the real data recorded through the Autolab environment; the code was divided into the following steps:

1. healthy data were uploaded, creating two main column vectors: Z_{real}, Z_{imag};

2. two degrading coefficient, *alpha* and *gamma*, are selected in order to get the higher frequency points less shifted from the healthy values and, at the opposite, the lower frequencies ones more shifted, miming the empirical degradation measurements reported in literature [90, 92, 91]. Hence the dataset of the degraded EIS was derived; differences in rate and magnitude of the graph's shift with respect to the cited literature are determined by differences in the experiments' setup. The final result for one single FC dataset[4] is shown in Fig. 2.39;

[4]A single dataset represents a single degradation process for one fuel cell.

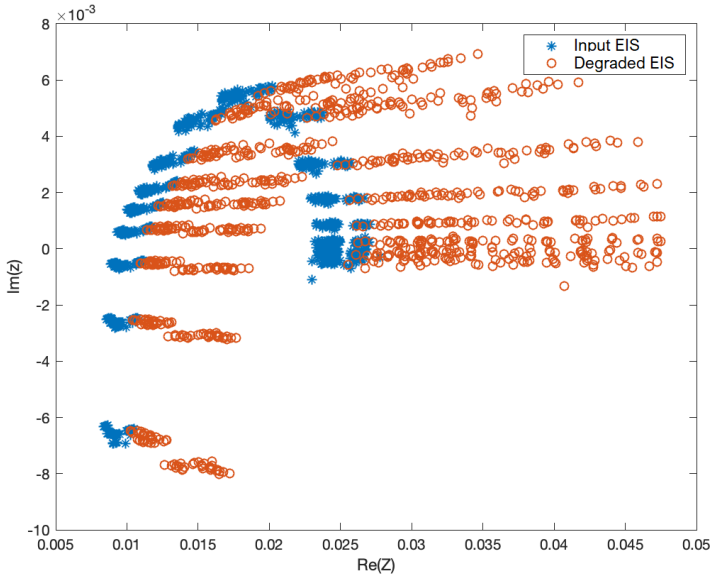

Figure 2.39: Simulated and real EIS measurement for one degradation process.

3. creation of the degradation curves and the association with EIS cycles: this process was essential in order to get the so-called *run until failure* data. First, a set of simulated points of the cell voltage was chosen and then interpolated with a generic cubic function; in this way, we have for each point on the Voltage-cycle graph the corresponding 16 EIS points; moreover, thanks to two random coefficients, the angular coefficient in the final part of the curve was randomly inclined, creating a single degradation curve for each fuel cell. Then, the process was repeated 100 times to simulate 100 degradation processes, so each of the 100 degradation curves was associated with the EIS measurement. The entire set of degradation curves for the 100 cells is presented in Fig. 2.40;

4. sequence padding: this is a technique used in Machine Learning to feed the net with sequences of the same length. The lower threshold used to cut-off data was 0.4 V; this represents the point of failure in which the cell was considered dead or unusable;

5. the final part of the script concatenates the 100 cell data to obtain the final dataset.

A simulated dataset composed of 100 FC data in which the EIS

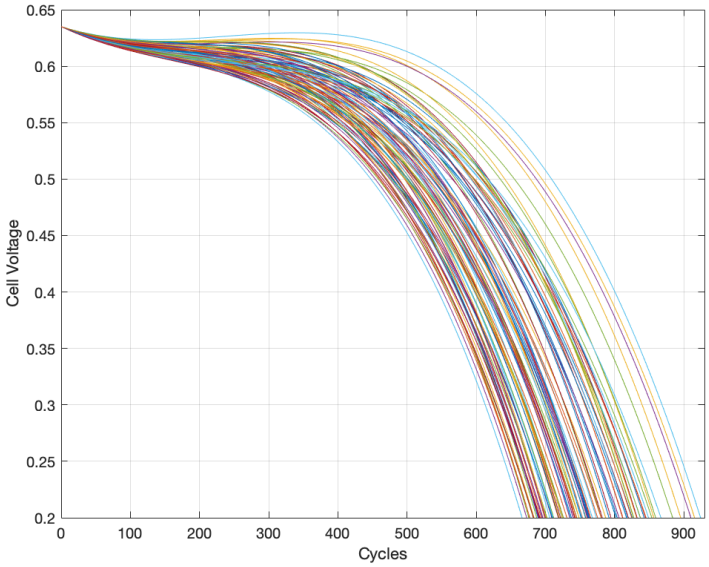

Figure 2.40: Set of degradation curves.

measurements are degraded over time cycles is finally obtained. The obtained dataset is used to train the LSTM to perform degradation prediction, as described in the following.

2.4.3 The LSTM training

A LSTM architecture is a recurrent neural network capable of learning long-term dependencies [94]. It consists of a set of recurrent subnets known as memory blocks; each block contains one or more self-connected memory cells. Blocks can be stacked and connected together in order to get a network. Each cell has three multiplicative units (the input, output and forget gate) that manage the storage of weights inside the structure and provide write, read and reset operations to remove or add information to the cell state.

For neural networks with multiple LSTM units and multiple layers, the hyperparameters are defined as the *time window*, the *batch size* and the *number of LSTM layers*.

The ability of LSTM to extract temporal relationships is generally given by changing the hyperparameters and tuning them until a good result is found. The hyperparameter selection is usually made by a trial-and-error procedure [95].

The LSTM network for prediction FC degradation

The learning/test phases of the neural network, built in Python using Google Keras library, require the input of a three-dimensional array structured as follows:

- time step (or window size): represents the floating window which, in our case, was maintained to "one" to get a one-step-ahead prediction.
- input dim: the number of features that is 32, as the 16 points taken for each EIS measurement was composed of real and imaginary part (Fig. 2.36).
- batch size: here, it is selected as the actual length of the dataset provided to the network for training.

The target is assigned as the value of the one-step-ahead degradation curve value so that the LSTM network will learn how the EIS cycle is related to the values of the degradation curve of the next cycle. As the time windows get through the data sequence, the LSTM net reconstructs the degradation curve.

After the trial-and-error hyperparameters selection, the best results, with respect to the Root Mean Square Error value, are obtained with the structure reported in Fig. 2.41.

Layer (type)	Output Shape	Param #
lstm_1 (LSTM)	(None, 1, 100)	53200
dropout_1 (Dropout)	(None, 1, 100)	0
lstm_2 (LSTM)	(None, 1, 100)	80400
dropout_2 (Dropout)	(None, 1, 100)	0
lstm_3 (LSTM)	(None, 100)	80400
dropout_3 (Dropout)	(None, 100)	0
dense_1 (Dense)	(None, 50)	5050
dense_2 (Dense)	(None, 25)	1275
dense_3 (Dense)	(None, 5)	130
dense_4 (Dense)	(None, 1)	6

Total params: 220,461
Trainable params: 220,461
Non-trainable params: 0

Figure 2.41: Model summary.

To perform the model validation, the network was simulated over a set of fresh data belonging to a new cell in order to get the predicted degradation curve. Fig. 2.42 shows the reconstructed degradation curve.

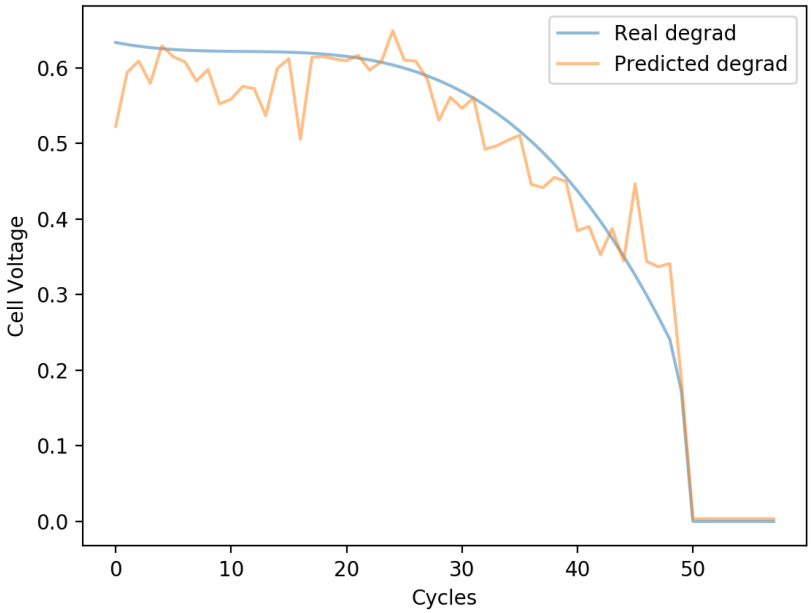

Figure 2.42: Degradation curve reconstructed by the net.

Chapter 3

Electrochemical Hydrogen Compressor[1]

Hydrogen meets the requirements to become a proper alternative in the energy storage field, thanks to its high gravimetric energy density. If it is produced in a carbon-free way (e.g., from renewable electrolysis), it can become a green energy carrier.

At present, hydrogen is still mainly extracted from hydrocarbons and contains a lot of impurities, even if produced by biological processes [97]. PEM fuel cell needs a 99.99% level of hydrogen purity to work properly [23]; therefore, the obstacle of hydrogen purification must be overcome to concretize the hydrogen economy perspective.

Another issue concerns the small volumetric energy density of hydrogen under ambient conditions. The most used way to store hydrogen is as compressed gas [98]. On-board storage reaches pressures up to 700 bar [19] and hydrogen refuelling station even up to 1000 bar [99].

Hydrogen purification and its compression must be carefully evaluated with efficiency, cost and safety analyses to achieve a competitive level compared to conventional fuels [100].

Currently, hydrogen purification and pressurization are two physically separated processes [97] as mechanical-diaphragm or piston compressors are the most used and mature compression systems [101]. They show several disadvantages, such as size, weight, efficiency, maintenance, cost, many noisy moving parts and the need for lubricants [102]. They have low efficiency when operating under off-design conditions and need an upstream purification module.

In contrast, non-mechanical compressor systems can offer promising

[1]This chapter is taken from [47] and [96], of which the Ph.D. candidate is an author.

results. Druart et al. [97] discussed the pros and cons of the most relevant ways for hydrogen purification and compression, concluding that the Electrochemical Hydrogen Compressor can be the most suitable device for the hydrogen-energy application. Toghyani et al. [103] compared the efficiency of an EHC, an ejector and a mechanical compressor for the hydrogen recirculation on a PEMFC and concluded that the system using a mechanical compressor has the worst performance due to the greater energy consumption.

The Electrochemical Hydrogen Compressor guarantees less energy consumption and higher efficiency even for small systems [104]. It is a solid-state system that has similar components to a PEM fuel cell [47]: one cell consists of a MEA positioned between two stainless steel plates for hydrogen flow (low-pressure and high-pressure sides) and system tightening. The MEA is the core of the device: it is the assembly of a polymer electrolyte membrane (generally of Nafion) positioned between anode and cathode electrodes. The Nafion allows the proton conduction (thanks to the water used in the chemical process), the separation of reactant gases and the electric insulation of the two electrodes. Each electrode has a catalyst layer that plays an important role in the reaction kinetics.

The cell can act as a fuel cell or an electrochemical compressor. If the assembly works as a fuel cell, the anode is fed by hydrogen and the cathode by air or oxygen; when the gases react producing water, an electrical current is generated. Instead, in an EHC operating mode, only the anode is fed (always by hydrogen) and an external voltage is applied across the electrodes (the structure behaves as a load, Fig. 3.1). The low-pressure hydrogen oxidates, being split into protons (that move across the membrane to the cathode) and electrons (that move through an external circuit to the cathode) [105], according to the hydrogen oxidation reaction (HOR):

$$H_2(LowPressure) \rightarrow 2H^+ + 2e^- \tag{3.1}$$

Then, at the cathode, the hydrogen evolution reaction (HER) takes place [106, 107] and hydrogen is made again, but at high pressure:

$$2H^+ + 2e^- \rightarrow H_2(HighPressure) \tag{3.2}$$

Considering the overall reaction involved in the process, an EHC takes low-pressure hydrogen as input and gives high-pressure hydrogen as output [108, 109]:

$$H_{2(LP)} \rightarrow H_{2(HP)}$$

The external voltage U applied across the electrodes includes the

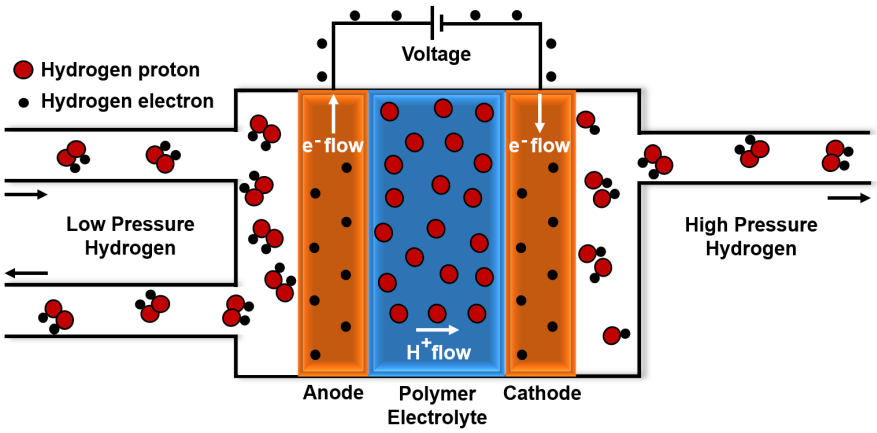

Figure 3.1: How an Electrochemical Hydrogen Compressor works: the polymer electrode membrane is positioned between two catalysts containing electrodes and allows the hydrogen protons to move from the left to the right side. Hydrogen electrons flow in the same direction by a power supply. Then, the chemical reduction reaction occurs at the cathode and hydrogen is made again, but at high pressure.

theoretical overpotential $U_{theoretical}$, the activation overpotential $V_{activation}$ and the Ohmic overpotential V_{Ohmic}:

$$U = U_{theoretical} + V_{activation} + V_{Ohmic}$$

In particular, $U_{theoretical}$ is given by the Nernst equation [110] and describes the effect of temperature and partial pressure over the theoretical potential:

$$U_{theoretical} = E_0 + \frac{RT}{nF} \ln \frac{p_2}{p_1} \tag{3.3}$$

where E_0 is the standard potential, R the ideal gas constant, T the absolute temperature, n the number of electrons, F the Faraday constant, p_2/p_1 the ratio between the hydrogen pressure at the cathode (high-pressure side) and the hydrogen pressure at the anode (low-pressure side).

Thanks to the membrane, the EHC performs hydrogen purification together with its compression under specific operating conditions, resulting in a more compact solution compared to other compressors. Furthermore, hydrogen can be pressurized up to several hundred bars with a single cell [111]. The EHC has a simple modular structure that can be scaled to guarantee a specific flow rate, no moving parts (no lubricants contamination or noise), low energetic cost consumption and no maintenance is needed. It can be used in many applications, such as anode

recirculation (0-2 barg), solid storage (10-50 bar), industrial gas cylinders (200-350-700 bar), high-pressure storage tanks for automotive (350-700 bar) and hydrogen refueling station (700-1000 bar).

The Ph.D. research activity about the Electrochemical Hydrogen Compressor started at the CNR–ITAE laboratory by analyzing the EHC polarization curve at different compression ratios. As for fuel cell systems, the polarization curve is one of the techniques used for EHC characterization. Another interesting measurement carried out at the CNR–ITAE laboratory to understand the behavior of the hydrogen compressor is the time test, where a fixed voltage is imposed for a long time period (hours) to estimate the system response during the whole observation time. Modeling followed the experimental work with the structural analysis of the EHC monopolar plate for a system operating at 700 bar; calculating the stress field in such components prone to hydrogen embrittlement is essential due to the possibility of failure. Indeed, irregular shape variations generate peaks of stress magnitude and triaxiality, further contributing to decreasing metal ductility at the local scale.

The chapter is organized as follows: in Section 3.1 the influence of the compression ratio on the EHC polarization curve is studied; Section 3.2 reports the results of an EHC unstable time-test measurement, investigating the possible chaotic behavior of the EHC. Finally, Section 3.3 describes a conceptual design of an EHC operating at 700 bar, starting by comparing three different geometric configurations, then finding the optimal design in order to have conservative levels of the nominal stress states.

3.1 Compression ratio influence on EHC performance

In this thesis, the polarization curve of an Electrochemical Hydrogen Compressor was investigated at different compression ratios. It showed a linear behavior of the current density as a function of the voltage. As expected, a higher compression ratio between the cathode and anode increased the voltage required to perform the compression process.

This section is organized as follows: after a brief state of the art, the experimental setup is described in Subsection 3.1.2, showing schematic piping diagrams as FC and compressor; Subsection 3.1.3 presents the measurements results and discussion.

3.1.1 State of the art

The literature on the Electrochemical Hydrogen Compressor is rather sparse compared to the research conducted about fuel cell systems.

Many studies investigated different types of membranes [112, 113]. The one developed by HyET allows compressing hydrogen up to 1000 bar thanks to increased proton conductivity and decreased hydrogen back-diffusion [20]. This latter characteristic impacts the maximum achievable pressure; for this reason, it was investigated by a wide number of researchers [98, 24, 27]. Many other works focused on the effects of a specific working variable, such as output pressure, temperature (inlet or cell temperature), flow rate or relative humidity [102, 114, 115]. In particular, Zou et al. [102] analyzed the effects of stoichiometric ratio, inlet temperature and pressure, using polarization curves, electrochemical impedance spectroscopy and time test at different voltages. Chouhan et al. [98] used pressure and current density curves over time at four applied voltages to find that a single cell with an operating voltage of 0.1 V can achieve a compression ratio of 150.

The thesis focused on the performance of an Electrochemical Hydrogen Compressor at different compression ratios (ratio between anodic and cathodic pressures). In particular, it investigated the effect that the compression ratio has on the energy consumption of the process.

3.1.2 Experimental setup

The first step in the activity concerned the realization of a new MEA and, consequently, the fuel cell assembly, considering that both fuel cells and EHC have the same structure.

The experimental measurements were carried out at the CNR-ITAE laboratory. The FC/EHC used in the measurements consists of a single cell of 25 cm^2 active area, with two copper end-plates and a Teflon seal (0.2 mm of thickness) to prevent hydrogen leakage.

Fuel cell setup

After the assembly phase, the cell was set into the correct working conditions through the break-in phase. It was performed using the experimental setup shown in Fig. 3.2a, in which the assembled device was used as FC in the Fuel Cell Technologies Testing Station (Fig. 3.3a).

The CNR-ITAE laboratory uses a common standard procedure for the break-in phase; these guidelines foresee ten polarization curves [47] in which the output voltage of the fuel cell is represented as a function of the input current density [40]. The measurements were performed under the following conditions:

- variable stechiometry (fixed flow);
- H_2 flow (anode): 260 sccm, air flow (cathode): 875 sccm;
- anode and cathode pressure: 3 bar(a);
- temperature: 80 °C;
- relative humidity: 100%.

EHC setup

After the break-in phase, the experimental measurements were performed as EHC using the experimental setup shown in Fig. 3.2b and Fig. 3.3b: hydrogen feeds the anode through a pressure regulator, a mass-flow controller (used to measure and control the flow) and a bubble humidifier at the end; two back-pressure regulators are used to maintain the desired pressure [47]. Compared to the FC setup, the cathode (air) inlet was closed and the cell was connected to the Autolab PGSTAT302N potentiostat/galvanostat power supply and to its BOOSTER20A module, extending the maximum current up to 20 A.

EHC measurements were polarization curves too, where the voltage represents the energy consumption for the compression process, while the current is proportional to the hydrogen pumped from the anode to the cathode.

Tests were performed under the following conditions:

- H_2 flow (anode): 260 sccm;
- anode pressure: 1 bar(a); cathode pressure: from 1 to 5 bar(a);
- temperature: 60 °C;

- relative humidity: 100%.

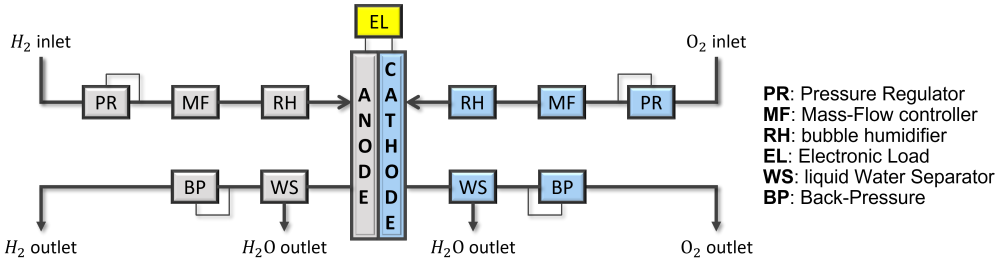

(a) Schematic piping diagram of the device, operating as FC.

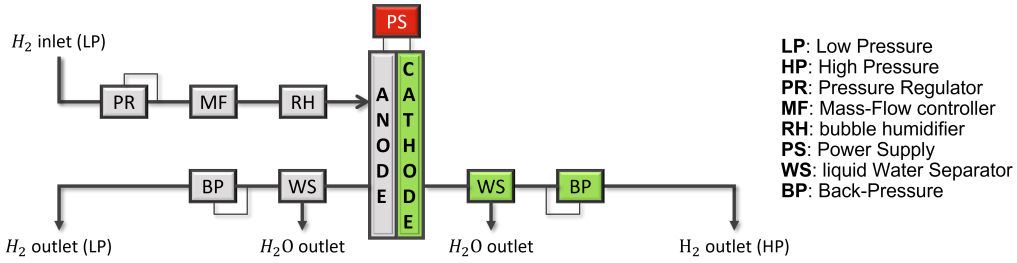

(b) Schematic piping diagram of the device, operating as EHC.

Figure 3.2: Schematic piping diagram of FC/EHC device.

3.1.3 Measurements and discussion

Fuel cell results

The software of the FCT-TS provides the experimental polarization curve obtained during the test [39], and Fig. 3.4 shows the results before and after the MEA activation: the voltage of the blue curve is higher than the green one in all the current density roundtrip, the OCV increased from 0.92 V to 0.97 V and the membrane resistance decreased from 25.5 mΩ to 24.3 mΩ.

The polarization curve shows a voltage hysteresis in the forward direction with increasing current densities and then in the backward direction with decreasing current densities. It is due to the variations in the concentration polarization at low current densities and the variations in the activation polarization at high current densities, while the relative contribution to the total polarization of the cell is the opposite (concentration polarization dominating at high current densities and

(a) FCT-TS. (b) EHC testing station.

Figure 3.3: Testing stations in the CNR-ITAE laboratory.

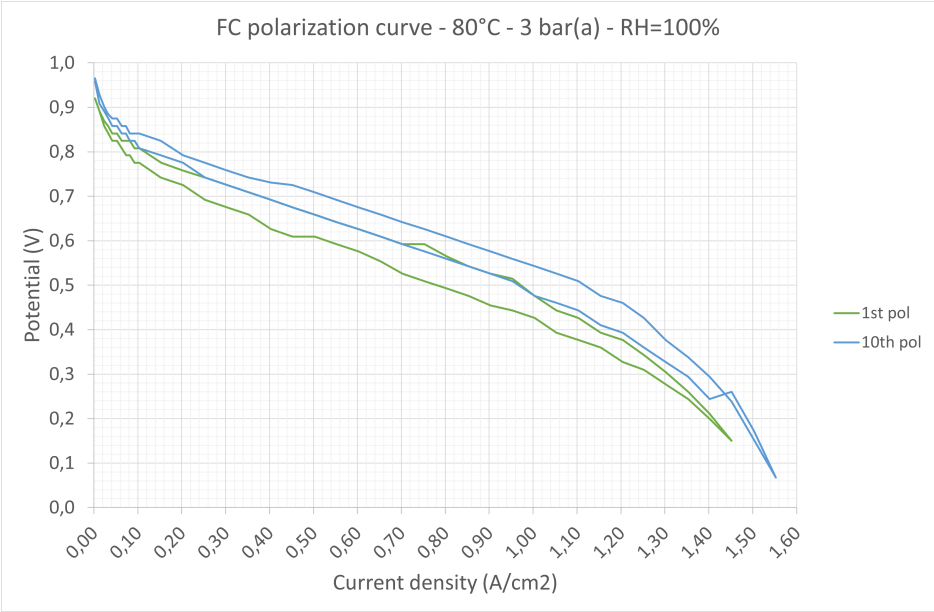

Figure 3.4: FC polarization curves before (green curve) and after (blue curve) the break-in phase.

activation polarization dominating at low current densities). About the cell ohmic resistance, it has a minor effect on voltage hysteresis [116].

Electrochemical Hydrogen Compressor results

All the polarization curves were performed measuring the current for an applied voltage (amperometric mode). The voltage scan rate was 0.005 V/s with step of 0.01 V. The potential started from 0 V and stopped at 1 V. However, the Autolab PGSTAT302N power supply has 2 A as its maximum current, which was extended up to 20 A using the BOOSTER20A module; for this reason, all the polarization curves were cut at the current limit value (0.8 A/cm^2 for a cell of 25 cm^2).

The first polarization curve on the EHC testing station was performed without compressing hydrogen, fixing the inlet and the output pressure to 1 bar(a) ($\beta = 1$). As shown in Fig. 3.5, the applied voltage used to compress hydrogen and the current density (i.e., the hydrogen flow) that crosses the membrane have a linear correlation in the studied range.

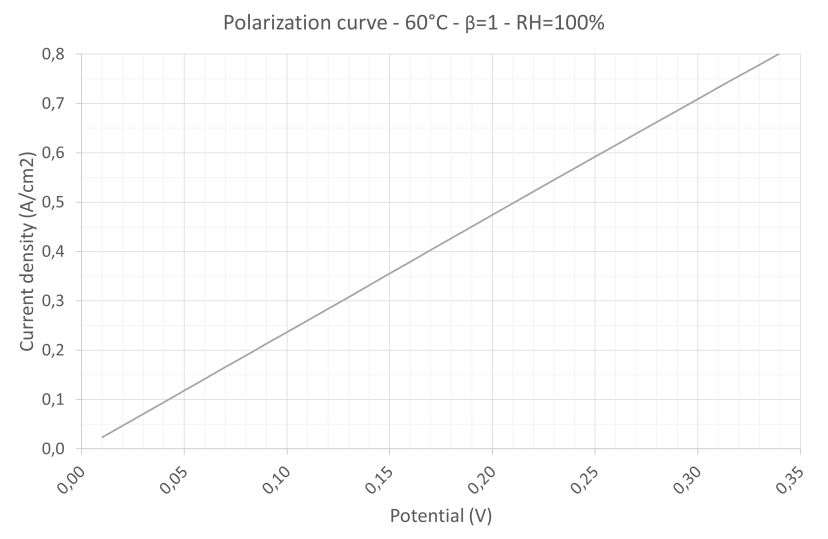

Figure 3.5: Linear behavior in the EHC polarization curve.

Fixing the anodic pressure at 1 bar(a), other polarization curves were performed at different cathodic pressures (2, 3, 4 and 5 bar(a)) to investigate the influence of the compression ratio on the performance of the electrochemical compressor. As expected, as the pressure increased, transporting H^+ ions through the membrane became more and more difficult and the voltage required to compress the hydrogen (corresponding to the consumed power) increased (Fig. 3.6).

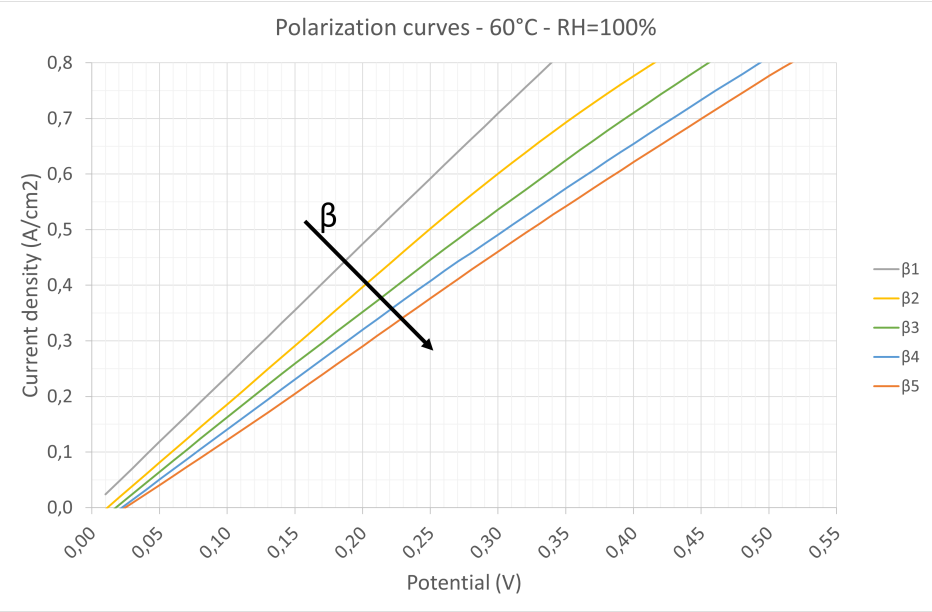

Figure 3.6: Influence of the compression ratio on the EHC polarization curve.

3.2 Chaotic behavior in Electrochemical H_2 devices[2]

The chaotic analysis is often used to investigate electrochemical signals. In this thesis, it was applied to understand the behavior of hydrogen electrochemical devices, with particular attention to the Electrochemical Hydrogen Compressors. Measurements carried out at the CNR-ITAE laboratory showed a current fluctuation with a fixed voltage. The oscillating phenomenon is not justifiable by the Nernst equation and the possible chaotic behavior of the EHC was investigated.

This Section is organized as follows: firstly, state of the art is presented; Subsection 3.2.2 describes the experimental setup, while in Subsection 3.2.3 the measurements are presented; Subsection 3.2.4 illustrates and discusses the results of the chaotic analysis.

3.2.1 State of the art

Chaotic systems are dynamic systems highly sensitive to initial conditions and whose apparently random states of disorder and irregularities are often governed by deterministic laws. This behavior exists in many natural systems (fluid flow, climate changes) and also in systems with artificial components, such as road traffic. It can be modeled mathematically or through analytical techniques.

The chaotic analysis is a powerful tool used in electrochemistry to investigate electrochemical signals. Bahena et al. [117] analyzed the electrochemical noise measured on a NiCoAg alloy immersed in Hank solution. The time series observed during the corrosion process was characterized by non-linear fractal analyses and showed irregularity correlated to deterministic chaos rather than random noise. Trzaska et al. [118] studied the chaotic phenomena on an electrochemical reactor using a fractional-order non-linear circuit. Guderian et al. [119] controlled chaos in the experimental Belousov-Zhabotinsky (BZ) reaction; they stabilized several unstable periodic orbits, sinusoidally modulating the electric current on a Pt-working electrode. Others studied synchronization phenomena in electrochemical oscillators. Cruz et al. [120] immersed two anodes in an electrolytic solution and, decreasing the distance between the two anodes, identified different domains of chaotic synchronization, experimentally proving the existence of a synchronization sequence.

[2]This section is taken from [47], of which the Ph.D. candidate is an author.

The thesis proposed the result of a chaotic test on an EHC unstable measurement. The measure was performed with a fixed voltage, but the current showed an oscillating phenomenon in the time domain. This behavior, not justifiable by the Nernst equation, motivated the reason for performing the chaotic analysis.

3.2.2 Experimental setup

The experimental EHC measurements were carried out with the experimental setup shown in Fig. 3.2b and Fig. 3.3b.

The CNR-ITAE laboratory is provided with two specific devices: Autolab PGSTAT302N and Keysight Technology N6973A power supply. The first is the one used in Chapter 2 and Section 3.1. The N6973A power supply (Fig. 3.7) is less precise than Autolab PGSTAT302N, but it works at more than 2 A currents, for which reason it was used in this experiment. It has been recently equipped with LabView-based software to perform polarization curves or time tests on the EHC.

Figure 3.7: N6973A power supply.

3.2.3 Measurements

The measurements were realized on the cell of 25 cm^2 active area. First, it was necessary a break-in phase to bring the cell into the correct working conditions. In particular, the break-in was performed in fuel cell modality, using the experimental setup reported in Fig. 3.2a. As explained in the previous Section, guidelines foresee ten polarization curves for the break-in phase. The tenth polarization curve is shown in Fig. 3.8.

After the break-in phase, the experimental setup was changed because the cell had to work as EHC. The measure was a time test where a voltage of 0.25 V was imposed for 29 000 s to have a more reliable result. The temperature of the cell, humidifier and tape was set to 60 °C and it was

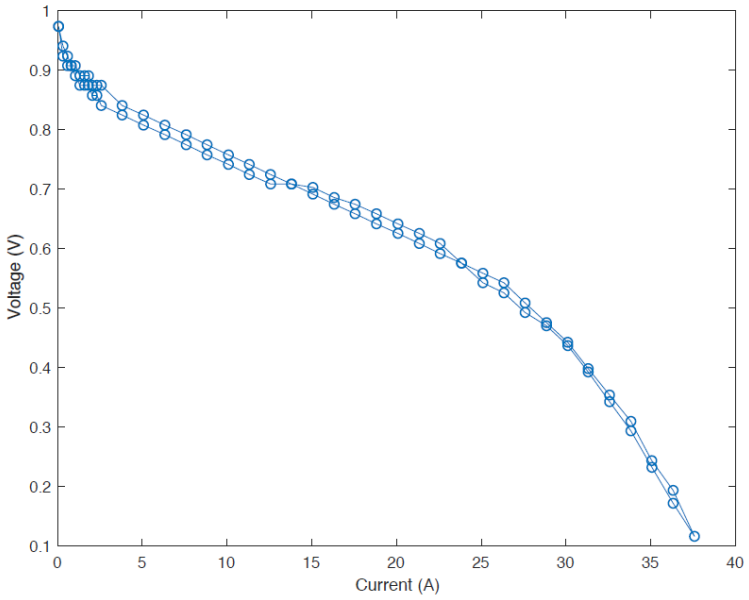

Figure 3.8: Polarization curve n. 10.

maintained constant for all the measurements phase. Moreover, β, defined as the ratio between the pressure at the cathode and at the anode, was 1.

The behavior of the EHC resulted very different from what was expected from studying the physical model (Fig. 3.9). The system seems to have a spiking dynamic; therefore, the impedance of the EHC changes in time.

3.2.4 Chaotic analysis: results and discussion

Chaotic systems are dynamic systems highly sensitive to initial conditions and whose apparently random states of disorder and irregularities are often governed by deterministic laws. Indicators of the high sensitivity of chaotic systems to initial conditions are the Lyapunov exponents [121]. They were the first parameters to be calculated.

In order to be able to analyze the dynamic of the system starting from a signal in the time domain, the so-called time delay technique was used [122]. The basic idea is to make copies of the signal with fixed time delays and consider these delayed values as coordinates of a phase space retrieved from data. This technique, therefore, associates to each measure $s(n)$ the m-dimensional vector $y(n)$ as follows:

$$y(n) = [s(n), s(n+\tau), \ldots, s(n+(m-1)\tau)] \tag{3.4}$$

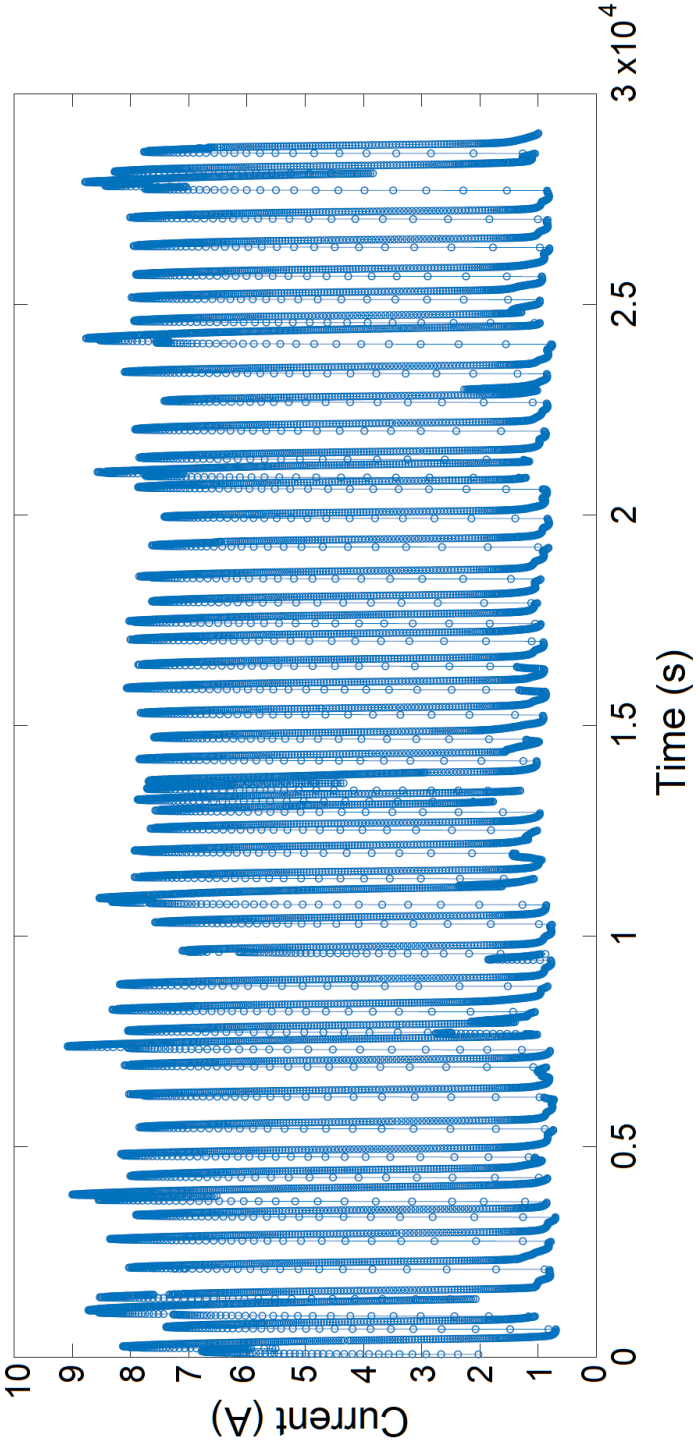

Figure 3.9: EHC time test: V = 0.25 V, $\beta = 1$, 29 000 s.

where τ represents the delay and m is the embedding dimension.

Assuring the equivalence between the original trajectory and the reconstructed one, thanks to Mañé's theorem [123], Takens' theorem [124] and Eckmann-Ruelle's conjecture [125], the analysis of the dynamic can be performed. To calculate properly the Lyapunov exponents of a system, Mohammadi [126] realized a Matlab code to perform this kind of analysis. It is characterized by the function lyaprosen, which arguments are the signal y, the delay τ and embedding dimension m. If τ or m are set to zero, the algorithm will calculate the best values using different optimization criteria.

To choose m, the False Nearest Neighbors (FNN) algorithm realized by Hegger and Kantz is used: the idea is to analyze how the number of neighbors of a point along a signal trajectory changes with increasing embedding dimension [127]. In too low an embedding dimension, many of the neighbors will be false, but in an appropriate embedding dimension or higher, the neighbors are real. With increasing the dimension, the false neighbors will no longer be neighbors. Therefore, by examining how the number of neighbors changes as a function of dimension, an appropriate embedding can be determined. Alternatively, the symplectic geometry method will be used.

To choose τ, instead, the algorithm will use autocorrelation up to orders 10 to select proper embedding lag, which is the lag before of first decline of autocorrelation value below e^{-1}. If this method does not give any result, the mutual information criteria will be used. Using the signal in Fig. 3.9, the optimal value of m calculated by the algorithm is 2; instead, an optimal value of τ was not found. For this reason, the largest Lyapunov exponent is calculated for three different τ: 10, 100, and 1000.

In Tab. 3.1 are summarized the largest Lyapunov exponents calculated by the algorithm and they are all positive, so the system is sensitive to the initial conditions for different τ and m.

Table 3.1: Lyapunov exponents.

	$m = 1$	$m = 2$	$m = 3$
$\tau = 10$	0,0594	0,0668	0,0600
$\tau = 100$	0,0594	0,0607	0,0507
$\tau = 1000$	0,0594	0,0607	0,0507

Continuing with the embedding technique, it is possible to reconstruct the phase plane through the algorithm realized by Leontitsis [128].

Imposing $\tau = 100$ and $m = 2$, the reconstructed phase space (both 2D and 3D) are shown in Fig. 3.10 and 3.11. From the results, it is visible how the reconstructed phase space is characterized by a density of periodic orbit; this feature is common in chaotic systems. Consequently, the dynamic analysis carried out has found evident characteristics of chaotic systems. It is not possible to say with certainty that the system expresses a chaotic dynamic, but this research work represents an initial analysis of an unknown phenomenon. At the same time, fractional calculus [129] is used to model and control PEM fuel cell [130, 131]. So, starting from [132, 133, 134], a similar approach could be applied to model and control the described hydrogen electrochemical device.

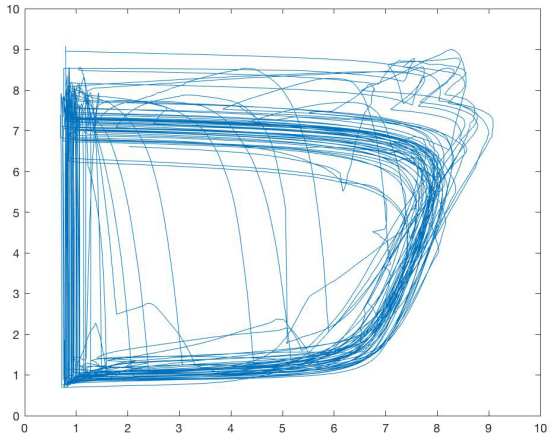

Figure 3.10: Phase space reconstruction - 2D.

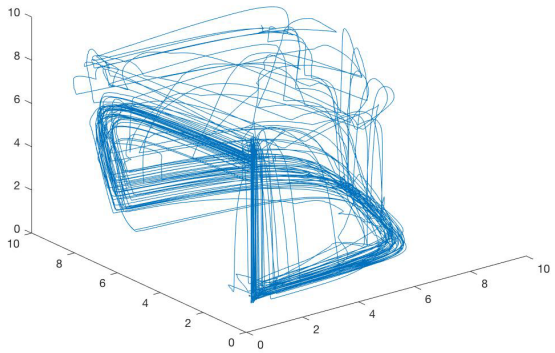

Figure 3.11: Phase space reconstruction - 3D.

3.3 Structural analysis of EHC End-Plates[3]

In this thesis, the monopolar plate of an Electrochemical Hydrogen Compressor prone to hydrogen embrittlement is analyzed. Irregular shape variations generate peaks of stress magnitude and triaxiality, further contributing to decreasing metal ductility at the local scale. The calculation of the stress field in such components is essential due to the possibility of failure due to the material embrittlement caused by hydrogen.

The thesis presented a conceptual design of an EHC operating at 700 bar and focused on the shape and the mechanical stress of the end-plates in order to have conservative levels of the nominal stress states, which then were taken as the design parameter for providing adequate structural integrity and mechanical reliability to the component. The FEM (Finite Element Method) analysis with Marc software - of MSC Software Corporation - identified the optimal end-plates configuration in circular plan view and active area. The plate, sized to have a deflection no greater than 0.1 mm when the EHC works at 700 bar, should have the minimum thickness of 17 mm.

This Section is organized as follows: in Subsection 3.3.1 state of the art is presented; Subsection 3.3.2 describes the numerical analysis, the methodology and results firstly for the comparison of different geometries and then, once evaluated the best geometric configuration, for the design of the plate.

3.3.1 State of the art

The structural design of the components in contact with gaseous hydrogen must consider the known phenomenon of hydrogen embrittlement. It deteriorates a particular feature of structural metals, such as their ductility. Surface cracks also occur on unstressed components subjected to cathodic charging [135]. Zhou et al. [136] proposed the adoption of "high entropy alloys" (HEA) as a countermeasure for limiting the decrease of ductility as the hydrogen content increases in time. Ogata [137] and Tomohiko et al. [138] thoroughly investigated the detrimental effect of hydrogen absorption in AISI stainless steels by also quantifying the decrease of allowed fatigue cycles and monotonic true stress-strain curves promoted by different amounts of adsorbed H_2.

As for fuel cell design, also the EHC needs FEM computer modeling to optimize its components (electrodes, catalysts, membrane, monopolar and bipolar plates, gaskets and bolts) and to improve the understanding of the

[3]This section is taken from [96], of which the Ph.D. candidate is an author.

mechanisms that govern the cell [139]. Furthermore, for the EHC is necessary to scale up the structural components to higher pressures. In the literature, a few researchers have been dedicated to this purpose. Baker et al. [140] compared different geometrical configurations of gas distribution channels using computational fluid dynamics to determine the most effective. Other studies investigated improving the EHC structure to increase efficiency and reduce hydrogen back diffusion [107].

The thesis aimed to analyze the monopolar plate of an Electrochemical Hydrogen Compressor operating at high pressure (700 bar) in order to guarantee conservative levels of the nominal stress states also when the stress peaks (due to the irregularities in the shape of the mechanical component) combined to the ductility decrease (due to the hydrogen embrittlement) can increase the possibility of local failure. The conceptual design started by comparing three different geometric configurations of the end-plate to find the optimal design that guarantees structural integrity and mechanical reliability.

3.3.2 Numerical analysis

The main components of an EHC stack are:

- the Membrane Electrode Assembly, constituted by two (anodic and cathodic) electrodes, two (anodic and cathodic) catalyst layers and a proton conductive membrane;
- bipolar plates, made of stainless steel. They contain the gas flow-field;
- end-plates, made of stainless steel or carbon fiber composite;
- bolts. On the end-plates, they ensure the gas tightening of the system;
- gaskets.

This study aims to optimize the design of an EHC single cell. In this case, the end-plates are monopolar plates, which means they contain the flow-field only on their internal side. The analysis is organized into two steps:

1. in the first step, different geometries of the monopolar plate are compared to identify the best configuration;
2. once the best geometric configuration had been evaluated, the second part of the study concerned the design of the plate.

Simulations have been performed by Marc Software of MSC Software Corporation. MSC Marc finite elements approach is especially suitable for involving nonlinear aspects of the numerical analyses, such as contact, here modeled, or for future developments of the work, such as implicit elastoplastic simulations or damage, and cohesive zone method for modeling damage and fracture under limit conditions. The software also allows for easily customizing the mathematical modeling of the material's

response via very flexible Fortran user subroutines.

Geometric details, such as the channels of the flow-field, were not taken into account: they were replaced with a groove whose dimensions correspond to the active area (the area in which chemical reactions occur). The depth of the groove was calculated by summing:

- the space for the MEA (overall thickness of 0.35 mm, hence 0.175 mm per plate);
- the depth the flow-field channels would have had if represented (0.5 mm);
- 1.5 mm corresponding to the thickness of a metallic mesh to put over the low-pressure channels to better support the MEA during operation.

The total depth of the groove is 2.175 mm for the low-pressure side and 0.675 mm for the high-pressure side. The FEM analyses were carried on for the low-pressure plate because they yield a conservative estimate for the high-pressure plate.

The mesh was created manually along with the geometry using brick elements that have three degrees of freedom per node. Because of the high corrosiveness of the compression process, the chosen material was AISI 316 stainless steel (European designation: X5CrNiMo17-12-2/1.4401). It is an austenitic chromium-nickel stainless steel containing molybdenum; it has excellent ductility with high corrosion resistance and mechanical strength at elevated temperatures. Its elastic properties, listed in Tab. 3.2, have references in [141, 142, 143, 144].

Table 3.2: Elastic properties of AISI 316 stainless steel [141, 142, 143, 144]: E is Young's modulus, ν the Poisson's ratio, σ_y the yield stress, σ_{UTS} the Ultimate Tensile Strength and HB the maximum Brinell Hardness. The first line contains the typical values; the second line reports the chosen values for the FEM simulations.

Values	E [GPa]	ν [-]	σ_y [MPa]	σ_{UTS} [MPa]	HB
Typical	193-200	0.27-0.3	200-300	500-700	215
Used	200	0.3	200	500	215

The working pressure of 700 bar acts on the upper side of the plate, inside the active area.

Part 1: methodology

The diffusion of hydrogen within mechanical components made of stainless steel is known to induce the embrittlement phenomenon, consisting of the reduction of the plastic strains locally attainable before failure [135, 136, 137, 138]. Consequently, the ultimate tensile stress and the fatigue response of stainless steel are negatively affected by pressure-driven diffusion of hydrogen within the alloy [137], while surface fracture can even be induced by cathodic charging with no outer stress applied [135]. In the application at hand, the contact between the surface of the compressor end-plates and the hydrogen flow is rather limited to the small-sized orifices and channels where the hydrogen is allowed to flow, so no large amounts of hydrogen can be expected to diffuse within the volume of the components. At the same time, such small-sized channels, holes, and irregular shape variations act as notches within the stressed mechanical component at hand, thus generating peaks of stress triaxiality, which further contribute to decreasing the ductility of metals at the local scale [145, 146]. According to such considerations, the design of mechanical components to be continuously operated in hydrogen environments must be aimed at conservative levels of the nominal stress states. This is the reason why the stress states have been taken as the design parameter to be evaluated and designed by the finite element method for providing adequate structural integrity to the component.

FC monopolar and bipolar plates at the CNR-ITAE laboratory utilize the configuration "a" represented in Fig. 3.12: it has a squared plan view and squared active area (the area in which chemical reactions occur). This configuration is usually used in fuel cell applications because it maximizes the utilization of the active area. An axisymmetric geometry is more suitable for EHC application due to the high pressure on the active area. For this purpose, the comparison between three different geometric configurations (Figg. 3.12-3.14) was initially carried on.

The plate sizes were calculated starting from the FC monopolar plates used at the CNR-ITAE laboratory with the following features:

- configuration "a";
- square side of plan view: 100 mm;
- square side of active area: 50 mm.

The other configurations have a circular plan view corresponding to the circle that circumscribes the square of the first configuration; a characteristic dimension greater than the one of case "a" (circle diameter against square side) was chosen to make the problem worse (larger size

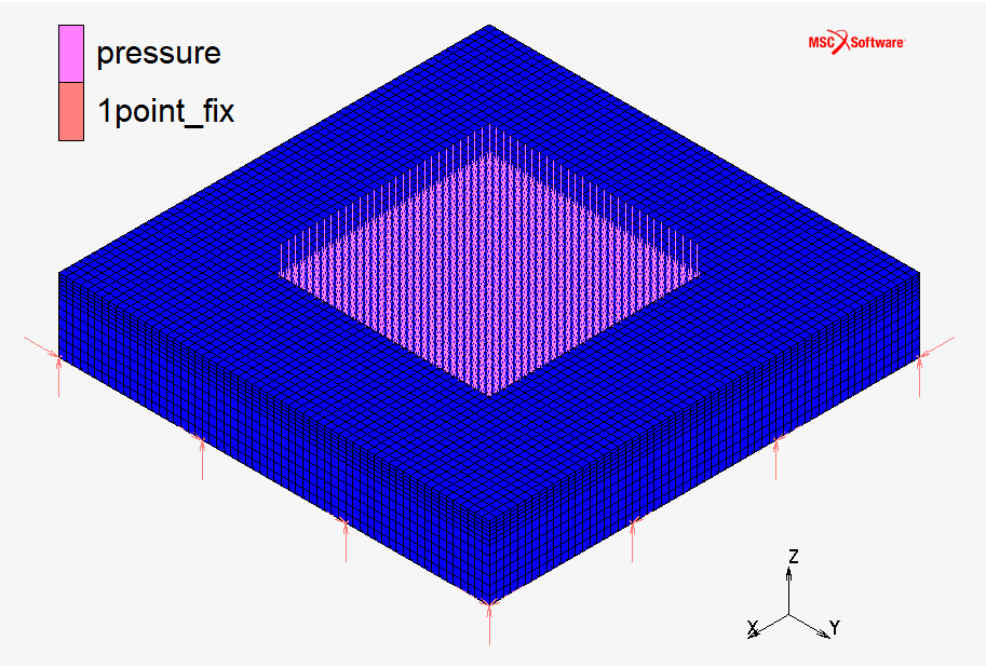

Figure 3.12: Monopolar plate - discretized domain in configuration "a": squared plan view and squared active area.

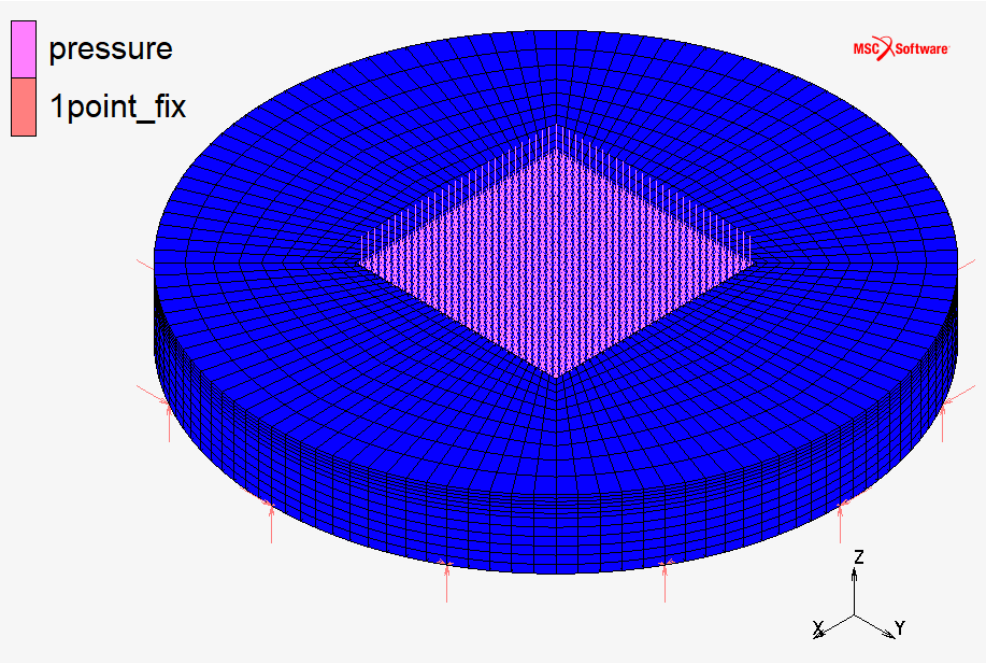

Figure 3.13: Monopolar plate - discretized domain in configuration "b": circular plan view and squared active area.

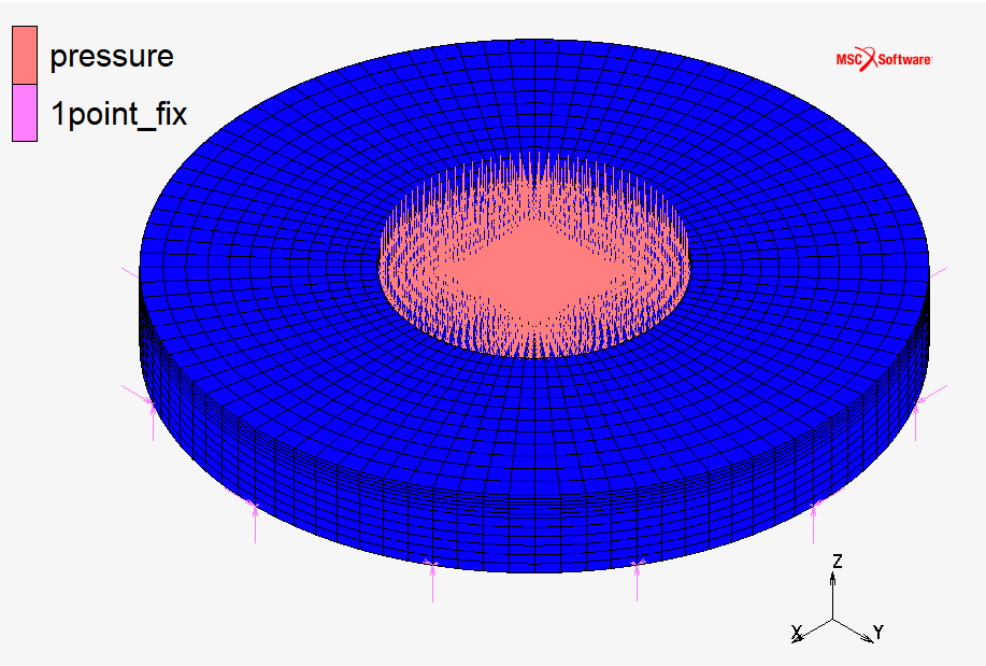

Figure 3.14: Monopolar plate - discretized domain in configuration "c": circular plan view and circular active area.

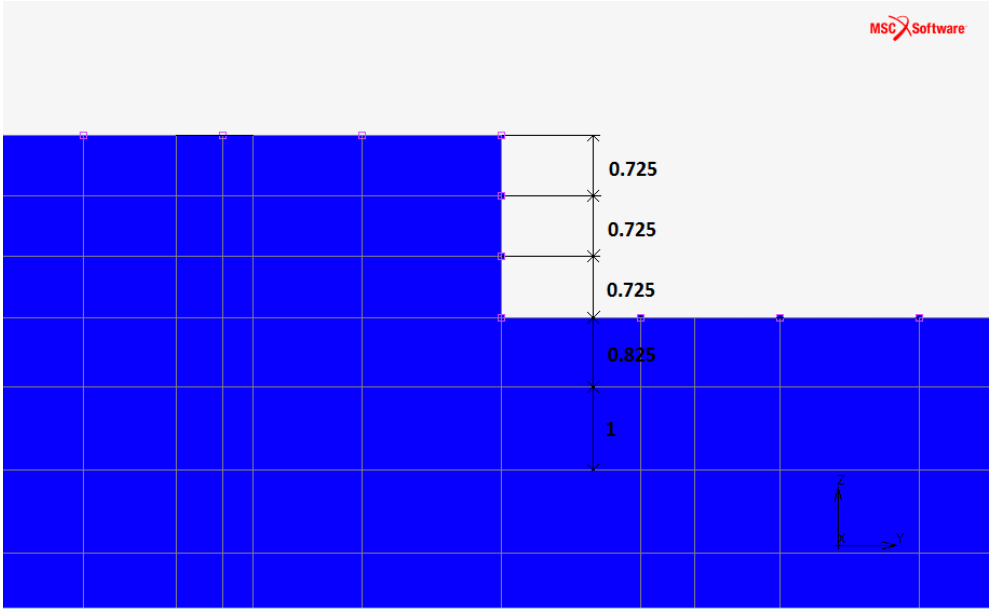

Figure 3.15: Monopolar plate - discretization along the z-axis in all the configurations (the dimension of each element is reported in mm).

means much deflection). It was calculated as:

$$d_p = \sqrt{2} l_p = 141.42\,\text{mm} \tag{3.5}$$

Finally, the circular active area of the last configuration corresponds to the circle that has the same area as the squared active area of the other two configurations:

$$d_{MEA} = 2 l_{MEA} \sqrt{\frac{1}{\pi}} = 56.5\,\text{mm} \tag{3.6}$$

About the sizing along the z-axis, the thickness of the plate is 30 mm for the three configurations. As stated above, the active area is deeper (Fig. 3.15) than the plate surface.

All the dimensions are summarized in Tab. 3.3.

Table 3.3: Active area AA_{MEA} [mm^2] and characteristic dimensions [mm] of the three plate configurations: l_p is the length (square side or diameter) of plate plan view, l_{MEA} is the length (square side or diameter) of the active area, t is the thickness of the plate and l_g is the depth of the groove.

	Conf. a	Conf. b	Conf. c
l_p	100	141.42	141.42
l_{MEA}	50	50	56.5
AA_{MEA}	2500	2500	2507
t	30	30	30
l_g	2.175	2.175	2.175

The comparison between geometries does not consider the bolts' holes that ensure the system's tightening: the plate was constrained by 3D pins placed at 12 points on the plate's lower - not loaded - side. The number of 3D pins was chosen considering the perimeter of the plate.

Part 1: results

Maximum values of deflection, equivalent strain and Von Mises stress, obtained from FEM simulations about the three configurations, are reported in Tab. 3.4. The results show that configurations "b" and "c" have a significant decrease in deflection compared to the deflection of configuration "a"; in terms of strains and stresses, excluding the constrained points that distort the actual trend, a drastic increase occurs in configuration "b", instead configuration "c" is the best in terms of stress.

Table 3.4: Maximum values of deflection (z_{max}), equivalent strain ($\epsilon_{max_{eq}}$) and Von Mises stress ($\sigma_{max_{VM}}$) for the three configurations.

		Conf. a	Conf. b	Conf. c
z_{max}	[mm]	−0.2081	−0.1333	−0.1374
$\epsilon_{max_{eq}}$	[%]	0.079	0.16	0.079
$\sigma_{max_{VM}}$	[MPa]	180	340	145

Based on the results of this comparison, the plate's design concerned the third configuration.

Part 2: methodology

The goal of this study was to size the monopolar plate (configuration "c") to have a deflection no greater than 0.1 mm when the EHC works at its operational pressure (700 bar). This design value should ensure wide physical contact between the MEA and the high-pressure monopolar plate.

As the plate material and the number of constrained points cannot be changed, the only way to ensure a deflection lower than 0.1 mm was to reduce the effective length of the plate as much as possible and to find its optimal (minimum) thickness. For this purpose, bolts' holes and gasket's groove, which ensures the gas tightening of the system, were taken into account.

Twelve high-strength M8 screws (class 10.9) with nuts and washers (with an external diameter of 16 mm) were chosen. The minimum diameter of the screw was calculated as:

$$d_{min} = 2\sqrt{\frac{pS}{n}\frac{\gamma}{\pi\sigma_y}} = 7.87\,\text{mm} \tag{3.7}$$

where:

- p is the pressure of 700 bar;
- S is 2507 mm^2 active area;
- n is the number of bolts;
- γ is a safety factor of 3;
- σ_y is the yield stress of the bolt material.

The gasket for the gas tightening of the EHC was chosen for axial load with internal pressure (Fig. 3.16). In this condition, O-rings do not allow the use of Back-up Rings to avoid the extrusion of the gasket in the gap between the components to be connected. Instead, some metal rings, used

as a deformable gasket in extreme static sealing situations, can increase their sealing capacity thanks to one or more coatings of materials, such as nickel, silver, gold, copper, and PTFE.

The metal ring was chosen to keep the groove width b as small as possible because it increases the plate's effective length (Fig. 3.16). The ring has a free height (cross-section diameter of the ring) of 2.38 mm and an external diameter inside the range of $25 \div 300$ mm. As reported in its technical data-sheet, the groove width is $b = 3.57$ mm, while the groove depth is $h = 1.83 + 0.08$ mm.

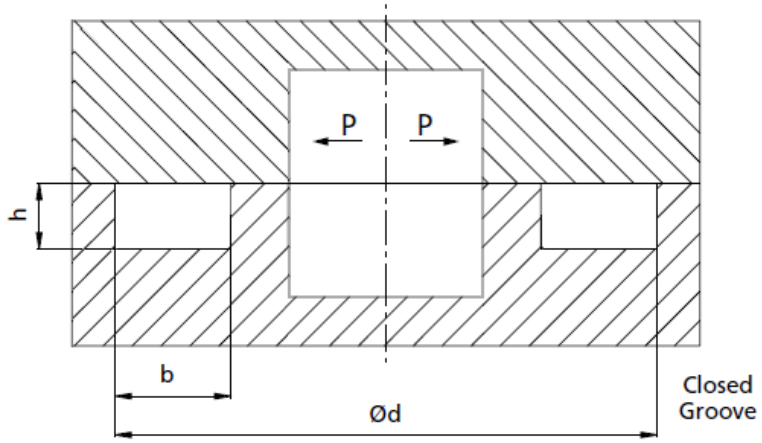

Figure 3.16: A not-scale representation of the gasket closed groove: h is the groove depth, b is the groove width and d is the groove diameter.

The external diameter of the groove was calculated as:

$$d = l_{MEA} + s + b \tag{3.8}$$

where l_{MEA} is the active area diameter, $s = 4$ mm is the height of the membrane annulus that it was needed to add to the active area, and b is the groove width.

Once known the external diameter of the groove, it will be possible to calculate the external diameter of the metal ring as:

$$d_r = d - 0.3 - 2t_c \tag{3.9}$$

where 0.3 mm is a clearance tolerance correction value and t_c is the maximum coating thickness if used.

The optimized sizing of the plate are shown in Fig. 3.17. The thickness of the plate has been set to 17 mm because results will show that the deflection

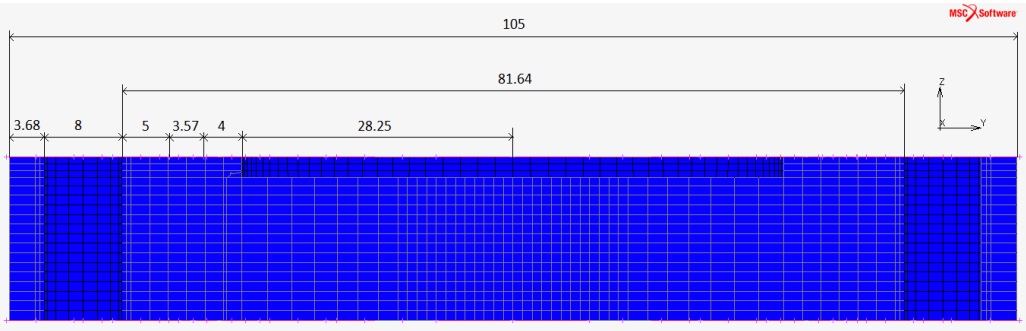

Figure 3.17: Optimized sizing of the plate: 28.25 mm is the active area radius, 4 mm is the height of the membrane annulus added to the active area, 3.57 mm is the groove width, 5 mm were left to give structural strength to the material before the 8 mm diameter holes for the bolts, 105 mm is the external diameter of the plate.

is less than 0.09 mm.

Once the geometry was defined, constraints were described more accurately than in the previous case to distribute contact stresses on a surface rather than in a point: both the body's bolts and the washers were represented with infinitely rigid surfaces, the former with cylinders, the latter with circles. Constraints were represented as a touching contact between the deformable surface of the plate and the infinitely rigid surfaces of bolts and washers, ensuring that the surfaces were correctly oriented.

Additional nodes on the bottom surface of the plate were constrained to avoid plate rotation during the simulation; in particular, it was locked:

- central node displacements in XY plane;
- displacement of a y-axis point along the x-axis;
- displacement of an x-axis point along the y-axis.

Part 2: results

Figg. 3.18 - 3.21 show the Von Mises stress, the deflection, the x-axis displacement and the equivalent strain distributions.

The maximum stress (Fig. 3.18) occurs:

1. at the center of the plate (about 250 MPa) due to the high pressure applied orthogonally to the surface;
2. in the contact areas (the automatic full-scale value, not represented in Fig. 3.18, is 695.7 MPa).

In both cases, stress values are higher than AISI 316 yield stress (σ_y = 200 MPa, Tab. 3.2). Despite this, the plate still has an elastic behavior.

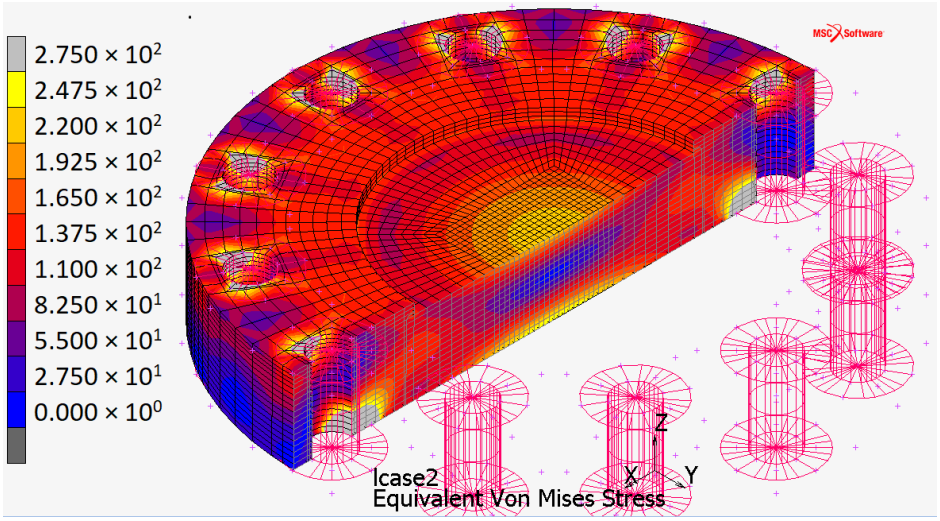

Figure 3.18: Von Mises stress distribution for the plate when constrained by touching contact with infinitely rigid surfaces.

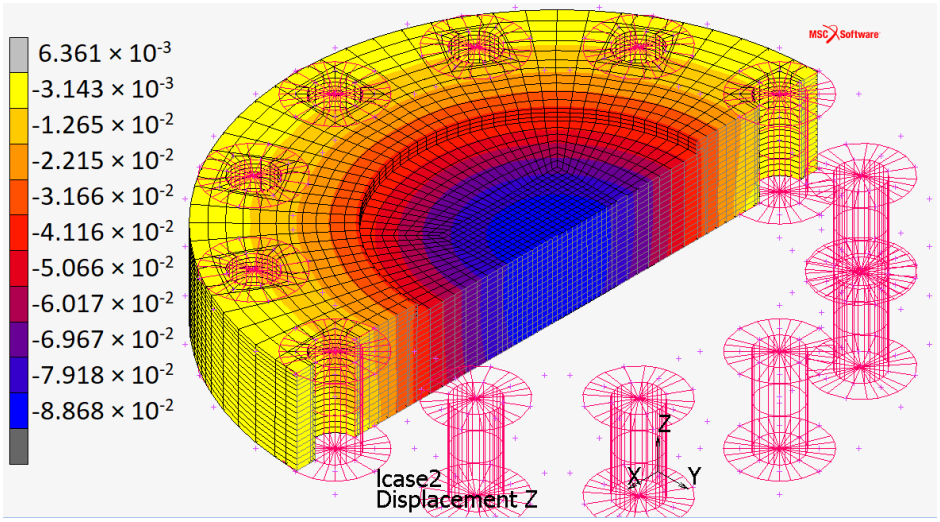

Figure 3.19: Deflection distribution for the plate when constrained by touching contact with infinitely rigid surfaces.

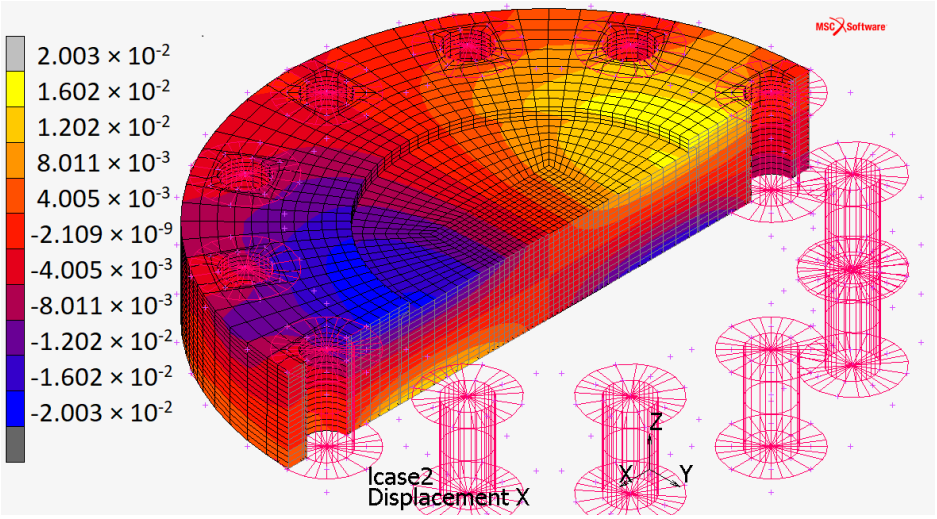

Figure 3.20: x-axis displacement distribution (it is the same along the y-axis, 90° rotated) for the plate when constrained by touching contact with infinitely rigid surfaces.

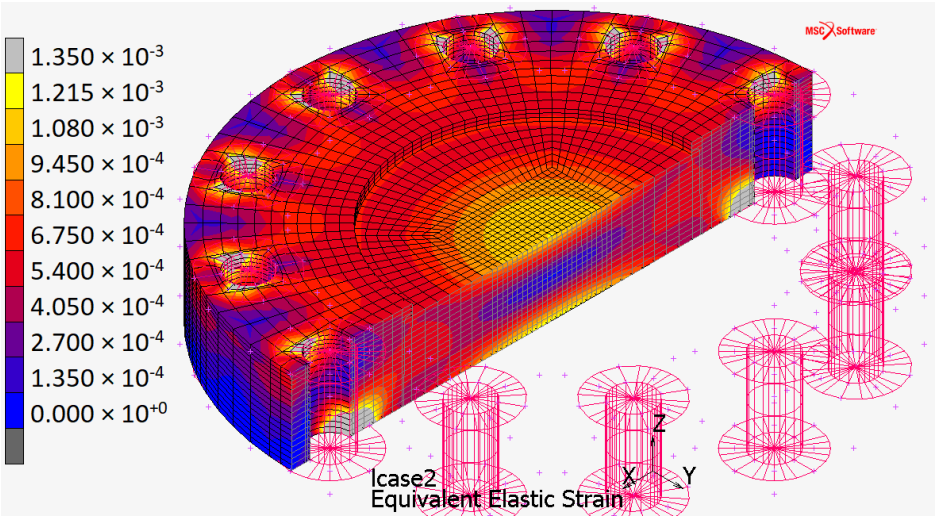

Figure 3.21: Equivalent strain distribution for the plate when constrained by touching contact with infinitely rigid surfaces.

The first case is a hydrostatic compression that does not plasticize the material: the area with the maximum deflection is unloaded in the central axial view of the plate because it is compressed so much above, so much below. This fact avoids the plastic behavior of the material even under stresses that moderately exceed the yield strength without triggering pressure-dependent brittle failure issues.

In the second case, the stress is due to the Hertzian contact between the plate and the rigid surfaces. It must not be compared with the yield stress but with the maximum allowable surface pressure of the material (p_{all}). As well as the maximum stress $\sigma_{z_{max}}$ acts orthogonally to the center of the contact ellipse, the other two main stresses also act, preventing lateral deformation. Consequently the equivalent stress due to Hertzian contact pressures (σ_{eq}) is lower than the $\sigma_{z_{max}}$.

As $\sigma_{z_{max}} = 517.2\,\text{MPa}$ and, according to [147], σ_{eq} is only 63-65% $\sigma_{z_{max}}$:

$$\sigma_{eq} = 63\%\sigma_{z_{max}} = 325.8\,\text{MPa} \tag{3.10}$$

Experimental relations link the maximum allowable surface pressure p_{all} to the material hardness ($HB = 215$ for AISI 316, see Tab. 3.2). One of these is [148]:

$$p_{all} = 2.76HB - 70 = 482\,\text{MPa} \tag{3.11}$$

or [149]:

$$p_{all} = 1HB + 190 = 390\,\text{MPa} \tag{3.12}$$

$$p_{all} = 1.52HB + 250 = 554\,\text{MPa} \tag{3.13}$$

For AISI 316 p_{all} is between 390 MPa and 550 MPa, higher than the equivalent stress $\sigma_{eq} = 325.8\,\text{MPa}$.

The simulation did not consider the second monopolar plate of the EHC, and infinitely rigid surfaces of washers constrained the top surface of the plate. The FEM simulation without top washers showed a 3.13% increase in deflection; hence the actual displacement along the z-axis will be within the range [0%, 3.13%].

Chapter 4

Thermal Energy Storage[1]

Thermal energy can be stored in three ways: thermochemical heat storage, sensible heat storage and latent heat storage.

The chemical heat accumulators use endothermic and exothermic reactions to store or release thermal energy. Substances such as silica gels, metal hydrides, zeolites and others are used [151]. The stored energy depends on the molar reaction enthalpy and the amount of substance. Small-scale applications (e.g., washing machines) already use chemical heat accumulators but are not ready for industrial use, and the technology is still in the research and development phase.

Sensible heat storage means storage whose energy absorption or release occurs with a noticeable change in the temperature of the operating medium. Depending on the application area, various substances can function as the operating medium, including water or molten salt. The stored energy depends on the specific heat capacity and the mass of the storage material. The sensible heat accumulators are currently used, for example, in solar power plants to store and buffer thermal energy with a capacity of up to 1000 MWh [152].

Latent heat accumulators use physical state change of the storage medium when storing or releasing thermal energy. A constant temperature characterizes heat transfer during phase change. The stored energy depends on the fusion enthalpy of the storage material and its mass.

4.1 Latent Heat Storage

Fig. 4.1 gives a schematic overview of different types of Phase Change Materials (PCM) used for latent heat storage. In most applications, the

[1]Part of this chapter is taken from [150], of which the Ph.D. candidate is an author.

phase transition is from solid to liquid or liquid to solid. This category of PCM is differentiated based on its chemical composition (organic and inorganic materials) and the temperature range. Both organic and inorganic materials can be further subdivided based on the characteristic behavior during the phase change. For example, eutectic mixtures and pure substances have a clearly defined solidification temperature; instead, mixtures of substances, such as paraffin wax mixtures or hydrate, have a temperature setting range. The organic and inorganic materials can also be divided into low-temperature and high-temperature materials based on their melting temperature. The low-temperature range extends from around $-50\,°C$ to $120\,°C$. Materials with a higher melting point belong to the high-temperature range.

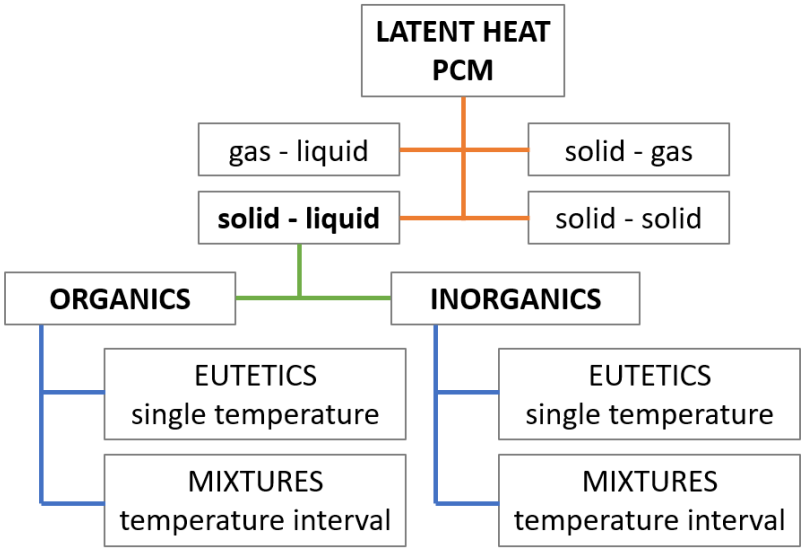

Figure 4.1: A schematic overview of Phase Change Materials used for latent heat storage.

Because they have very different properties, phase change materials must be accurately selected for every application [153, 154, 155]. Organic materials are chemically and thermally stable, do not interact corrosively with the PCM container, and have little or no tendency to supercool. However, the organic substances have a lower phase change enthalpy and higher flammability risk than the inorganic PCM.

Phase Change Materials are relatively inexpensive. Their main disadvantage is the low thermal conductivity. For example, the thermal conductivity of sodium nitrate ($NaNO_3$) is $0.56\,W/(m\,K)$. In comparison,

low-alloy steel (e.g., an evaporator tube made of $16\,Mo_3$) has about 80 times higher thermal conductivity. The low thermal conductivity highly affects the performance of latent heat storage: during the discharging process (Fig. 4.2), the PCM begins to solidify and a solid layer forms around the pipe (in general, heat transfer in solid materials is lower than in the liquid due to the lack of convection); as the discharge continues, the solid layer increases in thickness, further increasing the thermal resistance. Consequently, the heat flow decreases asymptotically, the discharging power becomes very small and the discharging time unusably long. A latent heat storage system can not operate in this condition, especially with small driving temperature differences.

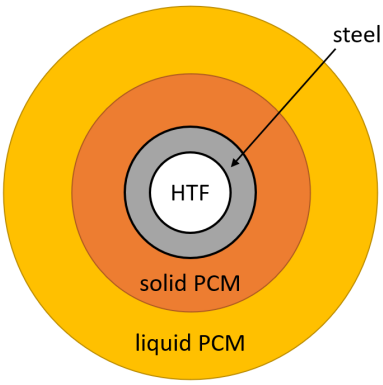

Figure 4.2: Solid PCM layer around the Heat Transfer Fluid (HTF) pipe.

In order to increase the performance of latent heat storage, many solutions have been identified over time, aiming to reduce melting and solidification times. This goal can be achieved in two different ways:

1. by improving the thermal conductivity of the PCM mass;
2. by increasing the contact area between the exchanger structure and the PCM mass.

The first solution increases thermal conductivity by adding more conductive additives, such as metal matrices [155], metal foams or metal rings. Their use significantly improves thermal conductivity, but they occupy a relatively large volume inside the PCM melt, reducing the storage capacity. Furthermore, they have a non-constant thermal conduction path because there is no defined connection from the evaporator tube to the metal structures. These structures are relatively expensive to manufacture and unsuitable for large-scale use [156].

Further improvements can be made by adding metal dust or carbon fiber structures [157]. These have some disadvantages: PCM and added

materials segregate due to differences in density; the melting temperature can change with metal dust additions. When using carbon fibers, thermal conductivity improvement is highly dependent on the spatial arrangement of the fibers. The use of these methods for large-scale industrial production is also unsuitable.

The second solution aims to increase the contact area between PCM mass and the heat conducting structure by encapsulating PCM inside a metal shell or using thermally conductive structures.

Encapsulation significantly increases the heat exchange surface. However, the manufacturing process is complex and, therefore, expensive. In addition, encapsulation must be able to manage the thermal expansion of the PCM. For example, the volumetric expansion of $NaNO_3$ upon melting is 10.7% [158]. Furthermore, an operating medium is required to heat exchange between PCM and HTF if HTF is water: direct water evaporation on the encapsulated PCM requires the storage to be designed and built as a pressure vessel of appropriate size.

A more promising technique is the PCM microencapsulation which increases heat transfer area, reduces PCM reactivity towards the outside environment and prevents PCM from leaking when it is in the liquid state. Microencapsulation is a process that allows for enclosing solid, droplet, liquid or gaseous PCM in a compatible thin solid wall. The material inside the MEPCM (MicroEncapsulated Phase Change Material) is called "core" and the wall is named "shell". In general, microencapsulation fabrication methods can be categorized into chemical, physico-chemical and physico-mechanical processes [159]. Dong et al. [160] proposed an optimized fabrication method for a MEPCM, as shown in Fig. 4.3.

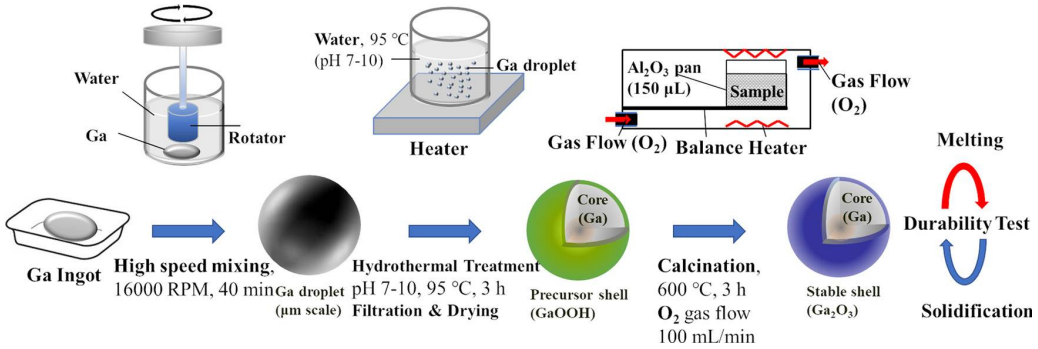

Figure 4.3: Schematic diagram of the Ga_2O_3 MEPCM fabrication process. The figure is taken from [160].

A Gallium ingot, used as a PCM, was mixed in a high-speed mixer to form Ga droplets. Then, Ga droplets were added to distilled water in a heated

PTFE container. The hydrothermal treatment continued with filtration and drying in order to obtain a precursor shell of GaOOH. Finally, the GaOOH MEPCM was calcined under an oxygen gas flow to form a stable Ga_2O_3 MEPCM using a thermogravimetry device.

Tests on MEPCM showed that the high rate of the heat storage capacity of the raw material was retained after encapsulation, preserving good stability in heat storage after many thermal cycles. Microencapsulation is expected to establish a new foundation for heat storage in the high-temperature region [161].

Another good solution to the heat conduction problem is using heat conduction structures connected to the heat transfer tube. They can generally be divided into radial and axial structures (Fig. 4.4). In the first case, the thermal conduction structure consists of many plates arranged transversely to the HTF pipe at a constant distance. The axial heat conduction structures are arranged along the longitudinal direction of the HTF pipe.

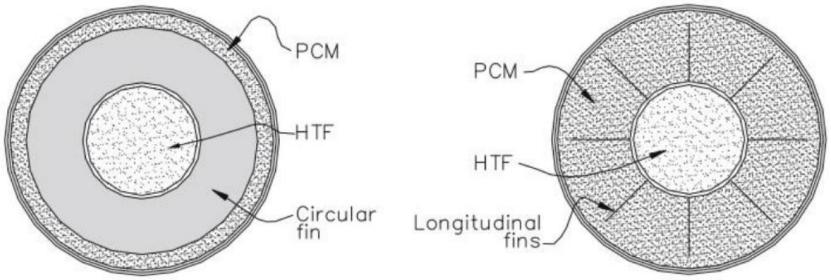

Figure 4.4: Heat conduction structures connected to the heat transfer tube: radial structure (left) and axial structure (right). The figure is taken from [162].

Comparison carried out in [162] showed that, during the melting process, the axial ribs were more efficient, enabling free convection, while free convection was largely suppressed in the radial ribs. During the solidification process, only heat conduction played a role since the free convection can be ten times lower than in the melting process [163].

Axial fins offer much more design flexibility. They can be unbranched, mono-branched, doubly-branched and various other shapes, manufactured (by extrusion) more cost-effectively than the radial structures. Design flexibility causes different PCM volume contents and surface configurations, making it difficult to compare the performance of the structures. For this reason, it is not easy to establish which structure is more efficient and economically more convenient.

Numerical analyses can help to evaluate the performance of different configurations. In this optic, Ph.D. research activity in the last months had the purpose of comparing three axial heat conduction structures in order to evaluate the most efficient in terms of maximum average discharging power. The three configurations have different fin shapes but the same radial dimensions to avoid different volume contents in metal and phase change material that would make difficult a proper comparison.

The remainder of the Chapter is organized as follows: Section 4.2 describes a Latent Heat Thermal Energy Storage (LH-TES) system developed inside an important European project, the CHESTER project; Section 4.3 explains how to model a solidification and melting problem; in particular, Subsection 4.3.1 describes the analytical model and the Newmann solution for the Classical Two-Phases (one-dimensional) Stefan Problem, that was analytically solved using a Matlab implementation of the analytical model (Subsection 4.3.2); then, the same physical problem was numerically simulated using Ansys Fluent software (Subsection 4.3.3); Subsection 4.3.4 reports the comparison of analytical and numerical results that validate the numerical model; once sure about the numerical model settings, the comparison of three axial heat conduction structures with different fin shapes was performed in order to evaluate the most efficient in terms of maximum average discharging power (Subsection 4.3.5). Subsection 4.3.6 shows the results of these last simulations.

4.2 The CHESTER project

Low-temperature heat storage tanks support many processes, such as cooling and air conditioning. They can be used to absorb peak loads (e.g., in refrigerated warehouses), protect electronic components from overheating, help air-conditioning building technology and store solar heat [153].

Phase change materials with an operating temperature of over 120 °C are used in industrial processes. They safeguard process parameters, for example, providing process steam in the event of an accident during power plant operation [164]. Another application area is thermal energy storage in solar power plants, where parabolic mirrors concentrate solar energy to generate process steam. The aim is to store surplus energy in order to increase the usage time of the solar power plant during the evening and night hours. The special feature of this type of power plant is the use of water as a heat transfer fluid.

The DLR deals with the design, research and development of pilot plants that allow the dispatchable supply of many different renewable energy sources through the combined use of electricity and heat. The CHESTER project, described in the following, was born for this purpose.

CHESTER project aims to develop, on the framework of energy consumption and 2020 targets for the use of renewable energy sources in Europe, a cost-competitive innovative system that will allow, through the combined use of electricity and heat, efficient energy management, storage, and dispatchable supply of many different RES (Fig. 4.5).

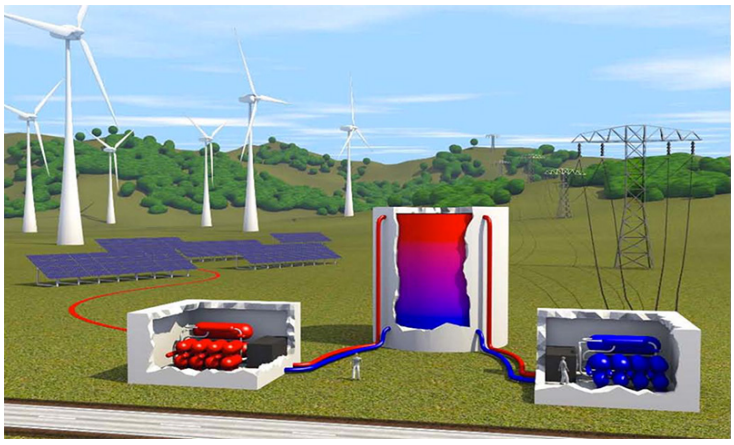

Figure 4.5: A schematic view of the CHESTER project system. The figure is taken from [165].

In general, when surplus electricity occurs, high-temperature heat can be generated to charge thermal energy storage. The stored heat can be reconverted when electricity is required (discharging process) through a thermal power cycle. Carnot efficiency defines the maximum roundtrip efficiency as the ratio of the net output power to the total input power (typically 40% for real systems) [10]. However, an emerging Carnot battery concept variant, called Pumped Thermal Energy Storage system, uses surplus electricity to increase the temperature level of a heat source (for example, seasonal pit storage charged by heat from solar thermal fields or industrial waste heat recovery systems). Heat is pumped by a heat pump, able to deliver much more than one unit of heat per unit of electrical energy consumed as the input electricity is not used to produce heat directly (for example, in a resistive electric radiator) but to transfer thermal energy between the evaporator and the condenser, working thanks to the heat contribution taken from the external environment. This allows the efficiency not to be longer limited by the Carnot efficiency, and a PTES system can ideally reach roundtrip efficiency (calculated as the ratio of the electrical energy generated during the discharging process to the electrical energy consumed during the charging process) of up to 100%.

Furthermore, a PTES system can receive thermal integration from low-temperature heat sources, for example, waste heat from industrial processes. In this case, the compression work during the charging process can be reduced and the efficiency (calculated as the ratio of the electrical energy generated during discharging process to the electrical energy consumed during charging process with integrated heat source) might thereby exceed 100%.

The CHEST system of the CHESTER project is a PTES system combined with the Smart District Heating to create a very flexible smart renewable energy management system. In this way, it can store electric energy with a roundtrip efficiency of 100% and even more, capable of converting power into heat, converting renewable low-temperature heat into power, and storing and delivering independently from each other upon request for both heat and power. Unlike pumped hydro and batteries, the system is expected to be site-independent and cyclically stable [165].

The CHEST system has three main components (Fig. 4.6):

- a high-temperature Heat Pump, equipped with an electrically powered compressor;
- a high-temperature Thermal Energy Storage system (with both latent and sensible heat storage);
- an Organic Rankine Cycle.

The system starts to charge the latent heat and the sensible heat TES at high temperature through the HT-HP that uses surplus electricity from

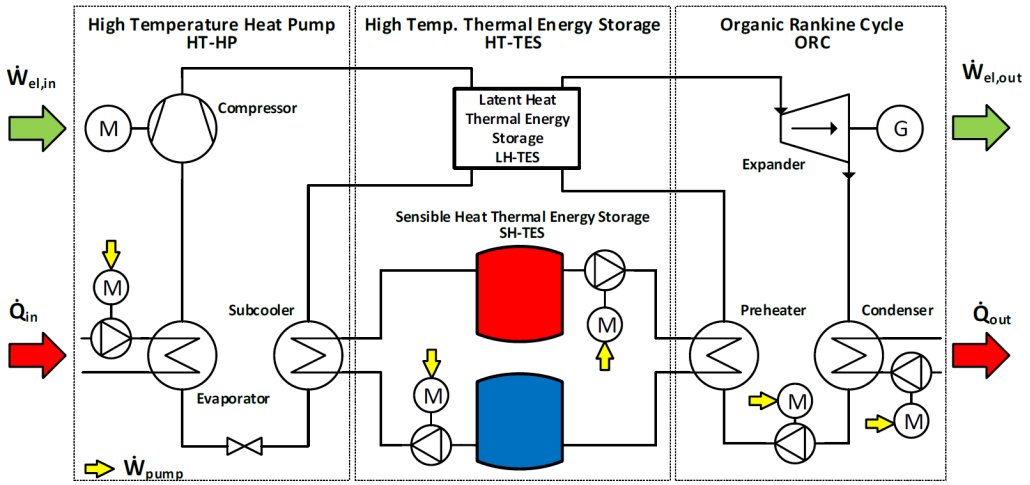

Figure 4.6: A conceptual diagram of the CHEST system. The figure is taken from [10].

the RES power grid (i.e., from wind or photovoltaic fields) when low power demand periods occur. The heat from seasonal pit storage, renewable sources or recovered waste heat is used as the HT-HP heat source (Fig. 4.7).

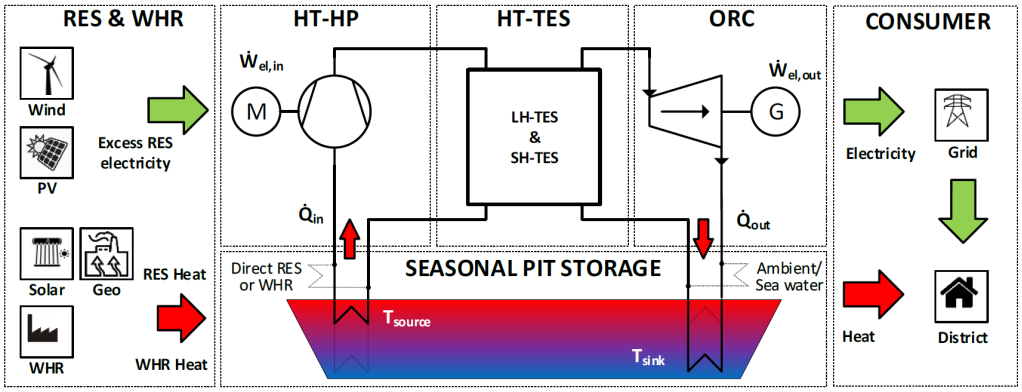

Figure 4.7: CHEST system integrated into a Smart District Heating. The figure is taken from [10].

The discharging phase uses the sensible heat TES as a pre-heater of an organic Rankine cycle (Fig. 4.6). Then the latent heat TES is used in its evaporation process. The ORC expander produces electricity and delivers it back into the grid.

The project started in April 2018. In 2021, DLR (Stuttgart, Germany) prepared the laboratory for integrating the individual CHEST technologies,

and worked on the piping between the individual technologies. The commissioning of the first-of-its-kind CHEST system was successfully carried out in December 2021, and the first operation of the overall system was planned for March 2022 [166].

4.3 Modeling of Phase Change Materials

The mathematical modeling of a phase change process aims to find the temperature field in the modeled material (with all the other heat transfer features), knowing the position over time of the moving frontier that separates the existing phases.

Processes of melting and freezing on a macroscopic scale concern numerous physical phenomena based on melting and solidification. During the phase change, the domain will be subdivided into liquid and solid regions, separated by an interface. The latent heat is absorbed (melting) or released (freezing) on the solid/liquid interface, so the moving interface characterizes the phase change process. Such problems have time-dependent boundary conditions and are known as "moving boundary problems" or "free boundary problems". Very few explicit analytical solutions are available for such problems in the literature. Their analysis requires knowing the initial temperature distribution and the thermal conditions on every exterior surface of the solid and liquid part of the body, also in the moving boundary, to have a well-posed mathematical problem.

The interface is the moving boundary of both the liquid and solid regions, and the following conditions are needed to complete the initial-boundary value problem [167]:

$$\lim_{\overrightarrow{x}_{\in liquid} \to interface} T(\overrightarrow{x}, t) = T_m \tag{4.1}$$

$$\lim_{\overrightarrow{x}_{\in solid} \to interface} T(\overrightarrow{x}, t) = T_m \tag{4.2}$$

where $T(\overrightarrow{x}, t)$ is the temperature depending on space and time, and T_m is the melting temperature.

The heat conduction equation is satisfied in each region, but a further condition (the interface position over time) is required to predict the temperature inside the liquid and the solid phases, as shown from the boundary limits in Eq. 4.1-4.2. This condition results from a heat balance across the interface and is known as the "Stefan condition".

4.3.1 Analytical solution of the Classical Two-Phases (one-dimensional) Stefan Problem

Stefan formulated the mathematical problem of finding the temperature field of a melting slab together with its solid/liquid interface history, determined as part of the solution [167]. The Classical Stefan Problem is

considered the prototype of all phase-change models, even if the closed-form explicit solutions (of similarity type) needs the following simplifying assumptions: one-dimensional and semi-infinite geometry, thermophysical properties constant in each region, constant melting temperature and latent heat, constant density in all the domain, uniform initial temperature, constant wall temperature, no internal heating source in the material, zero thickness sharp interface and heat transferring isotropically by conduction only (ignoring convection yields a conservative estimate of the melting speed).

In this thesis, the Classic Two-Phases Stefan Problem was considered in the one-dimensional case (Fig. 4.8): a semi-infinite slab ($0 \leq x < \infty$), initially solid at temperature $T_S < T_m$, is melted from the left ($x = 0$) by imposing a hot temperature $T_L > T_m$. The problem statement is to find a temperature distribution $T(x,t)$ and an interface function $X(t)$ that satisfy [167]:

Figure 4.8: A schematic representation of the Two-Phases 1-D Stefan Problem analytical model.

- the heat equation in both the liquid and the solid phases:

$$\frac{\partial T(x,t)}{\partial t} = \frac{k_L}{\rho c_L}\frac{\partial^2 T(x,t)}{\partial x^2}, \quad 0 < x < X(t), \quad t > 0 \tag{4.3}$$

$$\frac{\partial T(x,t)}{\partial t} = \frac{k_S}{\rho c_S}\frac{\partial^2 T(x,t)}{\partial x^2}, \quad x > X(t), \quad t > 0 \tag{4.4}$$

  where $c_{L/S}$ is the specific heat and $k_{L/S}$ is the thermal conductivity;

- the interface condition:

$$T(X(t),t) = T_m, \quad t > 0 \tag{4.5}$$

- the Stefan condition for one-dimensional case:

$$\rho L\frac{dX(t)}{dt} = -k_L\frac{\partial T(X(t),t)}{\partial x}\bigg|_- + k_S\frac{\partial T(X(t),t)}{\partial x}\bigg|_+, \quad t > 0 \tag{4.6}$$

where $\frac{\partial T(X(t),t)}{\partial x}\Big|_{\mp}$ represents the values of $\frac{\partial T(x,t)}{\partial x}$ as $x \to X(t)^{\mp}$

- the initial conditions:

$$X(0) = 0 \tag{4.7}$$

$$T(x,0) = T_S < T_m, \quad x > 0 \tag{4.8}$$

- the boundary conditions:

$$T(0,t) = T_L > T_m, \quad t > 0 \tag{4.9}$$

$$\lim_{x\to\infty} T(x,t) = T_S \quad t > 0 \tag{4.10}$$

The solution is the Neumann similarity solution that leads to the following transcendental equation for λ [167]:

$$\frac{Ste_L}{exp(\lambda^2)erf(\lambda)} - \frac{Ste_S}{\nu\ exp(\nu^2\lambda^2)erfc(\nu\lambda)} = \lambda\sqrt{\pi} \tag{4.11}$$

where:

- $Ste_{L/S}$ is the Stefan Number:

$$Ste_L = \frac{c_L(T_L - T_m)}{L}, \quad Ste_S = \frac{c_S(T_m - T_S)}{L}$$

- $\nu = \sqrt{\frac{\alpha_L}{\alpha_S}}$
- $erf(z)$ is the error function;
- $erfc(z) = 1 - erf(z)$ is the complementary error function.

The transcendental equation 4.11 is a strictly increasing function of $\lambda \geq 0$; therefore, it intersects any horizontal line exactly once, which means that the transcendental equation has a unique root (the similarity solution is unique), so, if a solution exists, it is the correct solution.

Once known λ, it is possible to calculate the solution by the following relationships:

- interface location:

$$X(t) = 2\lambda\sqrt{\alpha_L t}, \quad t > 0 \tag{4.12}$$

- temperature in the liquid region:

$$T(x,t) = T_L - (T_L - T_m)\frac{erf\left(\frac{x}{2\sqrt{\alpha_L t}}\right)}{erf\lambda}, \quad 0 < x < X(t), \quad t > 0 \quad (4.13)$$

- temperature in the solid region:

$$T(x,t) = T_S + (T_m - T_S)\frac{erfc\left(\frac{x}{2\sqrt{\alpha_S t}}\right)}{erfc(\nu\lambda)}, \quad x > X(t), \quad t > 0 \quad (4.14)$$

4.3.2 Matlab implementation of the analytical model

The analytical model of the Classic Two-Phases Stefan Problem (one-dimensional case) was implemented in Matlab. The main goal was to provide a tool to validate the numerical results obtained later from Ansys Fluent for the same physical problem.

The transcendental equation 4.11 is solvable by the Newton-Raphson iterative method, using the value $\sqrt{St/2}$ as initial approximation [167]. The Matlab script is reported in Appendix A and contains the Newton-Raphson function and the solution script for the Two-Phase 1-D Stefan Problem based on Eq. 4.12-4.14.

First of all, the Matlab script was run for a semi-infinite slab of Glauber's salt (sodium sulfate decahydrate, its thermo-physical properties are reported in Tab. 4.1), initially solid at temperature $T_S = 25\,^{\circ}\mathrm{C}$, then melted from the left ($x = 0$) by imposing a hot temperature $T_L = 90\,^{\circ}\mathrm{C}$. The Phase Change Material, boundary and initial conditions were chosen based on the example in [167]. This allowed making a comparison between the analytical results obtained from the Matlab script (Fig. 4.9 and Fig. 4.10) and the results reported in Fig. 2.2.4 and Fig. 2.2.5 of [167]. The correct match between figures lets us be sure about the good implementation of the analytical model.

Fig. 4.11 shows that the transcendental equation intersects the horizontal axis exactly once. As described in the previous subsection, the unique root must be the correct solution, so this is another proof of the good implementation of the model.

The Matlab script was then run for a semi-infinite slab of sodium nitrate (its thermo-physical properties are reported in Tab. 4.1), initially solid at temperature $T_S = 300\,^{\circ}\mathrm{C}$, then melted from the left ($x = 0$) by imposing a hot temperature $T_L = 350\,^{\circ}\mathrm{C}$. This Phase Change Material, of interest to the DLR Thermal Process Technology Department, was utilized

Table 4.1: Thermo-physical properties of sodium sulfate decahydrate ($Na_2SO_4\,10\,H_2O$) from [167] and sodium nitrate ($NaNO_3$), provided by the DLR Thermal Process Technology Department: ρ is the density [kg/m^3], c is the specific heat [J/(kg K)], k is the thermal conductivity [W/(m K)], L is the latent heat [J/kg], T_m is the melting temperature [°C].

		$Na_2SO_4\,10\,H_2O$		$NaNO_3$	
Symbol	Property	solid	liquid	solid	liquid
ρ	density	1460	1460	2010.5	2010.5
c	specific heat	1760	3310	1655	1655
k	thermal conductivity	2.16	0.59	0.56	0.56
L	latent heat	-	251210	-	178000
T_m	melting temperature	32	32	306	306

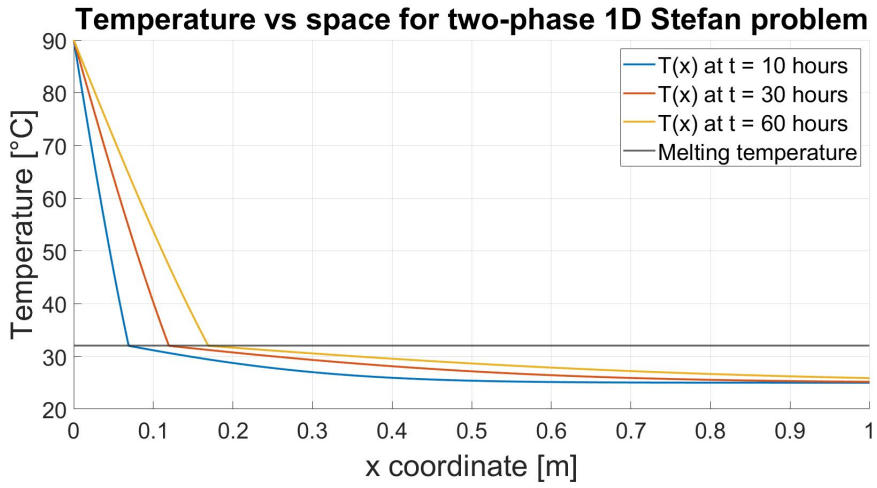

Figure 4.9: Temperature profiles at three times.

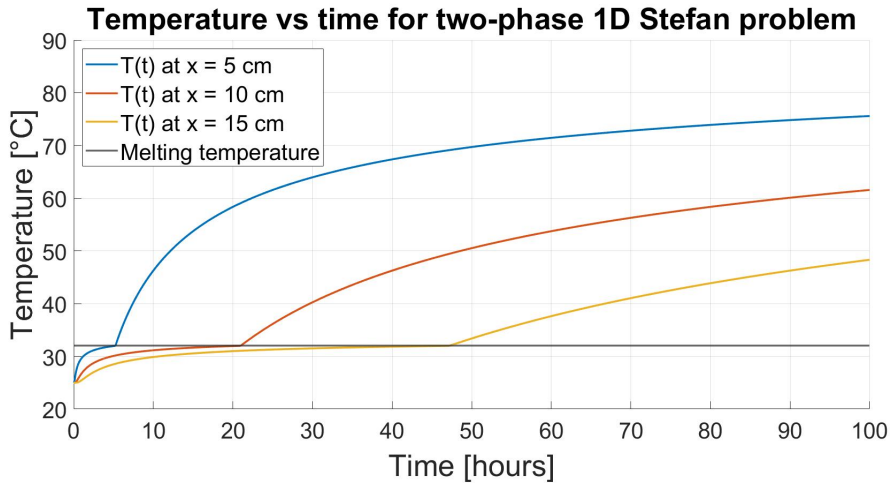

Figure 4.10: Temperature histories at three points.

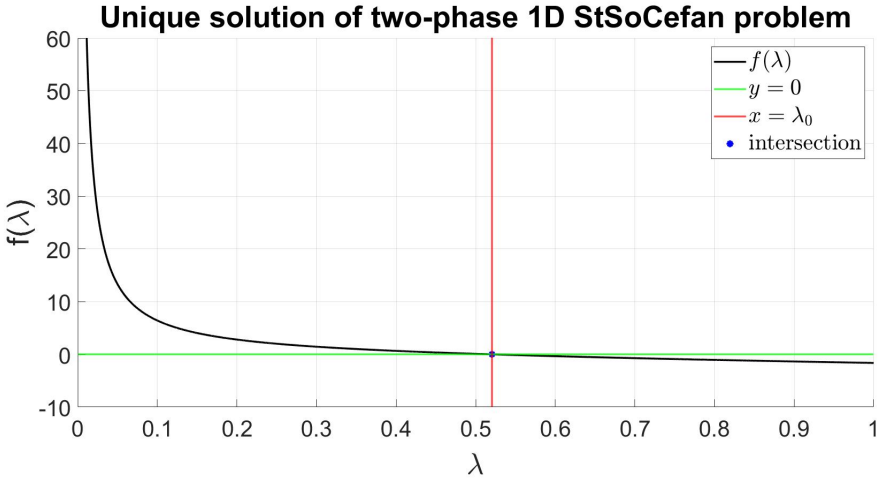

Figure 4.11: Unique solution of the two-phase 1-D Stefan problem.

for the numerical simulation on Ansys Fluent, as described in the next subsection. The comparison of results obtained from the Matlab analytical model and Ansys Fluent numerical simulation for the same boundary and initial conditions is reported in Subsection 4.3.4.

4.3.3 Numerical simulation for the 1-D problem

The numerical simulation has been performed by ANSYS FLUENT 2021 R1. ANSYS FLUENT is especially suitable for analyzing solidification and melting problems because it uses a dedicated model named *Solidification and melting*.

Solidification and melting model in Ansys Fluent

The solidification and melting model in ANSYS FLUENT uses an enthalpy-porosity technique to solve solidification and/or melting problems instead of tracking the moving frontier explicitly [168]. This method shows the phase change interface as a mushy porous zone where porosity is equal to the liquid fraction. The liquid fraction is associated with each cell in the computed domain and represents the fraction of the cell volume in liquid form. It changes from 0 to 1 during a melting process and from 1 to 0 during a solidification process.

The enthalpy-porosity formulation computes the liquid fraction iteration by iteration based on an enthalpy balance. When in a cell the material solidifies, the porosity becomes 0.

The energy equation for solidification and/or melting problems is written as [168]:

$$\frac{\partial(\rho H)}{\partial t} + \nabla \cdot (\rho \overrightarrow{v} H) = \nabla \cdot (k \nabla T) + S \tag{4.15}$$

where H is the enthalpy, ρ the density, $\overrightarrow{v}$ the velocity of the fluid and S the source term.

The enthalpy is calculated as:

$$H = h + \Delta H \tag{4.16}$$

where

$$h = h_{ref} + \int_{T_{ref}}^{T} c_p dT \tag{4.17}$$

is the sensible enthalpy (h_{ref} is the reference enthalpy, T_{ref} the reference

temperature and c_p the specific heat at constant pressure), instead

$$\Delta H = \beta L \tag{4.18}$$

represents the latent heat content (β the liquid fraction and L the latent heat of the material).

The liquid fraction is defined as:

- $\beta = 0$ if $T < T_{solidus}$
- $\beta = 1$ if $T > T_{liquidus}$
- $\beta = \frac{T - T_{solidus}}{T_{liquidus} - T_{solidus}}$ if $T_{solidus} < T < T_{liquidus}$

The relation between the enthalpy and the energy is given by [169]:

$$E = h - \frac{p}{\rho} + \frac{v^2}{2} \tag{4.19}$$

Numerical simulation of the Two-Phases 1-D Stefan Problem

The modeling started creating the geometry with the Design Modeler tool provided by ANSYS. As shown in the schematic diagram in Fig. 4.12, the PCM domain was a rectangle (10x3 cm^2). The domain length was taken seven times as long as the area melted during the simulation to preserve the semi-infinite nature of the model. The domain height was chosen to make the system's behavior nearly 1D along the horizontal centerline, where results were used for the comparison with Two-Phases 1-D Stefan Problem analytical model.

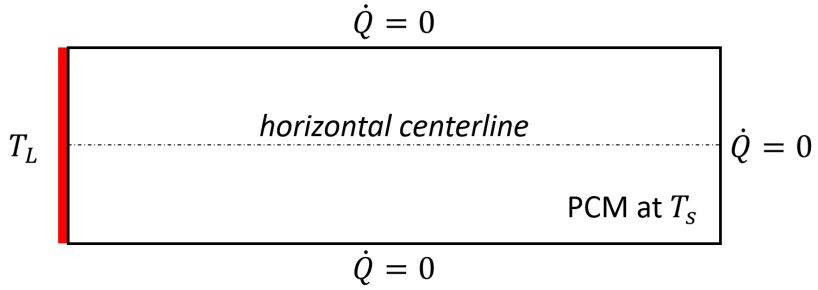

Figure 4.12: A schematic representation of the Two-Phases 1-D Stefan Problem numerical model.

The mesh was generated using uniform quadrilaterals with an element size of 0.04 cm.

The problem is solved by the finite volume method using ANSYS FLUENT 2021 R1. The procedure followed for the model setup is described in the following:

- in *General*, the solver was set to time-transient and 2D-planar analyses. The gravity contribution was not considered;
- in *Models*, the solidification and melting model was set to on, automatically enabling the energy model; the viscous flow model was changed from SST k-omega to laminar;
- in *Materials*, the phase change material ($NaNO_3$) was created, uploading the properties reported in Table 4.1;
- in *Boundary Conditions*, the left wall temperature T_L was set to 623.15 K (350 °C), while the top, right and bottom sides were perfectly insulated (heat flux equal to zero);
- in *Solution Methods*, pressure and velocity coupling was realized by the SIMPLE algorithm. Momentum and energy equations were discretized using a second-order upwind interpolation scheme, while the pressure equation was solved with the second-order method. The gradient discretization adopted the least-squares-cell-based method. The transient formulation that discretized the governing equations used the implicit first-order Euler method;
- in *Solution Controls*, all the under-relaxation factors were left to the default values;
- in *Solution Initialization*, the initial value of T_S was set to 573.15 K (300 °C).

Calculations were performed using an adaptive CFL-Based method for Time Advancement with incremental time steps. The time step was set to 0.1 s for 18 000 time steps (total flow time: 1800 s = 30 min). The maximum number of iterations per time step was set to 30. Convergence was obtained when the residual of equations was less than 1e-6.

Fig. 4.13 and Fig. 4.14 show respectively temperature and liquid fraction contours at 5 min, 10 min, 20 min and 30 min.

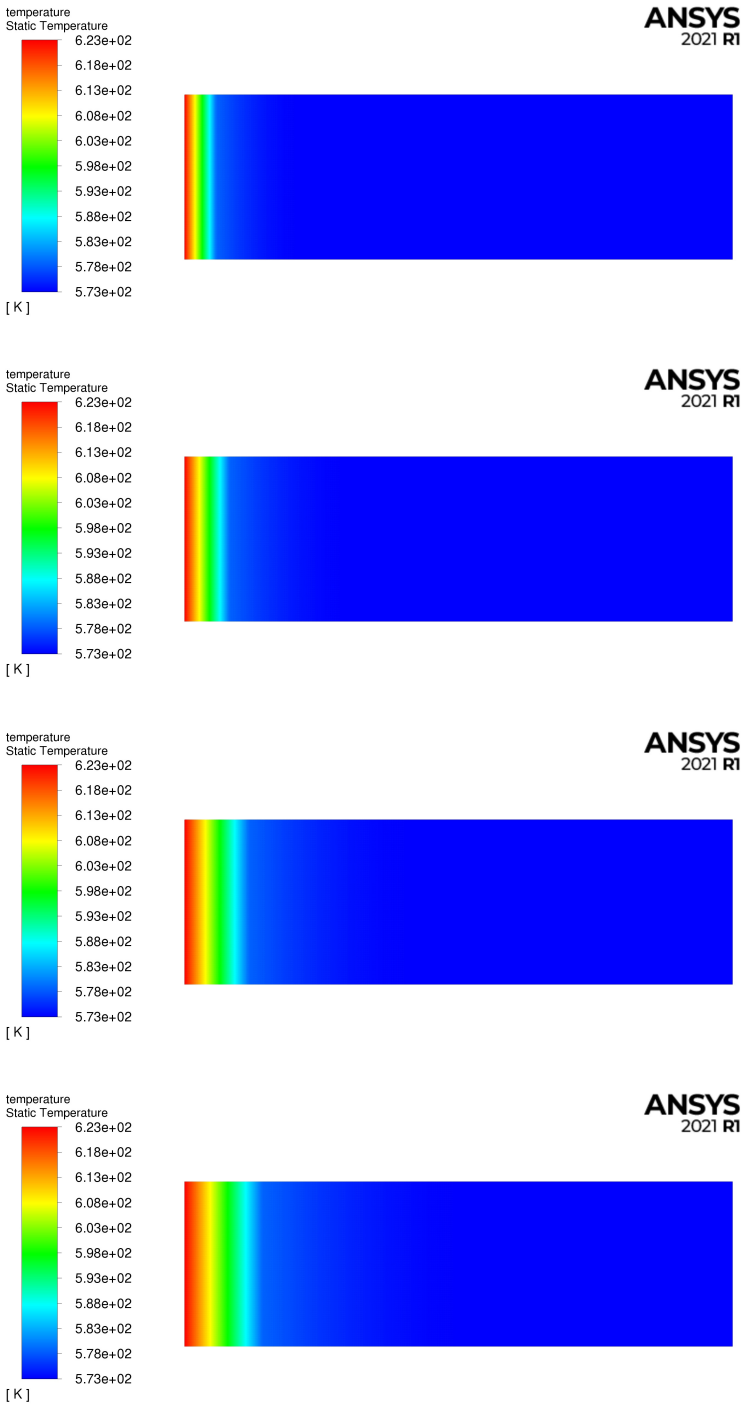

Figure 4.13: Temperature contours at 5 min, 10 min, 20 min and 30 min.

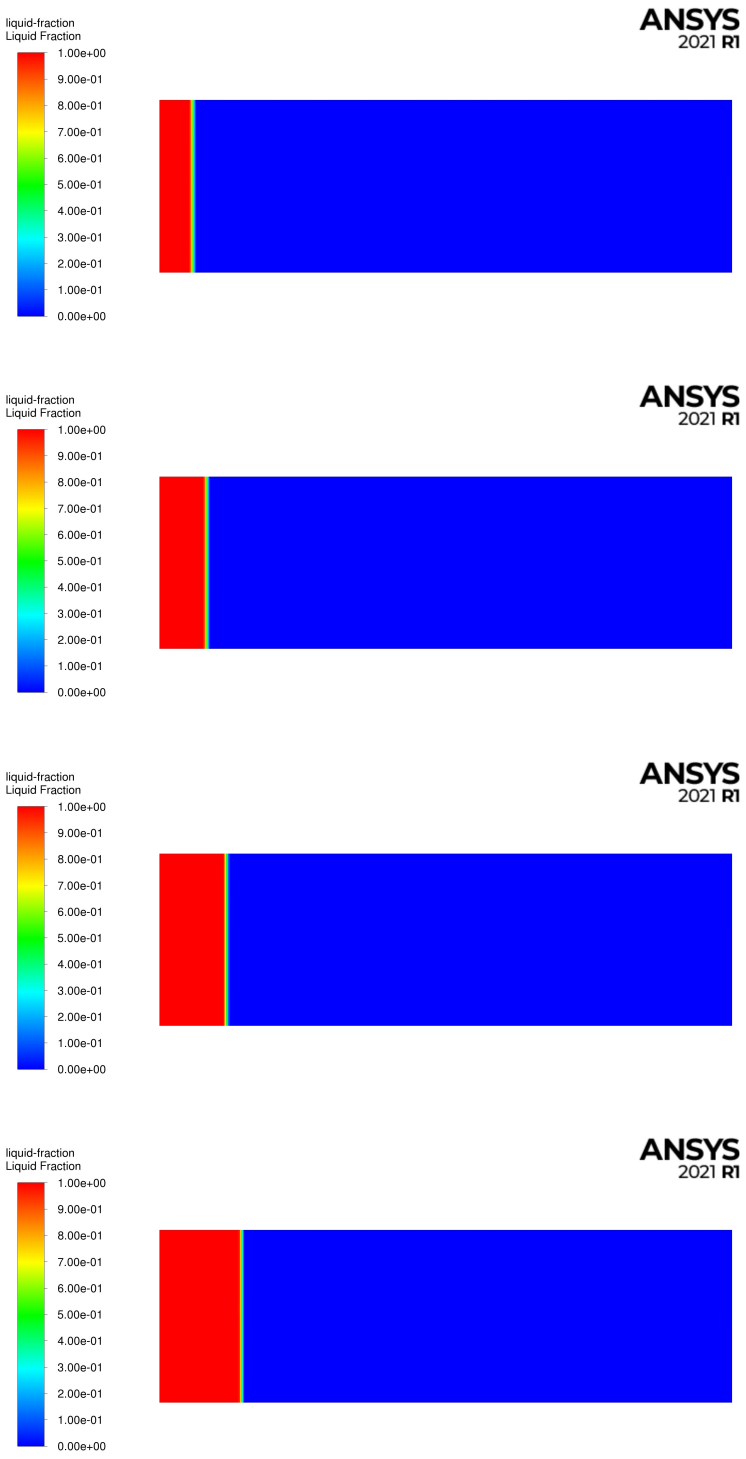

Figure 4.14: Liquid fraction contours at 5 min, 10 min, 20 min and 30 min.

4.3.4 Validation of the numerical model

Fig. 4.15 plots the temperature profile along the x coordinate, calculated from both the analytical and numerical models at 5 min, 10 min, 20 min and 30 min.

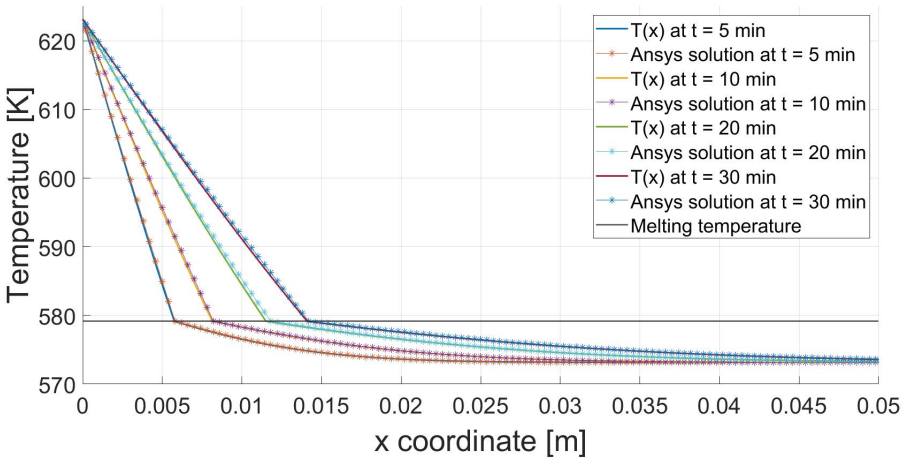

Figure 4.15: Temperature profiles at 5 min, 10 min, 20 min and 30 min.

The maximum computational error on the temperature field at a time t_i can be defined as [170]:

$$E_T(t_i) = max(e_T(x_1, t_i), e_T(x_2, t_i), ..., e_T(x_n, t_i))$$

where

$$e_T(x_i, t_i) = \frac{|T_{an}(x_i, t_i) - T_{num}(x_i, t_i)|}{T_L - T_S}$$

x_i is the i-th point of the discretized domain alond the horintal centerline, $T_{an}(x_i, t_i)$ and $T_{num}(x_i, t_i)$ are the temperature results calculated in the i-th point of the discretized domain at a time t_i respectively from the analytical and numerical models.

Tab. 4.2 shows the maximum computational error on the temperature field at 5 min, 10 min, 20 min and 30 min. The x coordinates and the temperature values corresponding to the calculated maximum errors are reported in Fig. 4.16. All the errors are less than 2%, indicating the goodness of the correspondence between numerical and analytical results.

Fig. 4.17 plots the frontier position over time, calculated from both the analytical and numerical models (at 5 min, 10 min, 20 min and 30 min).

The maximum computational error on the interface position can be defined as [170]:

Table 4.2: Maximum computational error on the temperature field at 5 min, 10 min, 20 min and 30 min.

Error	t = 5 min	t = 10 min	t = 20 min	t = 30 min
E_T	1.16%	1.09%	1.93%	1.03%

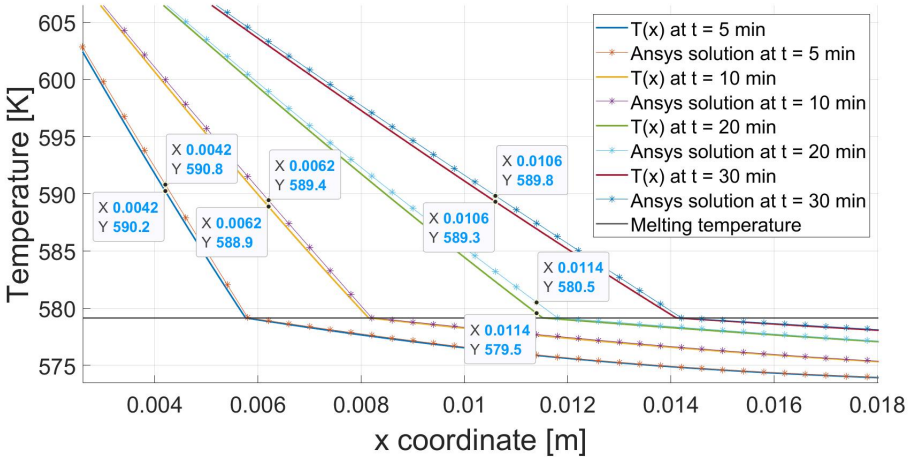

Figure 4.16: Detailed view of the maximum computational errors on the temperature field at 5 min, 10 min, 20 min and 30 min.

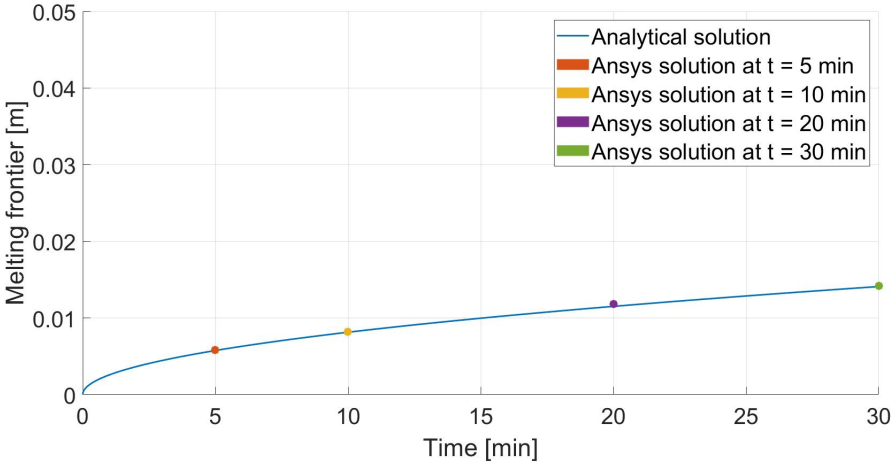

Figure 4.17: Melting frontier position over time for Two-Phase 1D Stefan Problem.

$$E_X = max(e_X(t_1), e_X(t_2), ..., e_X(t_n))$$

where

$$e_X(t_i) = \frac{|X_{an}(t_i) - X_{num}(t_i)|}{X_{an}(t_i)}$$

t_i is the i-th time of the simulation, $X_{an}(t_i)$ and $X_{num}(t_i)$ are the interface position calculated at time t_i respectively from the analytical and numerical models.

Tab. 4.3 shows the computational errors on the interface position at 5 min, 10 min, 20 min and 30 min. Also in this case, all the errors are small (the maximum computational error E_X is 2.5%).

Table 4.3: Computational errors on the interface position at 5 min, 10 min, 20 min and 30 min.

Error	t = 5 min	t = 10 min	t = 20 min	t = 30 min
E_X	0.76%	0.73%	2.5%	0.71%

The validation of the results obtained from the numerical simulations allows being confident about the correctness of the numerical model settings described in Subsection 4.3.3. The same settings can be used for studying a more complicated geometry in a more interesting problem. It is the topic of the following subsection.

4.3.5 Numerical simulations for the finned tube

Sure about the numerical model settings described in Subsection 4.3.3, the research work aims now to study a more interesting problem, which means evaluating the performance of different latent heat TES configurations during the discharging process: the system, initially charged (it means all PCM is liquid), undergoes a sudden decrease of temperature, starting to discharge (solidification process) and realizing heat to the Heat Transfer Fluid. The thesis aims to find the most efficient latent heat TES configuration in terms of maximum average discharging power.

Based on the heat conduction structure type used in the CHESTER project (axial type), the analysis deals with three different axial structures connected to the heat transfer tube (one of the three two-dimensional geometry is shown in Fig. 4.18). All the geometries consist of:

- a steel inner tube in which the Heat Transfer Fluid flows (it does not change in the comparison);
- an aluminum heat conduction structure connected to the heat transfer tube;
- the PCM all around the aluminum structure up to its outer radius.

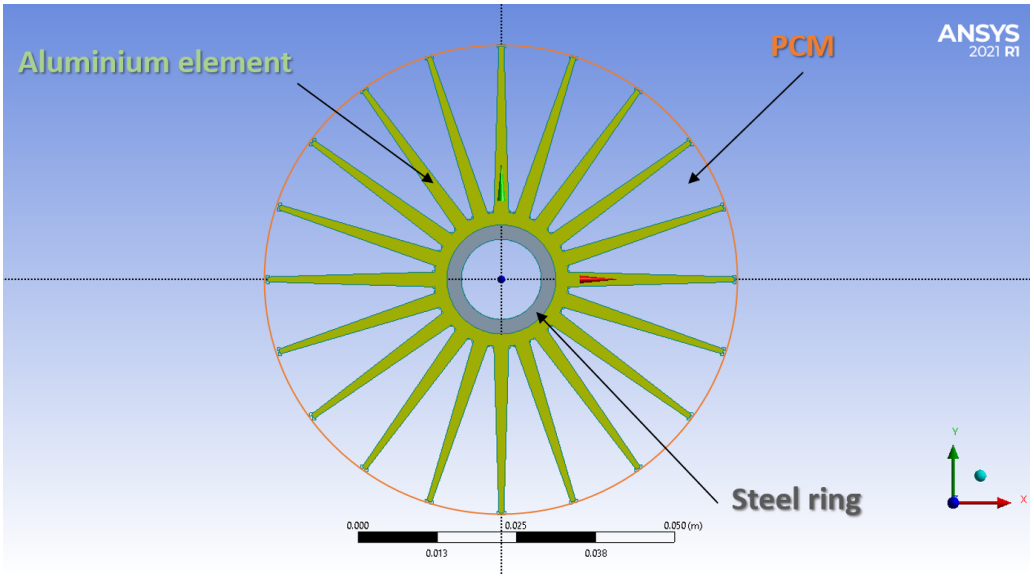

Figure 4.18: One of the three different geometries studied in the present work. It has a steel inner tube for Heat Transfer Fluid flow (grey element) and an aluminum heat conduction structure connected to the heat transfer tube (green component). The PCM is all around the aluminum structure up to its outer radius.

Geometries were sized with the following criteria:

- they change only for the fin shape (rectangular, trapezoidal and fractal fins);
- the three different structures connected to the heat transfer tube have the same volume fraction;
- the PCM mass is constant in all the configurations, which means that the PCM volume fraction is also constant.

The volume fraction is calculated as:

$$V_{\%,x} = \frac{A_x L}{A_{max} L} = \frac{A_x}{A_{max}}$$

where x stands for steel, aluminum and PCM, A_x is the surface area covered by x-material, A_{max} is the surface area of the cycle that has the distance from the fin tip to the tube center as radius and L is the length of the TES system (it will be considered equal to 1 m for the calculation of the total discharging power).

As stated before, the volume fractions are kept constant for all the configurations (it means constant radial dimensions) in order to perform a proper comparison that evaluates only the shape of the fins. Tab. 4.4 reports the constant parameters for the three configurations.

Table 4.4: Constant parameters for the three configurations under study.

Steel ring	R_{min}	0.0063	m
	R_{max}	0.0086	m
	area	0.0001076616	m^2
Aluminum ring	R_{min}	0.0086	m
	R_{max}	0.0106	m
Aluminum fins	*number*	20	m
	R_{inner}	0.0106	m
	R_{outer}	0.0525	m
Total aluminum structure	*area*	0.00091644	m^2
PCM	R_{min}	0.0106	m
	R_{max}	0.0525	m
	area	0.00751032	m^2

Again, numerical simulations have been performed by ANSYS FLUENT 2021 R1. Geometry domains, created with the Design Modeler tool, represent only a section of the total domain, thanks to the symmetry of the model. In

particular, the drawn section considers the fin's half-thickness and the PCM area's half-angle between two fins, as shown in Fig. 4.19 for one of the three configurations. The angle of the simulated section is 9° as all the models have 20 fins.

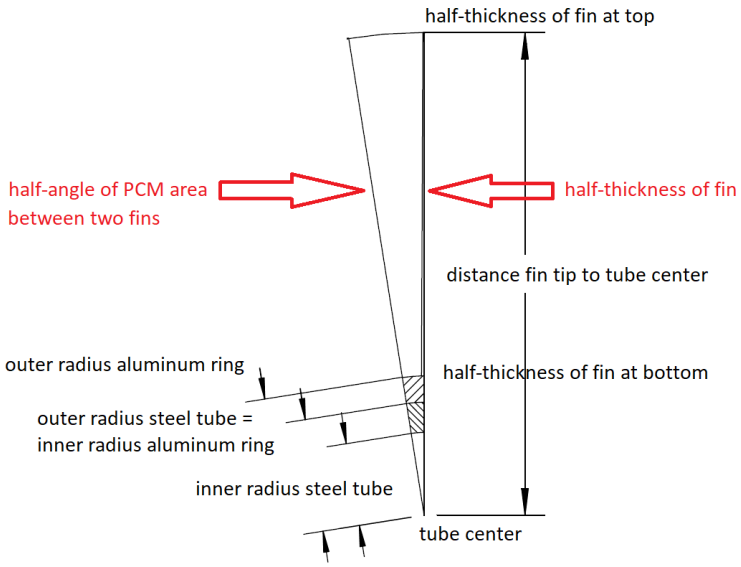

Figure 4.19: Simulated section of 9° for a model with 20 fins. It considers the fin's half-thickness and the PCM area's half-angle between two fins.

Once completed a drawing in Design Modeler, the three domains (steel aluminum and PCM) have been selected to make all into one part; in this way, Ansys Fluent does not solve equations in the contact regions but just considers the thermophysical properties changes between domains.

According to all the previous considerations, the simulated domains for the three axial structures are reported in Fig. 4.20. It is fair to point out that the geometry used in the latent heat TES of the CHESTER project is a rather complex branched fin geometry with a double tube heat exchanger, too complex for the purpose of a three-months mobility scheme. In any case, geometries shown in Fig. 4.20 represent a necessary starting point for the finned tube numerical simulations.

The meshes, generated using non-regular quadrilaterals elements with an element size of 0.04 cm, have a number of nodes and elements reported in Tab. 4.5 for each configuration.

The problem is solved by the finite volume method of ANSYS FLUENT, using the same settings of the 1D model reported in Subsection 4.3.3. Also in these simulations, convection is neglected. In the 1D model,

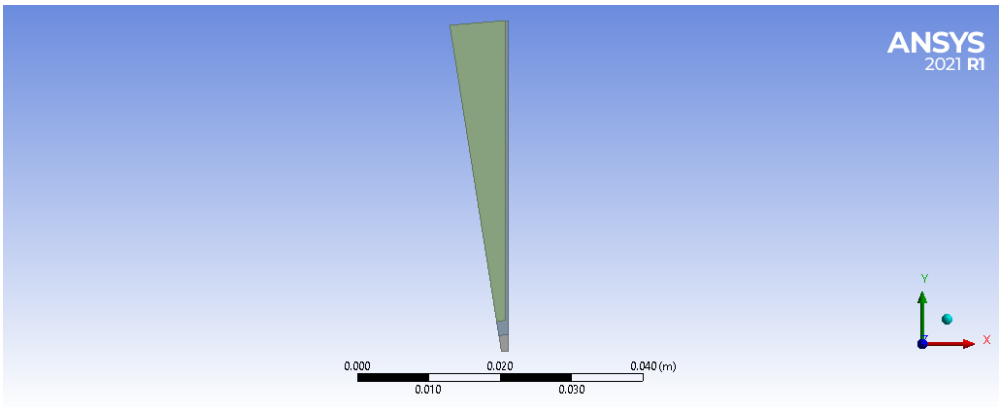

(a) Simulated domain for the first configuration: rectangular fin profile.

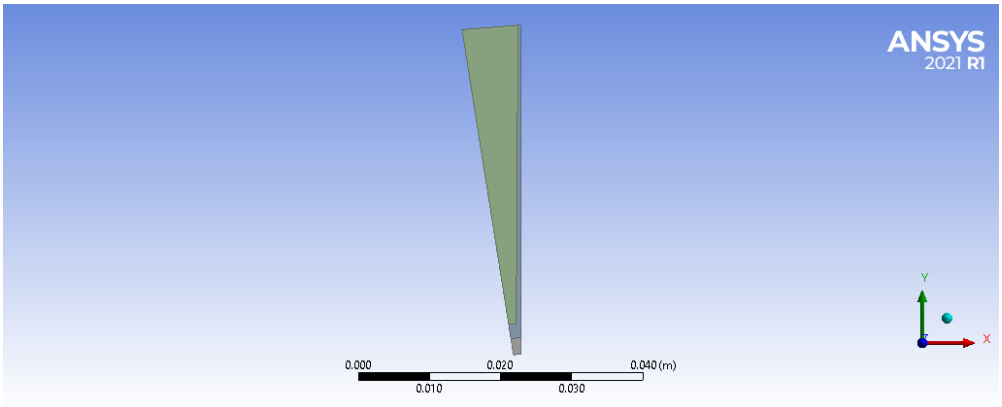

(b) Simulated domain for the second configuration: trapezoidal fin profile.

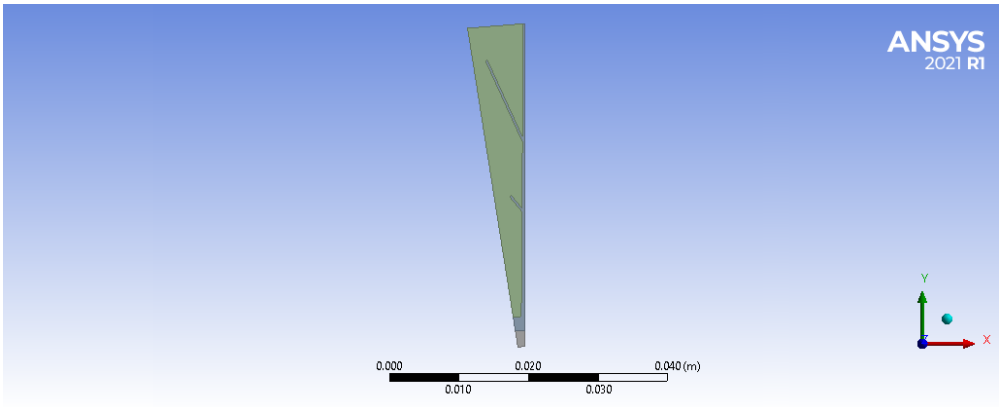

(c) Simulated domain for the third configuration: fractal fin profile.

Figure 4.20: Simulated domains for the three axial structures under study.

Table 4.5: Number of nodes and elements of the mesh for each configuration.

	Rectangular fins	Trapezoidal fins	Fractal fins
Nodes	16409	16622	17096
Elements	5308	5383	5543

the reason for ignoring convection was to perform the comparison with the analytical model of the Classical Two-Phases Stefan Problem, in which equations cannot take into account convection (see the simplifying assumptions described in Subsection 4.3.1). Here, the system is perfectly insulated (no thermal flow, no heat dispersion, no border effects), except for the wall in which the discharging temperature is applied; furthermore, as initial condition, the PCM domain is totally liquid but at the same temperature (no thermal gradient). Accordingly to these assumptions, it is reasonably possible to neglect convection, considering that this choice yields a conservative estimate of the melting speed.

$NaNO_3$ is the Phase Change Material used for finned tube simulations (its properties are reported in Tab. 4.1). It was initially liquid at temperature $T_L = 573.16\,\mathrm{K}$, $0.01\,\mathrm{K}$ more than the melting temperature ($T_m = 573.15\,\mathrm{K}$) in order to have 100% liquid fraction at time $t = 0$ on ANSYS FLUENT simulator.

As boundary conditions, a temperature difference of $-10\,\mathrm{K}$ is imposed at the inner radius of the steel ring while all the other boundaries are perfectly insulated (Heat Flux equal to zero).

The calculations were performed using an adaptive CFL-Based method for Time Advancement with incremental time steps. The time step was set to $0.1\,\mathrm{s}$ for $48\,000$ time steps (total flow time: $4800\,\mathrm{s} = 80\,\mathrm{min}$).

4.3.6 Results and discussion

Fig. 4.21 and Fig. 4.22 show respectively temperature and liquid fraction contours at 5 min, 10 min, 15 min, 20 min, 30 min, 40 min, 50 min and 60 min for rectangular fin profile geometry. At t = 60 min all the PCM is discharged (liquid fraction equal to 0%, Tab. 4.6).

Fig. 4.23 and Fig. 4.24 show results for trapezoidal fin profile geometry. Also in this case, all the PCM is discharged at t = 60 min; furthermore, the liquid fraction is slightly always lower than in the previous case (Tab. 4.6). It means that the trapezoidal fin profile performs more than the rectangular one.

Fig. 4.25 and Fig. 4.26 show results for fractal fin profile geometry. In this case, the profile seems to be worse than the previous configurations, but only at the beginning of the discharging process (t < 15 min); indeed, from t = 15 min, the performance of the fractal fin profile is the best. This behavior is due to the different distribution of the aluminum material between configurations: the non-fractal profiles have more aluminum content near the connection with the heat transfer tube where the phase change starts, so the thermal exchange is faster at the beginning of the solidification process. On the contrary, the fractal profile has lower aluminum content at the bottom of the fins because of the branches (the aluminum fraction is constant for all the configurations), but the branches are responsible for faster thermal exchange when the solidifying frontier moves away from the steel ring.

Table 4.6: Liquid fraction evolution over time for the three configurations under study.

	Rectangular fins	Trapezoidal fins	Fractal fins
5 min	76.16%	75.00%	75.94%
10 min	61.02%	59.41%	60.09%
15 min	48.87%	47.09%	46.90%
20 min	38.71%	36.94%	35.51%
30 min	22.74%	21.26%	16.21%
40 min	11.29%	10.24%	4.18%
50 min	3.62%	3.01%	0%
60 min	0%	0%	0%

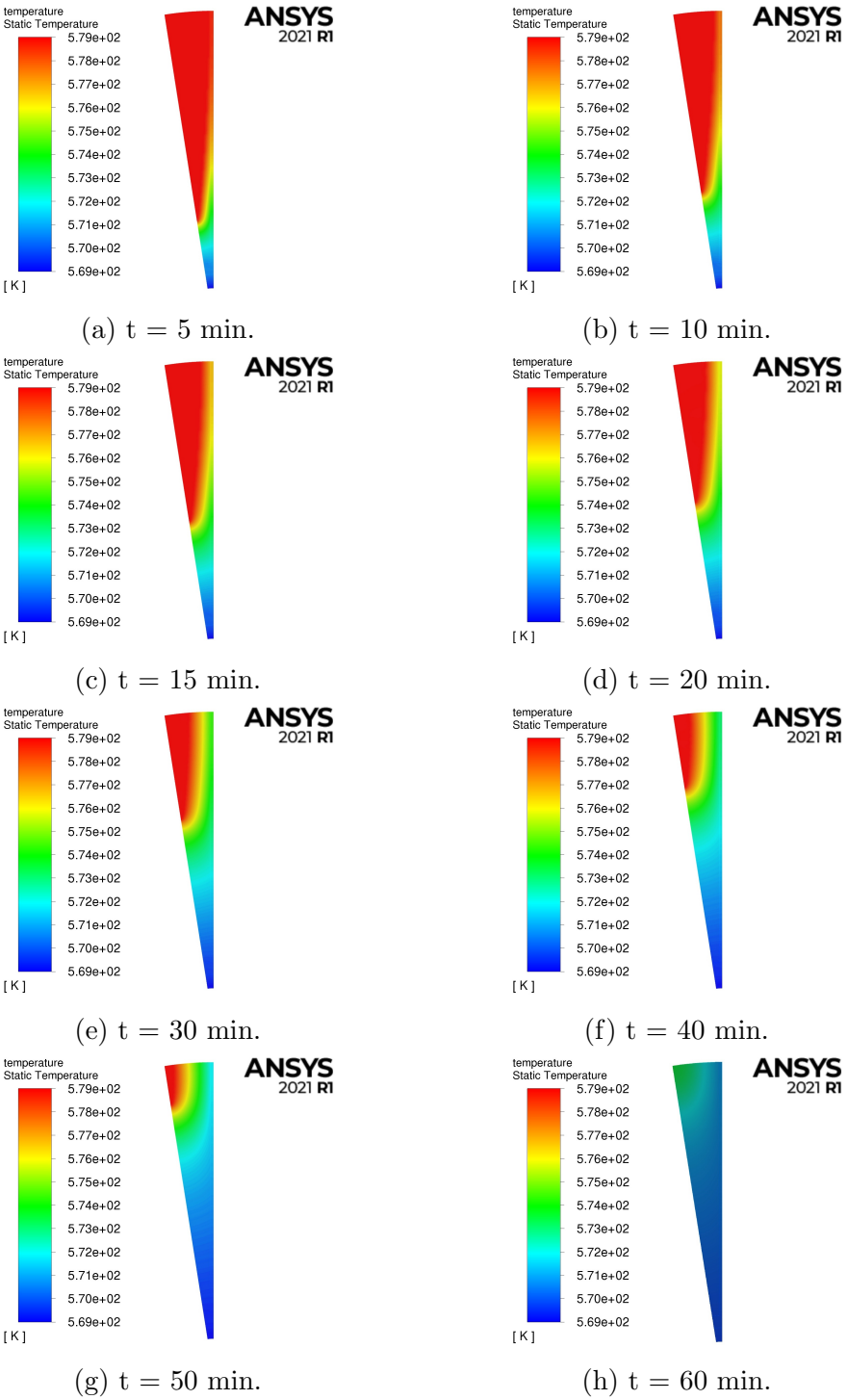

(a) t = 5 min. (b) t = 10 min.

(c) t = 15 min. (d) t = 20 min.

(e) t = 30 min. (f) t = 40 min.

(g) t = 50 min. (h) t = 60 min.

Figure 4.21: Temperature contours for the rectangular fin profile geometry at 5 min, 10 min, 15 min, 20 min, 30 min, 40 min, 50 min and 60 min.

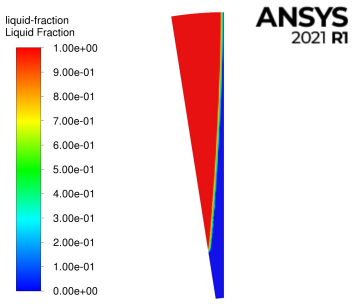

(a) t = 5 min, LF = 76.16%.

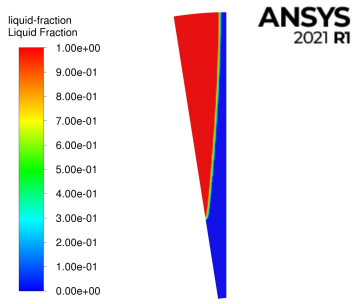

(b) t = 10 min, LF = 61.02%.

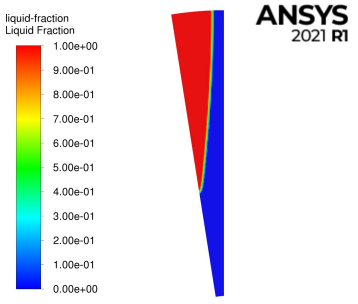

(c) t = 15 min, LF = 48.87%.

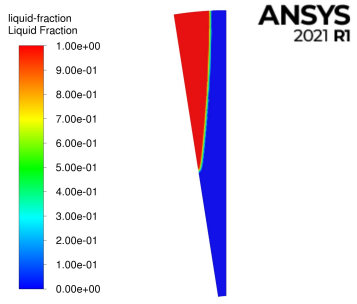

(d) t = 20 min, LF = 38.71%.

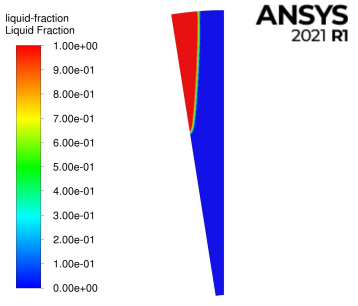

(e) t = 30 min, LF = 22.74%.

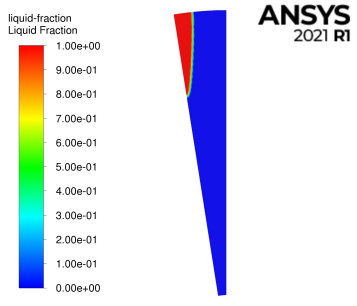

(f) t = 40 min, LF = 11.29%.

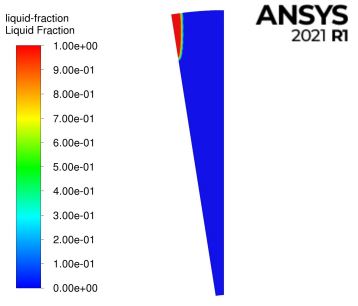

(g) t = 50 min, LF = 3.62%.

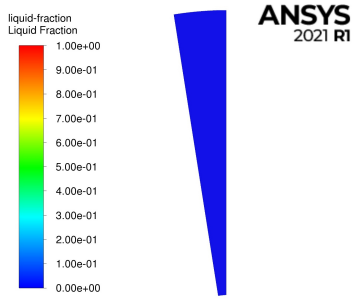

(h) t = 60 min, LF = 0%.

Figure 4.22: Liquid fraction contours for the rectangular fin profile geometry at 5 min, 10 min, 15 min, 20 min, 30 min, 40 min, 50 min and 60 min.

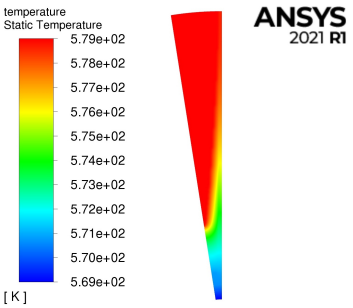

(a) t = 5 min.

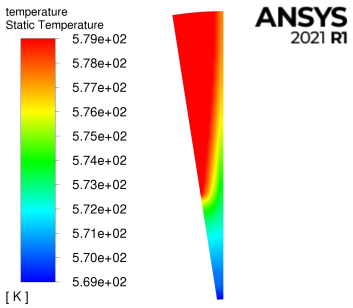

(b) t = 10 min.

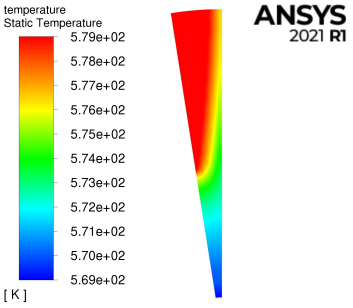

(c) t = 15 min.

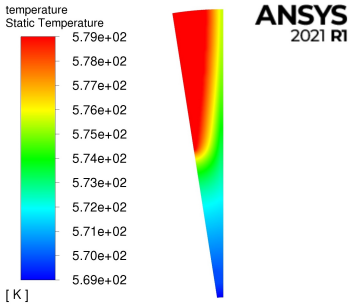

(d) t = 20 min.

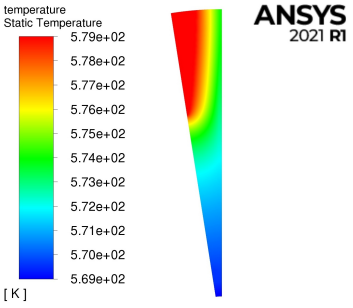

(e) t = 30 min.

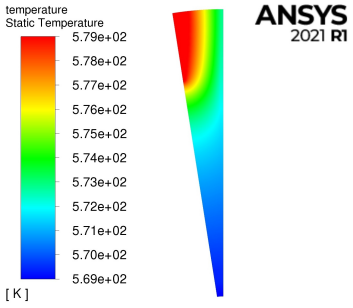

(f) t = 40 min.

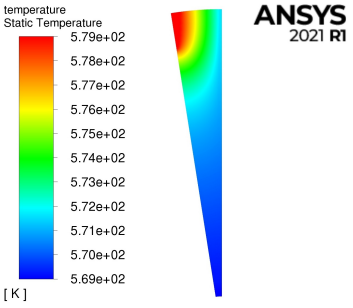

(g) t = 50 min.

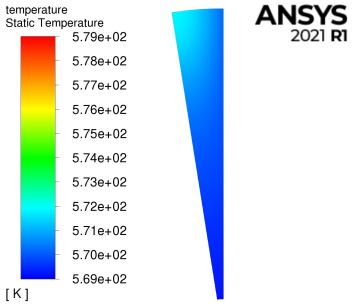

(h) t = 60 min.

Figure 4.23: Temperature contours for the trapezoidal fin profile geometry at 5 min, 10 min, 15 min, 20 min, 30 min, 40 min, 50 min and 60 min.

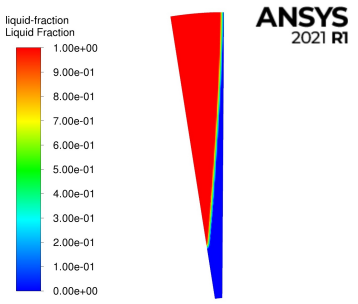

(a) t = 5 min, LF = 75.00%.

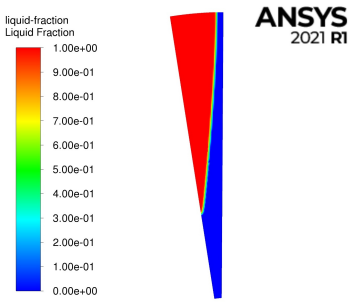

(b) t = 10 min, LF = 59.41%.

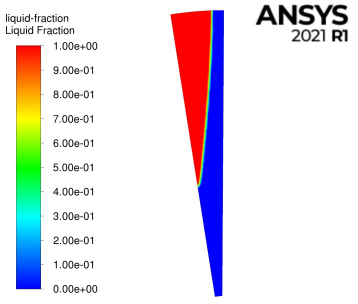

(c) t = 15 min, LF = 47.09%.

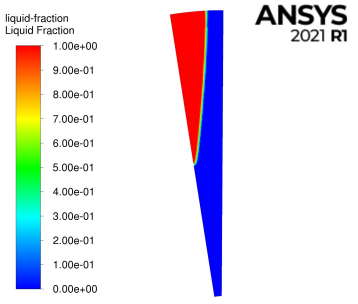

(d) t = 20 min, LF = 36.94%.

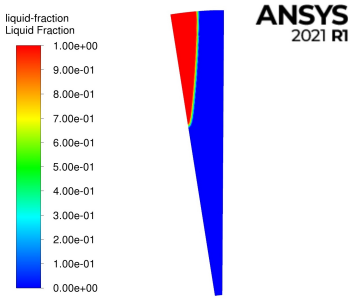

(e) t = 30 min, LF = 21.26%.

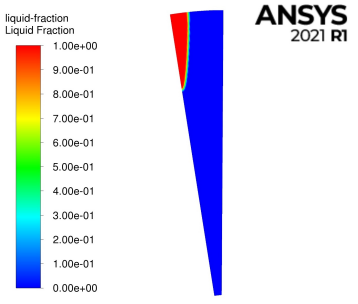

(f) t = 40 min, LF = 10.24%.

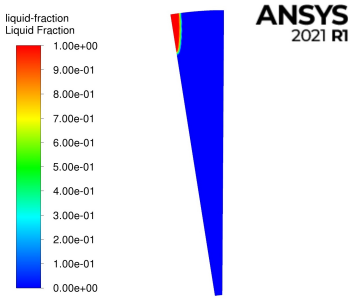

(g) t = 50 min, LF = 3.01%.

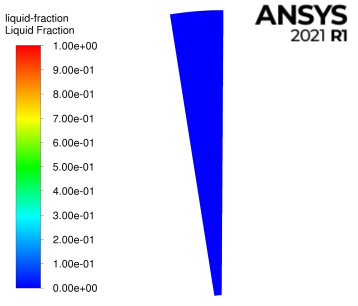

(h) t = 60 min, LF = 0%.

Figure 4.24: Liquid fraction contours for the trapezoidal fin profile geometry at 5 min, 10 min, 15 min, 20 min, 30 min, 40 min, 50 min and 60 min.

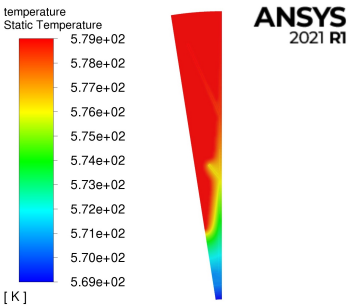

(a) t = 5 min.

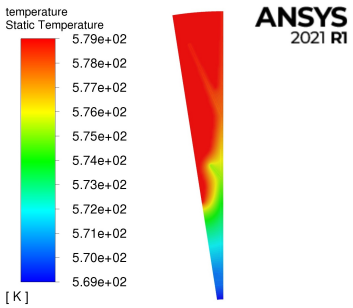

(b) t = 10 min.

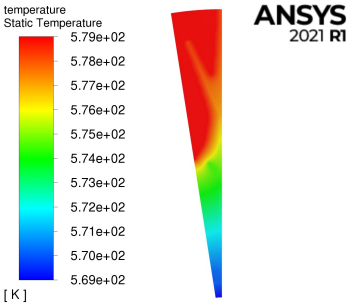

(c) t = 15 min.

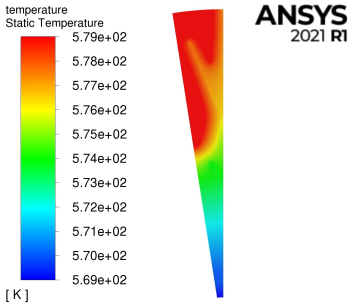

(d) t = 20 min.

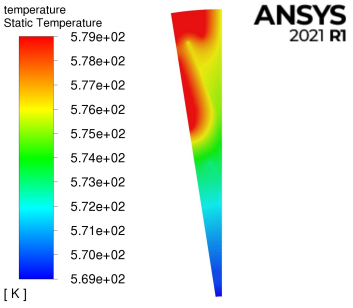

(e) t = 30 min.

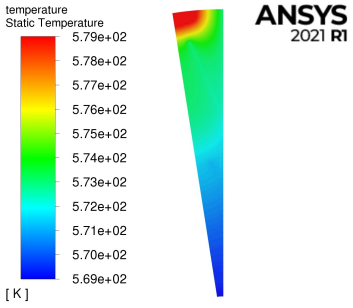

(f) t = 40 min.

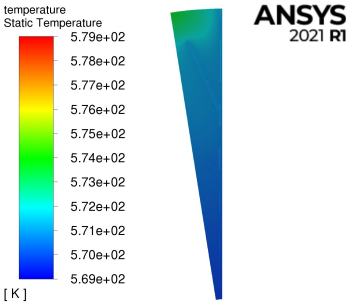

(g) t = 50 min.

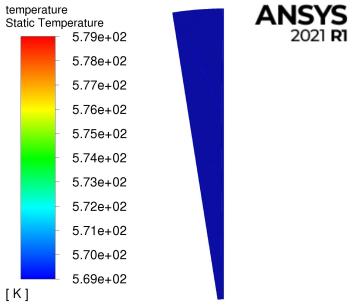

(h) t = 60 min.

Figure 4.25: Temperature contours for the fractal fin profile geometry at 5 min, 10 min, 15 min, 20 min, 30 min, 40 min, 50 min and 60 min.

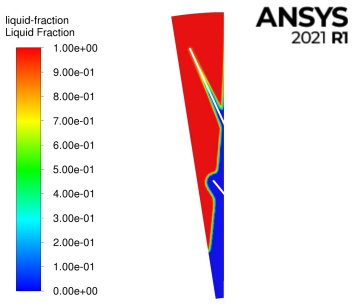

(a) t = 5 min, LF = 75.94%.

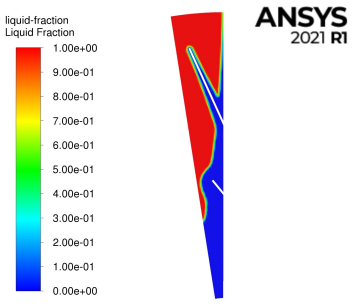

(b) t = 10 min, LF = 60.09%.

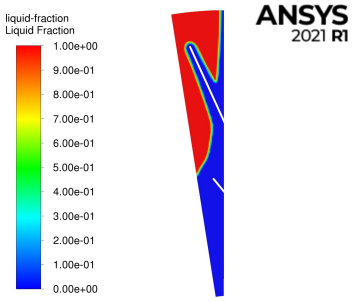

(c) t = 15 min, LF = 46.90%.

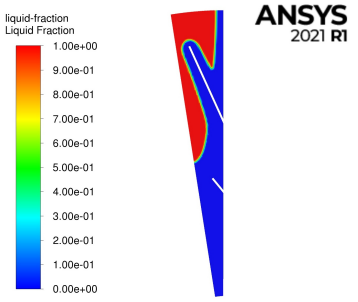

(d) t = 20 min, LF = 35.51%.

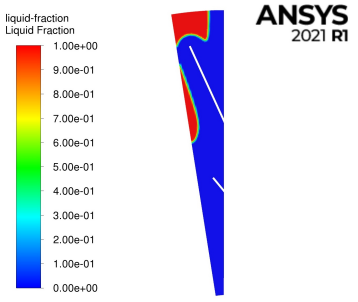

(e) t = 30 min, LF = 16.21%.

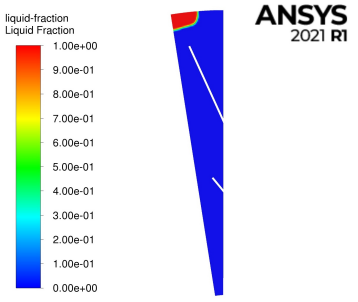

(f) t = 40 min, LF = 4.18%.

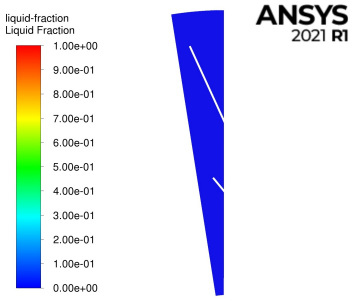

(g) t = 50 min, LF = 0%.

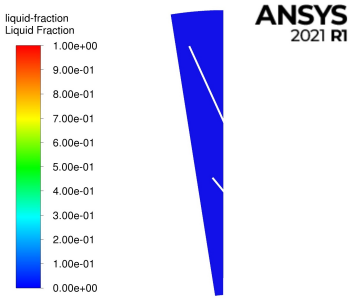

(h) t = 60 min, LF = 0%.

Figure 4.26: Liquid fraction contours for the fractal fin profile geometry at 5 min, 10 min, 15 min, 20 min, 30 min, 40 min, 50 min and 60 min.

Temperature contours for the three configurations at the end of the simulation time (t = 80 min) are reported in Fig. 4.27. They show that all the energy is released because the temperature field equals the imposed temperature throughout the domain. It can also be seen through the discharging power graph over time, reported in Fig. 4.28, as the power is equal to zero at t = 80 min.

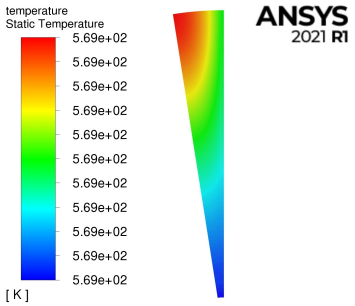

(a) Fin with a rectangular profile.

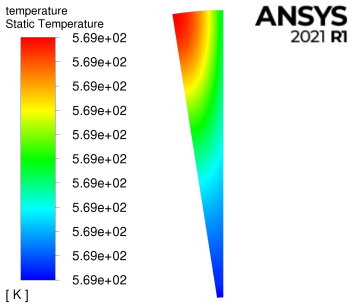

(b) Fin with a trapezoidal profile.

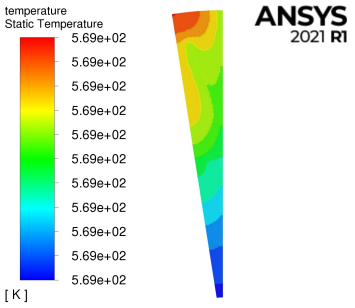

(c) Fin with a fractal profile.

Figure 4.27: Temperature contours for the three configurations at the end of simulation time (t = 80 min).

Discharging power graph (Fig. 4.28) has been calculated from the total heat flux [W/m^2] at the inner radius of the steel tube for 1 m length TES system. To perform the comparison between curves, the point where the liquid fraction equals a reference value (10%) is also represented in the graph, showing a faster discharging speed for the fractal geometry.

Fig. 4.29 shows the discharging power curve over the State of Charge of the thermal battery that varies from 100% (system completely charged, all PCM liquid) to 0% (system completely discharged, all PCM solid). If t_0 is the initial time and t^* is the time corresponding to the end of the simulation,

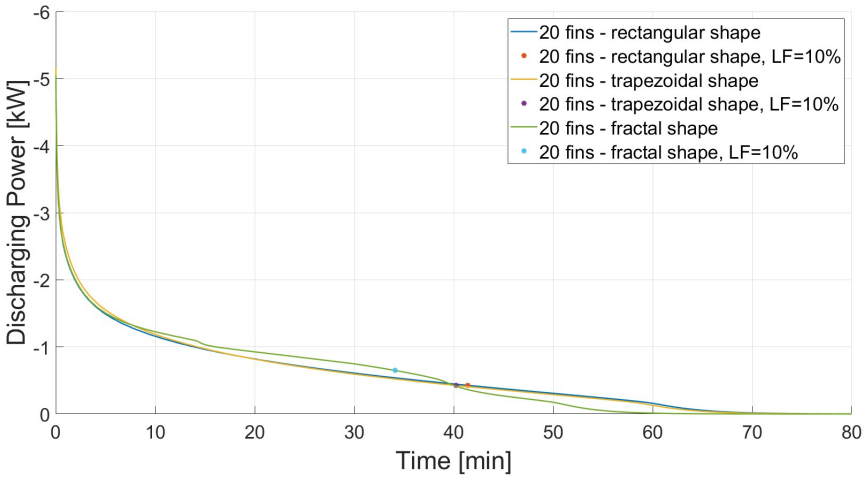

Figure 4.28: Total discharging power over time for the three configurations under study.

the State of Charge is calculated as:

$$SoC = \frac{E(t) - E(t^*)}{E(t_0) - E(t^*)}$$

where $E(t) - E(t^*)$ represents the PCM accumulated energy at time t and $E(t_0) - E(t^*)$ the total PCM released energy until complete solidification. The energy, calculated by Ansys Fluent according to the equation 4.19, is here the average energy calculated over the PCM area at time t, t^* and t_0.

The reference value of 10% liquid fraction, above mentioned, is also used to calculate the average discharging power as:

$$P_{ave} = \frac{1}{t_n - t_0} \sum_{i=0}^{n} (P_i - P_{i-1})(t_i - t_{i-1})$$

where:

- t_n is the time corresponding to LF = 10%;
- t_0 is the initial time;
- $i = 0, 1, ...n$ is the time discretization index;
- P_i is the discharging power corresponding to the i-th time step;
- t_i is the time corresponding to the i-th time step.

The average discharging power P_{ave} for the three configurations is reported in Tab. 4.7, together with the total energy released during the discharging process up to the end of the simulation. The total energy has

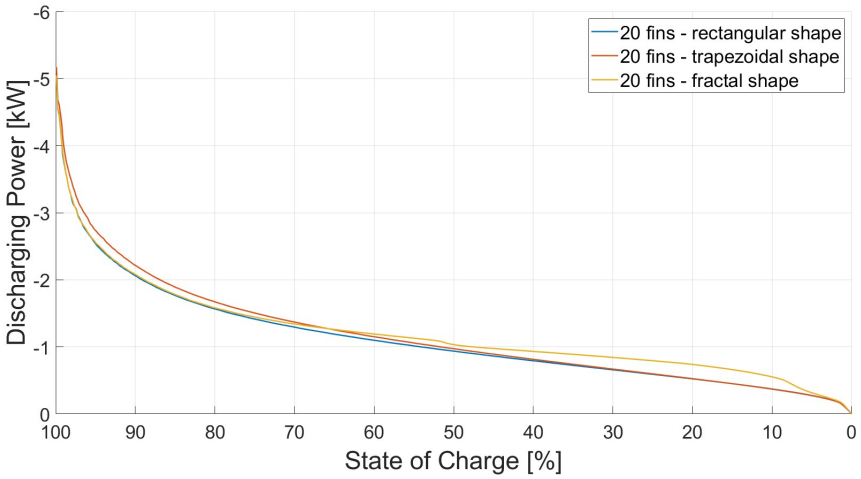

Figure 4.29: Total discharging power over the State of Charge for the three configurations under study.

been calculated:

- theoretically as
$$E_{LH} = M_{PCM} \cdot L$$
where M_{PCM} [kg] is the PCM total mass of 1 m length TES system and L [J/kg] is the PCM latent heat;

- from the discharging power curve (at the inner radius of the steel tube) as
$$E_P = \sum_{i=0}^{n^*} (P_i - P_{i-1})(t_i - t_{i-1})$$
where n^* is the time corresponding to the end of the simulation, $i = 0, 1, ...n^*$ is the time discretization index, P_i is the discharging power corresponding to the i-th time step and t_i is the time corresponding to the time step.

E_{LH} represents the storage capacity of the thermal battery as it is calculated from the PCM mass and latent heat of the TES system (for this reason, it is a positive value). It is constant for all the configurations (Tab. 4.7) as they are created keeping constant the PCM volume fraction.

E_P is a negative value as it represents the total energy released during the discharging process. It slightly changes for the three configurations due to the different domain discretization and its absolute value is higher than E_{LH} because of the energy contributions of aluminum and steel materials.

Table 4.7: Average discharging power P_{ave} (for a time corresponding to LF = 10%), total energy from latent heat formula E_{LH} (at the end of simulation time) and total energy calculated from power E_P (at the end of simulation time) for the three configurations under study.

	Total time	Rectangular fins	Trapezoidal fins	Fractal fins
P_{ave}	t : LF = 10%	-950.8 W	-979.4 W	-1136.6 W
E_{LH}	80 min	$2.6877 \cdot 10^6$ J	$2.6877 \cdot 10^6$ J	$2.6877 \cdot 10^6$ J
E_P	80 min	$-2.7380 \cdot 10^6$ J	$-2.7379 \cdot 10^6$ J	$-2.7326 \cdot 10^6$ J

Chapter 5

Conclusion and future developments

In this thesis, two alternatives for long-term energy storage have been investigated. The first one is hydrogen and its technologies.

The thesis proposed a new model to describe the behavior of a PEM fuel cell for a set of currents by means of a single Fractional-Order Transfer Function. The proposed model exploited only five parameters; two are fixed, while the others can be mathematically computed as a current function. The FOTF was identified using a set of EIS experimental measurements taken at the laboratories of CNR-ITAE on a $25\,\mathrm{cm}^2$ active area PEMFC. Genetic algorithms were used to identify the FOTF parameters for each working point. As a second step, an approximated model was investigated. To this aim, two of the five parameters were fixed and an interpolation function was designed for the remaining three parameters as a function of the current value. The quality of the approximation was evaluated both against the experimental measurements and the simulations of a model reported in the literature.

Further research will be devoted to finding an Equivalent Electric Circuit Model based on the proposed FOTF. Also, new instrumentation will be used to measure currents higher than 20 A, extending the validity range of the proposed approach.

As second step, an LSTM-based degradation curve estimation for a FC was proposed. The network was trained on a dataset obtained by simulation a degradation protocol over time to a cell, starting from a set of experimental measurements. Estimating the degradation curve allowed the evaluation of the health status of the cell as a function of the cycles.

Future developments will require the experimental validation of the degradation protocol for the fuel cell to obtain a full experimental dataset.

The second part of the thesis concerned the Electrochemical Hydrogen Compressor. Its polarization curve was analyzed, mainly focusing on the correlation between the current density and the voltage when the compression ratio varies. Results showed that the slope of the line decreases as the compression ratio increases, meaning that more energy is needed for the compression process.

Future work will concern a more detailed characterization of the compression ratio, equipping the laboratory to achieve higher cathodic pressures. Furthermore, it is necessary to study the effect of temperature and relative humidity on the performance of the EHC to determine its optimal operating condition for more efficient compression.

Furthermore, a time-test measurement was performed on the Electrochemical Compressor. Unlike what was expected from mathematical equations, spiking behavior emerged and was completely unexpected. Then, a possible chaotic behavior was considered. From the analysis, the system was highly sensitive to the initial conditions and presented a density of periodic orbits, which were shown in the reconstructed phase plane through the time delay embedding technique. Hence it is conceivable that the system is chaotic.

The analysis, especially the chaotic ones, was the first approach to an unknown and non-predictable phenomenon. Therefore, the obtained results must be confirmed through more detailed analysis, in particular measuring the voltage at a fixed current and extending the time windows.

Finally, the monopolar plate of an Electrochemical Hydrogen Compressor was analyzed from a structural point of view. Small-sized channels and holes behave as notches, significantly increasing the stress triaxiality at the local scale. High-stress triaxiality peaks, eventually combined with hydrogen embrittlement, can significantly increase the probability of failure and crack initiation at a given material point. Based on such considerations, the Electrochemical Hydrogen Compressor End-Plate must be designed in order to have conservative levels of the nominal stress states. The research aimed to find the optimal shape of the monopolar plate, starting from three different geometric configurations. The results of the FEM analysis with Marc software - of MSC Software Corporation - identified the optimal configuration in circular plan view and active area. The plate in this configuration has been sized to have a deflection no greater than 0.1 mm when the EHC works at its operational pressure (700 bar). The minimum plate thickness is 17 mm. The deflection can increase up to 3.13% since the upper surface of the plate has been constrained by infinitely rigid washers rather than the deformable surface of the other monopolar plate.

Future developments foresee realizing more accurate FEM simulations both on the monopolar plate and on the bipolar plate, involving new aspects, such as implicit elastoplastic simulations or damage both on a global scale (loads acting on the system are not the operating ones but the exceptional ones) and on a local scale (plasticization occurs even with standard loads, where the cracks appear).

The second solution for long-term energy storage is a Thermal Energy Storage System. In particular, the thesis investigated the latent heat alternative among TES solutions. The mathematical modeling of a melting and solidification process has time-dependent boundary conditions because the interface between solid and liquid phases is a moving boundary. The heat transfer analysis needs to know the interface position over time to predict the temperature inside the liquid and the solid regions.

The Classical Stefan Problem was considered in the one-dimensional case in order to implement its analytical model in Matlab. The transcendental equation was solved by the Newton-Raphson iterative method and the results were compared with an example from the literature. The same boundary and initial conditions were utilized for the numerical simulation on ANSYS FLUENT 2021 R1, then the comparison of results obtained from the Matlab analytical model and Ansys Fluent numerical simulation was carried on. The maximum computational error was less than 2.6%.

The validation of the results allowed us to be confident about the correctness of the numerical model settings, so the same settings were used for studying a more interesting problem, i.e., evaluating the performance of three different latent heat TES configurations during a discharging process. The goal was to find the most efficient latent heat TES configuration in terms of maximum average discharging power. Geometries were sized changing only the fin shape (rectangular, trapezoidal and fractal), keeping constant the volume fractions of steel, aluminum and PCM for all the configurations in order to perform a proper comparison. Results showed that the trapezoidal fin profile performs better than the rectangular one. The fractal fin profile geometry seemed worse than the others at the beginning of the discharging process due to the different distribution of the aluminum material between configurations. Instead, it definitively revealed the best at the end, as the branches are responsible for faster thermal exchange when the solidifying frontier moves away from the steel ring. The PCM was completely discharged after 50 minutes (PCM in rectangular fin profile geometry after 59 minutes and in the trapezoidal fin profile geometry after 58 minutes). This behavior was also shown from the discharging power graph over time and over the State of Charge. In conclusion, the average discharging power for the three configurations was evaluated,

showing the higher performance obtained with the fractal fin profile.

The numerical model is suitable for simulating PCM with conductive additives, requiring only changing the thermophysical properties of the material. Future developments foresee other simulations with such phase change materials or with the same PCM used in this thesis but utilizing the thermophysical properties obtained from experimental measurements. The following step will be the experimental validation of the same physical models numerically studied in this thesis.

Bibliography

[1] https://unfccc.int/documents/279247. [Online]. 2022.

[2] Dolf Gielen et al. "The role of renewable energy in the global energy transformation". In: *Energy Strategy Reviews* 24 (2019), pp. 38–50. ISSN: 2211-467X.

[3] Morten B. Ley et al. "Complex hydrides for hydrogen storage – new perspectives". In: *Materials Today* 17.3 (2014), pp. 122–128. ISSN: 1369-7021. DOI: https://doi.org/10.1016/j.mattod.2014.02.013.

[4] David J.C. Mackay. *Sustainable Energy - Without the Hot Air*. Uit Cambridge Ltd, 2009.

[5] James A Ritter et al. "Implementing a hydrogen economy". In: *Materials Today* 6.9 (2003), pp. 18–23. ISSN: 1369-7021. DOI: https://doi.org/10.1016/S1369-7021(03)00921-0.

[6] Andreas Züttel. "Materials for hydrogen storage". In: *Materials Today* 6.9 (2003), pp. 24–33. ISSN: 1369-7021. DOI: https://doi.org/10.1016/S1369-7021(03)00922-2.

[7] Jidai Wang et al. "Overview of Compressed Air Energy Storage and Technology Development". In: *Energies* 10.7 (2017). ISSN: 1996-1073. DOI: 10.3390/en10070991.

[8] Samir Succar, Robert H Williams, et al. "Compressed air energy storage: theory, resources, and applications for wind power". In: *Princeton environmental institute report* 8 (2008), p. 81.

[9] Andrew Blakers et al. "A review of pumped hydro energy storage". In: *Progress in Energy* 3.2 (Mar. 2021), p. 022003. DOI: 10.1088/2516-1083/abeb5b.

[10] Felipe Trebilcock et al. "Development of a Compressed Heat Energy Storage System Prototype". In: July 2020. DOI: 10.18462/iir.rankine.2020.1178.

[11] Saba Niaz, Taniya Manzoor, and Altaf Hussain Pandith. *Hydrogen storage: Materials, methods and perspectives*. 2015. DOI: 10.1016/j.rser.2015.05.011.

[12] D.J. Durbin and C. Malardier-Jugroot. "Review of hydrogen storage techniques for on board vehicle applications". In: *International Journal of Hydrogen Energy* 38 (2013), pp. 14595–14617. ISSN: 0360-3199.

[13] C. Casati et al. "Some fundamental aspects in electrochemical hydrogen purification/compression". In: *Journal of Power Sources* 180 (2008), pp. 103–113. ISSN: 0378-7753.

[14] A.M. Seayad and D.M. Antonelli. "Recent Advanced in Hydrogen Storage in Metal-Containing Inorganic Nanostructures and Related Materials". In: *Advanced Materials* 16 (2004), pp. 765–777. ISSN: 1521-4095.

[15] H. Barthelemy, M. Weber, and F. Barbier. "Hydrogen storage: Recent improvements and industrial perspectives". In: *International Journal of Hydrogen Energy* 42 (2017), pp. 7254–7262. ISSN: 0360-3199.

[16] N.A.A. Rusman and M. Dahari. "A review on the current progress of metal hydrides material for solid-state hydrogen storage applications". In: *International Journal of Hydrogen Energy* 41 (2016), pp. 12108–12126. ISSN: 0360-3199.

[17] Michael U. Niemann et al. "Nanomaterials for Hydrogen Storage Applications: A Review". In: *Journal of Nanomaterials* 2008 (2008).

[18] T.Q. Hua et al. "Technical assessment of compressed hydrogen storage tank systems for automotive applications". In: *International Journal of Hydrogen Energy* 36 (2011), pp. 3037–3049. ISSN: 0360-3199.

[19] R.K. Ahluwalia, T.Q. Hua, and J.K. Peng. "On-board and Off-board performance of hydrogen storage options for light-duty vehicles". In: *International Journal of Hydrogen Energy* 37 (2012), pp. 2891–2910. ISSN: 0360-3199.

[20] P. Bouwman. "Electrochemical Hydrogen Compression (EHC) solutions for hydrogen infrastructure". In: *Fuel Cells Bulletin* 2014 (2014), pp. 12–16. ISSN: 1464-2859.

[21] N. Miguel et al. "Compressed hydrogen tanks for on-board application: Thermal behaviour during cycling". In: *International Journal of Hydrogen Energy* 33 (2015), pp. 6449–6458. ISSN: 0360-3199.

[22] Michel Suermann et al. "Electrochemical Hydrogen Compression: Efficient Pressurization Concept Derived from an Energetic Evaluation". In: *Journal of The Electrochemical Society* 164.12 (2017), F1187–F1195.

[23] Brian M. Besancon et al. "Hydrogen quality from decarbonized fossil fuels to fuel cells". In: *International Journal of Hydrogen Energy* 34.5 (2009), pp. 2350–2360. ISSN: 0360-3199.

[24] R. Strobel et al. "The compression of hydrogen in an electrochemical cell based on a PE Fuel Cell design". In: *Journal of Power Sources* 105 (2002), pp. 208–215. ISSN: 0378-7753.

[25] Jiexin Zou et al. "Electrochemical Compression Technologies for High-Pressure Hydrogen: Current Status, Challenges and Perspective". In: *Electrochemical Energy Reviews* 3 (2020), pp. 690–729.

[26] F. Matera et al. "Performance assessment of alternative membranes for Electrochemical Hydrogen Compressor (EHC) in portable PEM fuel cell applications". In: *European Hydrogen Energy Conference - Spain* (2018).

[27] B. Rohland et al. "Electrochemical hydrogen compressor". In: *Electrochimica Acta* 43 (1998), pp. 3841–3846. ISSN: 0013-4686.

[28] Ahmed Elberry et al. "Large-scale compressed hydrogen storage as part of renewable electricity storage systems". In: *International Journal of Hydrogen Energy* 46 (Mar. 2021). DOI: 10.1016/j.ijhydene.2021.02.080.

[29] https://www.irena.org/publications/2020/Nov/Innovation-outlook-Thermal-energy-storage. [Online]. 2022.

[30] https://www.solarthermalworld.org/sites/default/files/brewing_beer_with_solar_heat.pdf. [Online]. 2022.

[31] Iñigo Ortega-Fernández and Javier Rodríguez-Aseguinolaza. "Thermal energy storage for waste heat recovery in the steelworks: The case study of the REslag project". In: *Applied Energy* 237 (2019), pp. 708–719. ISSN: 0306-2619. DOI: https://doi.org/10.1016/j.apenergy.2019.01.007.

[32] https://cordis.europa.eu/project/id/642067. [Online]. 2022.

[33] http://large.stanford.edu/publications/power/references/docs/Andasol1-3engl.pdf. [Online]. 2022.

[34] https://www.kyotogroup.no/news/kyoto-group-orders-first-thermal-battery-for-commercial-pilot-decarbonizing-industrial-heat-usage. [Online]. 2022.

[35] https://www.igte.uni-stuttgart.de/en/research/research_hrt/completed-projects/desinadine/. [Online]. 2022.

[36] https://www.eec.org.au/for-energy-users/technologies-2/heat-pumps. [Online]. 2022.

[37] https://www.nrcan.gc.ca/energy-efficiency/energy-star-canada/about/energy-star-announcements/publications/heating-and-cooling-heat-pump/6817. [Online]. 2022.

[38] Wolf-Dieter Steinmann, Henning Jockenhöfer, and Dan Bauer. "Thermodynamic Analysis of High-Temperature Carnot Battery Concepts". In: *Energy Technology* 8.3 (2020), p. 1900895. DOI: https://doi.org/10.1002/ente.201900895.

[39] Riccardo Caponetto et al. "Fuel Cell Fractional-Order Model via Electrochemical Impedance Spectroscopy". In: *Fractal and Fractional* 5.1 (2021). ISSN: 2504-3110. DOI: 10.3390/fractalfract5010021.

[40] Riccardo Caponetto et al. "Application of Electrochemical Impedance Spectroscopy for prediction of Fuel Cell degradation by LSTM neural networks". In: *2021 29th Mediterranean Conference on Control and Automation (MED)*. 2021, pp. 1064–1069. DOI: 10.1109/MED51440.2021.9480253.

[41] S. A. Sherif, F. Barbir, and T. N. Veziroglu. "Wind energy and the hydrogen economy-review of the technology". In: *Solar Energy* (2005). ISSN: 0038092X. DOI: 10.1016/j.solener.2005.01.002.

[42] John O.m. Bockris and T. Nejat Veziroglu. "A Solar-Hydrogen Energy System for Environmental Compatibility". In: *Environmental Conservation* (1985). ISSN: 14694387. DOI: 10.1017/S0376892900015526.

[43] Fabio Matera. *Membrane Electrochemical Hydrogen Compressor (EHC) for PEFC: technical aspects, challenges and research at CNR-ITAE*. Tech. rep. 2017.

[44] Michael A. Danzer and Eberhard P. Hofer. "Analysis of the electrochemical behaviour of polymer electrolyte fuel cells using simple impedance models". In: *Journal of Power Sources* (2009). ISSN: 03787753. DOI: 10.1016/j.jpowsour.2008.10.003.

[45] Matteo Galeotti et al. "Performance analysis and SOH (state of health) evaluation of lithium polymer batteries through electrochemical impedance spectroscopy". In: *Energy* (2015). ISSN: 03605442. DOI: 10.1016/j.energy.2015.05.148.

[46] Hong Sun et al. "Characteristics of charge/discharge and alternating current impedance in all-vanadium redox flow batteries". In: *Energy* (2019). ISSN: 03605442. DOI: 10.1016/j.energy.2018.11.130.

[47] A. Buscarino et al. "Preliminary analysis of the chaotic behavior in hydrogen electrochemical devices". In: *IFAC-PapersOnLine* 54.17 (2021). 6th IFAC Conference on Analysis and Control of Chaotic Systems CHAOS 2021, pp. 149–153. ISSN: 2405-8963. DOI: https://doi.org/10.1016/j.ifacol.2021.11.041.

[48] F. Barbir. *PEM Fuel Cells: Theory and Practice*. Academic Press sustainable world series PEM fuel cells. Elsevier Science, 2005. ISBN: 9780080455419.

[49] "Polarization curve". In: *https://www.fuelcellstore.com/blog-section/polarization-curves* ().

[50] Liga, R. "Caratterizzazione e modellistica di uno stack di celle a membrana polimerica (PEM) per sistemi di propulsione per automotive". PhD thesis. 2013.

[51] Michael Danzer and Eberhard Hofer. "Analysis of the electrochemical behaviour of polymer electrolyte fuel cells using simple impedance models". In: *Journal of Power Sources - J POWER SOURCES* 190 (May 2009), pp. 25–33. DOI: 10.1016/j.jpowsour.2008.10.003.

[52] Hong Sun et al. "Characteristics of Charge/Discharge and Alternating Current Impedance in All-Vanadium Redox Flow Batteries". In: *Energy* 168 (Nov. 2018). DOI: 10.1016/j.energy.2018.11.130.

[53] Mohamed Sélmene Ben Yahia et al. "Fuel cell impedance model parameters optimization using a genetic algorithm". In: *International Journal of Electrical and Computer Engineering* (2017). ISSN: 20888708. DOI: 10.11591/ijece.v7i1.pp196-205.

[54] NETL. "Seventh Edition Fuel Cell Handbook". In: (Nov. 2004). DOI: 10.2172/834188. URL: https://www.osti.gov/biblio/834188.

[55] https://www.seastema.it/Comunicato%20stampa%20TETI_eng.pdf. [Online]. 2022.

[56] Aparna M. Dhirde et al. "Equivalent electric circuit modeling and performance analysis of a PEM fuel cell stack using impedance spectroscopy". In: *IEEE Transactions on Energy Conversion* (2010). ISSN: 08858969. DOI: 10.1109/TEC.2010.2049267.

[57] Huaxin Lu et al. "On-line fault diagnosis for proton exchange membrane fuel cells based on a fast electrochemical impedance spectroscopy measurement". In: *Journal of Power Sources* 430 (2019), pp. 233–243. ISSN: 0378-7753. DOI: https://doi.org/10.1016/j.jpowsour.2019.05.028.

[58] Mohammad Zhiani et al. "Comparison of the performance and EIS (electrochemical impedance spectroscopy) response of an activated PEMFC (proton exchange membrane fuel cell) under low and high thermal and pressure stresses". In: *Energy* 97 (2016), pp. 560–567.

[59] Parthasarathy M. Gomadam and John W. Weidner. *Analysis of electrochemical impedance spectroscopy in proton exchange membrane fuel cells*. 2005. DOI: 10.1002/er.1144.

[60] Junxiang Shi and Xingjian Xue. "Mechanistic model based multi-impedance curve-fitting approach for solid oxide fuel cells". In: *Journal of Electroanalytical Chemistry* (2011). ISSN: 15726657. DOI: 10.1016/j.jelechem.2011.07.034.

[61] R. Pan et al. "Health degradation assessment of proton exchange membrane fuel cell based on an analytical equivalent circuit model". In: *Energy* 207 (2020).

[62] K. B. Oldham and J. Spanier. *The Fractional Calculus: Theory and Applications of Differentiation and Integration to Arbitrary Order*. Elsevier, 2006.

[63] A. Atangana and D. Baleanu. "New Fractional Derivatives with Nonlocal and Non-Singular Kernel: Theory and Application to Heat Transfer Model". In: *Therm Sci* 20 (2016), pp. 763–769.

[64] M. Caputo and M. Fabrizio. "New Fractional Derivatives with Nonlocal and Non-Singular Kernel: Theory and Application to Heat Transfer Model". In: *Prog Fract Differ Appl* 1.2 (2015), pp. 73–85.

[65] J. Sabatier, C. Farges, and J.C. Trigeassou. "Fractional systems state space description: some wrong ideas and proposed solutions". In: *Journal of Vibration and Control* 20.7 (2014), pp. 1076–1084.

[66] H. Sun et al. "A new collection of real world applications of fractional calculus in science and engineering". In: *Communication in Nonlinear Science and Numerical Simulation* 64 (2018), pp. 213–231.

[67] R. Caponetto et al. "Model Order Reduction: A Comparison between Integer and Non-Integer Order Systems Approaches". In: *Entropy* 21.9 (2019).

[68] A. Ardjal et al. "Design and implementation of a fractional nonlinear synergetic controller for generator and grid converters of wind energy conversion system". In: *Energy* 186 (2019).

[69] V. Tarasov and V. Tarasova. "Criterion of Existence of Power-Law Memory for Economic Processes". In: *Entropy* 20.6 (2018).

[70] R. Caponetto et al. "Realization of green fractional order devices by using bacterial cellulose". In: *AEU – Int. J. of Elec. and Comm.* 112.1 (2019), pp. 246–254.

[71] C. Vastarouchas et al. "Emulation of an electrical-analogue of a fractional order human respiratory mechanical impedance model using OTA topologies". In: *AEU - International Journal of Electronics and Communications* 78 (2017), pp. 201–208.

[72] J. Sabatier. "Fractional Order Models for Electrochemical Devices". In: *Fractional Dynamics*. Ed. by C. Cattani, H. M. Srivastava, and X. J. Yang. De Gruyter, 2015. Chap. 9, pp. 141–160.

[73] Q. Zhu et al. "A state of charge estimation method for lithium-ion batteries based on fractional order adaptive extended kalman filter". In: *Energy* 187 (2019).

[74] Jay B. Benziger et al. "The power performance curve for engineering analysis of fuel cells". In: *Journal of Power Sources* 155 (2006), pp. 272–285.

[75] A. J. Bard and L. R. Faulkner. *Electrochemical Methods: Fundamentals and Applications*. 2nd ed. Wiley, 2000. Chap. 10.

[76] D. Goldberg. *Genetic Algorithms in Search, Optimization, and Machine Learning*. Addison-Wesley Professional, 1989.

[77] A. J. Chipperfield, P. J. Fleming, and C. M. Fonseca. "Genetic Algorithm Tools for Control Systems Engineering". In: *Proc. Adaptive Computing in Engineering Design and Control* (1994), pp. 128–123.

[78] Thyago P. Carvalho et al. "A systematic literature review of machine learning methods applied to predictive maintenance". In: *Computers & Industrial Engineering* 137 (2019), p. 106024. ISSN: 0360-8352. DOI: https://doi.org/10.1016/j.cie.2019.106024.

[79] M. G. Xibilia et al. "Soft Sensors Based on Deep Neural Networks for Applications in Security and Safety". In: *IEEE Transactions on Instrumentation and Measurement* 69.10 (2020), pp. 7869–7876. DOI: 10.1109/TIM.2020.2984465.

[80] Salvatore Graziani and Maria Gabriella Xibilia. "Deep Learning for Soft Sensor Design". In: *Development and Analysis of Deep Learning Architectures*. Ed. by Witold Pedrycz and Shyi-Ming Chen. Vol. 867. Studies in Computational Intelligence. Springer, 2020, pp. 31–59.

[81] D. Zhang, X. Han, and C. Deng. "Review on the research and practice of deep learning and reinforcement learning in smart grids". In: *CSEE Journal of Power and Energy Systems* 4.3 (2018), pp. 362–370. DOI: 10.17775/CSEEJPES.2018.00520.

[82] Georg Helbing and Matthias Ritter. "Deep Learning for fault detection in wind turbines". In: *Renewable and Sustainable Energy Reviews* 98 (2018), pp. 189–198. ISSN: 1364-0321. DOI: https://doi.org/10.1016/j.rser.2018.09.012.

[83] Yang Zhao et al. "A review of data mining technologies in building energy systems: Load prediction, pattern identification, fault detection and diagnosis". In: *Energy and Built Environment* 1.2 (2020), pp. 149–164. ISSN: 2666-1233. DOI: https://doi.org/10.1016/j.enbenv.2019.11.003.

[84] Samuel Simon Araya et al. "Fault Characterization of a Proton Exchange Membrane Fuel Cell Stack". In: *Energies* 12 (Jan. 2019), p. 152. DOI: 10.3390/en12010152.

[85] Christophe Lin-Kwong-Chon et al. "A review of adaptive neural control applied to proton exchange membrane fuel cell systems". In: *Annual Reviews in Control* 47 (2019), pp. 133–154. ISSN: 1367-5788. DOI: https://doi.org/10.1016/j.arcontrol.2019.03.009.

[86] Karim Belmokhtar, Mamadou Doumbia, and K. Agboussou. "PEM fuel cell modelling using artificial neural networks (ANN)". In: *International Journal of Renewable Energy Research* 4 (Jan. 2014), pp. 725–730.

[87] Christian Jeppesen et al. "Fault detection and isolation of high temperature proton exchange membrane fuel cell stack under the influence of degradation". In: *Journal of Power Sources* 359 (2017), pp. 37–47. ISSN: 0378-7753. DOI: https://doi.org/10.1016/j.jpowsour.2017.05.021.

[88] Rui Ma et al. "Data-driven proton exchange membrane fuel cell degradation predication through deep learning method". In: *Applied Energy* 231 (2018), pp. 102–115. ISSN: 0306-2619. DOI: https://doi.org/10.1016/j.apenergy.2018.09.111.

[89] R. Ma et al. "Data-Fusion Prognostics of Proton Exchange Membrane Fuel Cell Degradation". In: *IEEE Transactions on Industry Applications* 55.4 (2019), pp. 4321–4331. DOI: 10.1109/TIA.2019.2911846.

[90] Dongho Seo et al. "Investigation of MEA degradation in PEM fuel cell by on/off cyclic operation under different humid conditions". In: *International Journal of Hydrogen Energy* 36.2 (2011). The 3rd Annual Korea-USA Joint Symposium on Hydrogen & Fuel Cell Technologies, pp. 1828–1836. ISSN: 0360-3199. DOI: https://doi.org/10.1016/j.ijhydene.2010.02.053.

[91] Weiqi Zhang et al. "Anode and cathode degradation in a PEFC single cell investigated by electrochemical impedance spectroscopy". English. In: *Electrochimica Acta* 131.Complete (2014), pp. 245–249. DOI: 10.1016/j.electacta.2014.02.054.

[92] N Wagner and Erich Gülzow. "Change of electrochemical impedance spectra (EIS) with time during CO-poisoning of the Pt-anode in a membrane fuel cell". In: *Journal of Power Sources* 127 (Mar. 2004), pp. 341–347. DOI: 10.1016/j.jpowsour.2003.09.031.

[93] Ivan Pivac, Dario Bezmalinović, and Frano Barbir. "Catalyst degradation diagnostics of proton exchange membrane fuel cells using electrochemical impedance spectroscopy". In: *International Journal of Hydrogen Energy* 43 (June 2018). DOI: 10.1016/j.ijhydene.2018.05.095.

[94] Sepp Hochreiter and Jürgen Schmidhuber. "LSTM can solve hard long time lag problems". In: Jan. 1996, pp. 473–479.

[95] D. Bruneo and F. De Vita. "On the Use of LSTM Networks for Predictive Maintenance in Smart Industries". In: *2019 IEEE International Conference on Smart Computing (SMARTCOMP)*. 2019, pp. 241–248. DOI: 10.1109/SMARTCOMP.2019.00059.

[96] Riccardo Caponetto et al. "Structural Analysis of Electrochemical Hydrogen Compressor End-Plates for High-Pressure Applications". In: *Energies* 15.16 (2022). ISSN: 1996-1073. DOI: 10.3390/en15165823. URL: https://www.mdpi.com/1996-1073/15/16/5823.

[97] [Florence Druart et al. "Electrochemical hydrogen compression and purification versus competing technologies: Part I. Pros and cons". In: *Chinese Journal of Catalysis* 41.5, 756 (2020), pp. 756–769.

[98] Ashish Chouhan, Bamdad Bahar, and Ajay K. Prasad. "Effect of back-diffusion on the performance of an electrochemical hydrogen compressor". In: *International Journal of Hydrogen Energy* 45.19 (2020), pp. 10991–10999. ISSN: 0360-3199.

[99] P. Bouwman. "Electrochemical Hydrogen Compression (EHC) solutions for hydrogen infrastructure". In: *Fuel Cells Bulletin* 2014 (2014), pp. 12–16. ISSN: 1464-2859.

[100] Yasemin Aykut and Ayşe Bayrakçeken Yurtcan. "Catalyst development for viability of electrochemical hydrogen purifier and compressor (EHPC) technology". In: *International Journal of Hydrogen Energy* (2022). ISSN: 0360-3199.

[101] E.A. Fosson. *Design and analysis of a hydrogen compression and storage station.* 2017. URL: https://calhoun.nps.edu/handle/10945/56919.

[102] Jiexin Zou et al. "Insights into electrochemical hydrogen compressor operating parameters and membrane electrode assembly degradation mechanisms". In: *Journal of Power Sources* 484 (2021), p. 229249. ISSN: 0378-7753.

[103] S. Toghyani, E. Baniasadi, and E. Afshari. "Performance analysis and comparative study of an anodic recirculation system based on electrochemical pump in proton exchange membrane fuel cell". In: *International Journal of Hydrogen Energy* 43.42 (2018), pp. 19691–19703. ISSN: 0360-3199.

[104] Ludwig Lipp. "Electrochemical Hydrogen Compressor". In: *Web* (Jan. 2016). DOI: 10 . 2172 / 1235441. URL: https://www.osti.gov/biblio/1235441.

[105] A. Rico- Zavala et al. "Nanocomposite membrane based on SPEEK as a perspectives application in electrochemical hydrogen compressor". In: *International Journal of Hydrogen Energy* 44.10 (2019), pp. 4839–4850. ISSN: 0360-3199. DOI: https://doi.org/10.1016/j.ijhydene.2018.12.174.

[106] YanMing Hao et al. "Characterization of an electrochemical hydrogen pump with internal humidifier and dead-end anode channel". In: *International Journal of Hydrogen Energy* 41.32 (2016), pp. 13879–13887. ISSN: 0360-3199. DOI: https://doi.org/10.1016/j.ijhydene.2016.05.160.

[107] S.A. Grigoriev et al. "Description and characterization of an electrochemical hydrogen compressor/concentrator based on solid polymer electrolyte technology". In: *International Journal of Hydrogen Energy* 36 (2011), pp. 4148–4155. ISSN: 0360-3199.

[108] J.L. Pineda-Delgado et al. "Effect of relative humidity and temperature on the performance of an electrochemical hydrogen compressor". In: *Applied Energy* 311 (2022), p. 118617. ISSN: 0306-2619.

[109] Maria Nordio et al. "Experimental and modelling study of an electrochemical hydrogen compressor". In: *Chemical Engineering Journal* 369 (2019), pp. 432–442. ISSN: 1385-8947. DOI: https://doi.org/10.1016/j.cej.2019.03.106.

[110] Nilesh V. Dale et al. "Modeling and analysis of electrochemical hydrogen compression". In: *NHA Annual Hydrogen Conference*. 2008.

[111] S.A. Grigoriev et al. "Characterization of PEM Electrochemical Hydrogen Compressors". In: *Kurchatov Institute - Russia* (2008).

[112] Kelly A. Perry, Glenn A. Eisman, and Brian C. Benicewicz. "Electrochemical hydrogen pumping using a high-temperature polybenzimidazole (PBI) membrane". In: *Journal of Power Sources* 177.2 (2008), pp. 478–484. ISSN: 0378-7753.

[113] Benjamin L. Kee et al. "Thermodynamic Insights for Electrochemical Hydrogen Compression with Proton-Conducting Membranes". In: *Membranes* 9.7 (2019). ISSN: 2077-0375.

[114] M.T. Nguyen et al. "Characterisation of a electrochemical hydrogen pump using electrochemical impedance spectroscopy". In: *Journal of Applied Electrochemistry* 41 (2011). ISSN: 1572-8838.

[115] G. Sdanghi et al. "Feasibility of Hydrogen Compression in an Electrochemical System: Focus on Water Transport Mechanisms". In: *Fuel Cells* 20.3 (2020), pp. 370–380.

[116] Alfredo Iranzo et al. "Influence of the dwell time in the polarization hysteresis of polymer electrolyte membrane fuel cells". In: *Electrochimica Acta* 426 (2022), p. 140809. ISSN: 0013-4686. DOI: https://doi.org/10.1016/j.electacta.2022.140809.

[117] D. Bahena et al. "Electrochemical Noise Chaotic Analysis of NiCoAg Alloy in Hank Solution". In: *International Journal of Corrosion* 2011 (2011), p. 491564.

[118] Maria Trzaska and Zdzislaw Trzaska. "Chaotic oscillations in fractional-order nonlinear circuit models of bipolar pulsed electroplatings". In: *2011 20th European Conference on Circuit Theory and Design (ECCTD)*. 2011, pp. 166–169. DOI: 10.1109/ECCTD.2011.6043308.

[119] A. Guderian et al. "Electrochemical Chaos Control in a Chemical Reaction: Experiment and Simulation". In: *The Journal of Physical Chemistry A* 102.26 (1998), pp. 5059–5064. DOI: 10.1021/jp980997g.

[120] J. M. Cruz, M. Rivera, and P. Parmananda. "Experimental observation of different types of chaotic synchronization in an electrochemical cell". In: *Phys. Rev. E* 75 (3 Mar. 2007), p. 035201. DOI: 10.1103/PhysRevE.75.035201.

[121] Arturo Buscarino, Luigi Fortuna, and Mattia Frasca. *Essentials of Nonlinear Circuit Dynamics with MATLAB®and Laboratory Experiments*. CRC Press, 2017.

[122] Simone Giannerini and Rodolfo Rosa. "Caos, statistica e metodi di ricampionamento". In: *Statistica* 62.3 (Oct. 2007), pp. 359–378.

[123] Ricardo Mañé. "On the dimension of the compact invariant sets of certain non-linear maps". In: *Dynamical Systems and Turbulence, Warwick 1980*. Ed. by David Rand and Lai-Sang Young. Berlin, Heidelberg: Springer Berlin Heidelberg, 1981, pp. 230–242. ISBN: 978-3-540-38945-3.

[124] Floris Takens. "Detecting strange attractors in turbulence". In: *Dynamical Systems and Turbulence, Warwick 1980*. Ed. by David Rand and Lai-Sang Young. Berlin, Heidelberg: Springer Berlin Heidelberg, 1981, pp. 366–381. ISBN: 978-3-540-38945-3.

[125] J.P. Eckmann and D. Ruelle. *Essentials of Nonlinear Circuit Dynamics with MATLAB®and Laboratory Experiments*. Springer New York, 2004. DOI: 10.1007/978-0-387-21830-4_17.

[126] Shapour Mohammadi. *LYAPROSEN: MATLAB function to calculate Lyapunov exponent*. 2009.

[127] Rainer Hegger and Holger Kantz. "Improved false nearest neighbor method to detect determinism in time series data". In: *Phys. Rev. E* 60 (4 Oct. 1999), pp. 4970–4973. DOI: 10.1103/PhysRevE.60.4970.

[128] Alexandros Leontitsis. https://www.mathworks.com/matlabcentral/mlc-downloads/downloads/submissions/1597/versions/1/previews/phasespace.m/index.html. [Online]. 2001.

[129] I. Podluby. *Fractional Differential Equations: An Introduction to Fractional Derivatives, Fractional Differential Equations, to Methods of Their Solution and Some of Their Applications*. Academic Press, 1998.

[130] Phani Teja Bankupalli et al. "Fractional order modeling and two loop control of PEM fuel cell for voltage regulation considering both source and load perturbations". In: *International Journal of Hydrogen Energy* 43.12 (2018), pp. 7518–7536.

[131] Xueqin Lü et al. "Dynamic Modeling and Fractional Order PID Control of PEM Fuel Cell". In: *Int. J. Electrochemical Science* 12 (2017), pp. 7518–7536.

[132] Riccardo Caponetto et al. "Fuel Cell Fractional-Order Model via Electrochemical Impedance Spectroscopy". In: *Fractal and Fractional* 5.1 (2021).

[133] R. Caponetto and G. Dongola. "A numerical approach for computing stability region of FO-PID controller". In: *Journal of the Franklin Institute* 350.4 (2013), pp. 871–889. DOI: 10.1016/j.jfranklin.2013.01.017.

[134] R. Caponetto, L. Fortuna, and D. Porto. "Parameter tuning of a non integer order PID controller". In: *Proceedings of the fifteenth international symposium on mathematical theory of networks and systems MTNS2002, Notre Dame, Indiana* (2002).

[135] Dan Eliezer. "The Behavior of 316 Stainless Steel in Hydrogen". In: *Journal of Materials Science* 19 (May 1984), p. 1540. DOI: 10.1007/BF00563051.

[136] Xiao Zhou, Ali Tehranchi, and William A. Curtin. "Mechanism and Prediction of Hydrogen Embrittlement in fcc Stainless Steels and High Entropy Alloys". In: *Phys. Rev. Lett.* 127 (17 Oct. 2021), p. 175501. DOI: 10.1103/PhysRevLett.127.175501. URL: https://link.aps.org/doi/10.1103/PhysRevLett.127.175501.

[137] T. Ogata. "Influence of high pressure hydrogen environment on tensile and fatigue properties of stainless steels at low temperatures". In: *AIP Conference Proceedings* 1435.1 (2012), pp. 39–46. DOI: 10.1063/1.4712078.

[138] Tomohiko Omura and Jun Nakamura. "Hydrogen Embrittlement Properties of Stainless and Low Alloy Steels in High Pressure Gaseous Hydrogen Environment". In: *ISIJ International* 52.2 (2012), pp. 234–239. DOI: 10.2355/isijinternational.52.234.

[139] A. Arvay. "Proton Exchange Membrane Fuel Cell Modeling and Simulation using Ansys Fluent". In: *Arizona State University - USA* (2011).

[140] Joseph Baker, Yunho Hwang, and Chunsheng Wang. "Design of Gas Channels for a Carbon Dioxide Electrochemical Compressor". In: *International Compressor Engineering Conference* Paper 2616 (2018).

[141] https://www.acciaiterni.it/wp-content/uploads/2017/07/316_NEW.pdf. [Online]. 2022.

[142] http://www.ambrogiocolombo.it/prodotto/inox-aisi-316/. [Online]. 2022.

[143] https://www.gruppolimainox.it/index.php/attivita/114-pages/acciai-inossidabili/designazione/317-aisi-316. [Online]. 2022.

[144] https://www.efunda.com/Materials/alloys/stainless_steels/show_stainless.cfm?ID=AISI_Type_316&prop=all&Page_Title=AISI%20Type%20316. [Online]. 2022.

[145] G. Mirone. "Role of stress triaxiality in elastoplastic characterization and ductile failure prediction". In: *Engineering Fracture Mechanics* 74.8 (2007), pp. 1203–1221. ISSN: 0013-7944.

[146] Jian Peng et al. "Effect of Stress Triaxiality on Plastic Damage Evolution and Failure Mode for 316L Notched Specimen". In: *Metals* 9.10 (2019). ISSN: 2075-4701.

[147] Renato Giovannozzi. *Costruzione di macchine, Vol. 1.* Pàtron, 1980.

[148] P. Righettini. https://docplayer.it/57127739-Progettazione-funzionale-di-sistemi-meccanici-e-meccatronici-camme-pressioni-di-contatto.html. [Online]. 2022.

[149] https://web.archive.org/web/20210301070357/http://mechdesigner.support/index.htm?contact-fatigue-cams-cam-followers.htm. [Online]. 2022.

[150] Emanuela Privitera et al. "Impact of Geometry on a Thermal-Energy Storage Finned Tube during the Discharging Process". In: *Energies* 15.21 (2022). ISSN: 1996-1073. DOI: 10.3390/en15217950.

[151] Ali Abedin. "A Critical Review of Thermochemical Energy Storage Systems". In: *The Open Renewable Energy Journal* 4 (Aug. 2011). DOI: 10.2174/1876387101004010042.

[152] https://www.dlr.de/tt/Portaldata/41/Resources/dokumente/ess_2013/ESS2013_DLR_Speicherrelevanz_fuer_CSP_Herrmann_Flagsol.pdf. [Online]. 2022.

[153] Belén Zalba et al. "Review on thermal energy storage with phase change: materials, heat transfer analysis and applications". In: *Applied Thermal Engineering* 23.3 (2003), pp. 251–283. ISSN: 1359-4311. DOI: https://doi.org/10.1016/S1359-4311(02)00192-8.

[154] Murat M. Kenisarin. "High-temperature phase change materials for thermal energy storage". In: *Renewable and Sustainable Energy Reviews* 14.3 (2010), pp. 955–970. ISSN: 1364-0321. DOI: https://doi.org/10.1016/j.rser.2009.11.011.

[155] Francis Agyenim et al. "A review of materials, heat transfer and phase change problem formulation for latent heat thermal energy storage systems (LHTESS)". In: *Renewable and Sustainable Energy Reviews* 14.2 (2010), pp. 615–628. ISSN: 1364-0321. DOI: https://doi.org/10.1016/j.rser.2009.10.015.

[156] Saman Gunasekara et al. "Thermal Energy Storage Materials (TESMs)—What Does It Take to Make Them Fly?" In: *Crystals* 11 (Oct. 2021), p. 1276. DOI: 10.3390/cryst11111276.

[157] S. Jegadheeswaran and Sanjay D. Pohekar. "Performance enhancement in latent heat thermal storage system: A review". In: *Renewable and Sustainable Energy Reviews* 13.9 (2009), pp. 2225–2244. ISSN: 1364-0321. DOI: https://doi.org/10.1016/j.rser.2009.06.024.

[158] Rainer Tamme et al. "Latent heat storage above 120°C for applications in the industral process heat sector and solar power generation". In: *International Journal of Energy Research - INT J ENERG RES* 32 (Mar. 2008), pp. 264–271. DOI: 10.1002/er.1346.

[159] R. Al Shannaq and M.M. Farid. "10 - Microencapsulation of phase change materials (PCMs) for thermal energy storage systems". In: *Advances in Thermal Energy Storage Systems*. Ed. by Luisa F. Cabeza. Woodhead Publishing Series in Energy. Woodhead Publishing, 2015, pp. 247–284. ISBN: 978-1-78242-088-0. DOI: https://doi.org/10.1533/9781782420965.2.247.

[160] Kaixin Dong et al. "Optimized Preparation of a Low-Working-Temperature Gallium Metal-Based Microencapsulated Phase Change Material". In: *ACS Omega* 7.32 (2022), pp. 28313–28323. DOI: 10.1021/acsomega.2c02801.

[161] https://seeds.mcip.hokudai.ac.jp/en/view/208/. [Online]. 2022.

[162] Francis Agyenim, Philip Eames, and Mervyn Smyth. "A comparison of heat transfer enhancement in a medium temperature thermal energy storage heat exchanger using fins". In: *Solar Energy* 83.9 (2009), pp. 1509–1520. ISSN: 0038-092X. DOI: https://doi.org/10.1016/j.solener.2009.04.007.

[163] Uroš Stritih. "An experimental study of enhanced heat transfer in rectangular PCM thermal storage". In: *International Journal of Heat and Mass Transfer* 47.12 (2004), pp. 2841–2847. ISSN: 0017-9310. DOI: https://doi.org/10.1016/j.ijheatmasstransfer.2004.02.001.

[164] M. Johnson et al. "High Temperature Latent Heat Thermal Energy Storage Integration in a Co-gen Plant". In: *Energy Procedia* 73 (2015). 9th International Renewable Energy Storage Conference, IRES 2015, pp. 281–288. ISSN: 1876-6102. DOI: https://doi.org/10.1016/j.egypro.2015.07.689.

[165] https://www.chester-project.eu/about-chester/the-project/. [Online]. 2022.

[166] https://www.chester-project.eu/news/laboratory-preparation-and-status-of-the-chest-technology/. [Online]. 2022.

[167] V. Alexiades and A.D. Solomon. *Mathematical Modeling of Melting and Freezing Processes (1st ed.)* Routledge, 1993.

[168] https://www.afs.enea.it/project/neptunius/docs/fluent/html/th/node349.htm. [Online]. 2022.

[169] https://www.afs.enea.it/project/neptunius/docs/fluent/html/th/node107.htm. [Online]. 2022.

[170] Alen Cukrov et al. “A SOLUTION TO STEFAN PROBLEM USING EULERIAN TWO FLUID VOF MODEL”. In: *Brodogradnja: Teorija i praksa brodogradnje i pomorske tehnike* 72.4 (2021), pp. 141–164.

Appendix A

Matlab script for Two-Phase 1-D Stefan Problem

A.1 Input data

```
% INPUT DATA %
cL = 3.31; % specific heat - liquid phase [J/(g*K)]
cS = 1.76; % specific heat - solid phase [J/(g*K)]
kL = 0.0059; % thermal conductivity - liquid phase [W/(cm*K)]
kS = 0.0216; % thermal conductivity - solid phase [W/(cm*K)]
rho_L = 1.460; % density - liquid phase [g/cm^3]
rho_S = 1.460; % density - solid phase [g/cm^3]
L  = 251.21; % latent heat [J/g]
Tm = 32; % melting temperature [Celsius degrees]
TL = 90; % wall temperature [Celsius degrees]
TS = 25; % initial temperature [Celsius degrees]
time_profiles = [36000 108000 216000]; % for T(x) graph [s]
points = [0.05 0.10 0.15]; % for T(t) graph [m]
t_max = 360000; % T(t) graph limit [s]
```

A.2 Newton-Raphson function

```
function [y] = Newton_Raphson(x, f, x0)
%   x is the variable
%   f is the transcendental equation
%   x0 is the initial approximation

% the derivative of the transcendental equation
g = diff(f);
epsilon = 10^(-20);

for i = 1 : 100
    % the value of the transcendental equation at x0
    f0 = vpa(subs(f, x, x0));

    % the value of the derivative of the transcendental equation at x0
    f0_der = vpa(subs(g, x, x0));

```

```
    % Newton_Raphson formula
    y = x0 - f0 / f0_der;
    err = abs(y - x0);

    % checking the amount of error at each iteration
    if err < epsilon
        break
    end

    x0 = y;
end

% displaying up to required decimal places
y = double(y - rem(y, epsilon));

end
```

A.3 Two-Phase 1-D Stefan Problem

```
clc
close all
clear

% INPUT DATA %
input_data

% PRELIMINARY CALCULATIONS %
dTL = TL - Tm;
dTS = Tm - TS;
StL = cL * dTL / L; % Stefan number - liquid phase
StS = cS * dTS / L; % Stefan number - solid phase
alpha_L = kL / (rho_L * cL); % diffusivity - liquid phase [cm^2/s]
alpha_S = kS / (rho_S * cS); % diffusivity - solid phase [cm^2/s]
ni = sqrt(alpha_L / alpha_S);

% NEWMANN SOLUTION  %
y0 = sqrt(StL / 2); % initial approximation
syms y
% transcendental equation
f = StL/(exp(y^2)*erf(y))-StS/(ni*exp(ni^2*y^2)*erfc(ni*y))-y*sqrt(pi);
y0 = Newton_Raphson(y, f, y0);
if isnan(y0)
    fprintf('Error: the Root by Newton-Raphson method is %.20f\n', y0);
    fprintf('Please, try to modify the initial approximation of y0\n');
    return
end

% CALCULATION OF X(t):
% frontier position at time t [cm]
Xt = @(t) 2*y0*sqrt(alpha_L*t);

% CALCULATION OF t_melt(x):
% time needed for melting front at x coordinate [s]
t_melt = @(x) x^2/(4*y0^2*alpha_L);

% CALCULATION OF T(x,t): temperature field [Celsius degrees]
% in the liquid region (0<x<X(t))
Txt_L = @(x,t) TL-(TL-Tm)*erf(x/(2*sqrt(alpha_L*t)))/erf(y0);
% in the solid region (x>X(t))
Txt_S = @(x,t) TS+(Tm-TS)*erfc(x/(2*sqrt(alpha_S*t)))/erfc(y0*ni);
```

```
42
43 %%%% PLOTS %%%%
44 FontSize_legend = 21;
45 FontSize_axis = 21;
46 FontSize_axis_title = 28;
47 FontSize_title = 28;
48 Line_width = 1.5;
49
50 % transcendental equation UNIQUE ROOT
51 s = 0 : 0.0001 : 1;
52 fs = StL./(exp(s.^2).*erf(s))-StS./(ni*exp(ni^2.*s.^2).*erfc(ni.*s))-s.*sqrt
       (pi);
53 figure
54 hold on
55 grid on
56 xlim([0 1])
57 ylim([-10 60])
58 ax = gca;
59 ax.FontSize = FontSize_axis;
60 plot(s, fs, "black", 'LineWidth',Line_width)
61 yline(0, "g", 'LineWidth',Line_width)
62 xline(y0, "r", 'LineWidth',Line_width)
63 plot(y0, 0, "b*", 'LineWidth',Line_width)
64 xlabel("\lambda", 'FontSize', FontSize_axis_title)
65 ylabel("f(\lambda)", 'FontSize', FontSize_axis_title)
66 legend("$f(\lambda)$", "$y=0$", "$x=\lambda_0$", 'intersection', '
       Interpreter', 'latex', 'Location', "northeast", 'FontSize',
       FontSize_legend)
67 title("Unique solution of two-phase 1D StSoCefan problem", 'FontSize',
       FontSize_title)
68
69 % Temperature profiles at three times
70 space = 0 : 0.001 : 100; %cm
71 Tx_time_profiles = zeros(length(space), length(time_profiles));
72 name_plot = strings(1, length(time_profiles));
73 figure
74 hold on
75 grid on
76 for j = 1 : length(time_profiles)
77     for i = 1 : length(space)
78         if space(i) <= Xt(time_profiles(j)) % space <= frontier position at
               time t
79             Tx_time_profiles(i, j) = Txt_L(space(i), time_profiles(j));
80         else
81             Tx_time_profiles(i, j) = Txt_S(space(i), time_profiles(j));
82         end
83     end
84     legend('Location', "northeast", 'FontSize', FontSize_legend)
85     name_plot(j) = join(["T(x) at t =", num2str(time_profiles(j)/3600), "
           hours"]);
86     plot(space/100, Tx_time_profiles(:, j), 'DisplayName', name_plot(j), '
           LineWidth',Line_width)
87 end
88 xlim([0 1])
89 ylim([TS-5 TL])
90 ax = gca;
91 ax.FontSize = FontSize_axis;
92 yline(Tm, 'DisplayName', 'Melting temperature', 'LineWidth',Line_width)
93 xlabel("x coordinate [m]", 'FontSize', FontSize_axis_title)
94 ylabel("Temperature [Celsius degrees]", 'FontSize', FontSize_axis_title)
95 title("Temperature vs space for two-phase 1D Stefan problem", 'FontWeight',
       'bold', 'FontSize', FontSize_title);
```

```
96
97  % Temperature histories at three points
98  time = 0 : 1 : t_max;
99  points = points * 100; %cm
100 t_melt_points = zeros(1, length(points));
101 T_points_t = zeros(length(time), length(points));
102 figure
103 hold on
104 grid on
105 for j = 1 : length(points)
106     t_melt_points(j) = t_melt(points(j)); % in seconds
107     for i = 1 : length(time)
108         if time(i) <= t_melt_points(j)
109             T_points_t(i, j) = Txt_S(points(j), time(i));
110         else
111             T_points_t(i, j) = Txt_L(points(j), time(i));
112         end
113     end
114     legend('Location', "northwest", 'FontSize', FontSize_legend)
115     name(j) = join(["T(t) at x =", num2str(points(j)), "cm"]);
116     plot(time/3600, T_points_t(:, j), 'DisplayName', name(j), 'LineWidth',
        Line_width)
117 end
118 xlim([0 t_max/3600])
119 ylim([TS-5 TL])
120 ax = gca;
121 ax.FontSize = FontSize_axis;
122 yline(Tm, 'DisplayName', 'Melting temperature', 'LineWidth',Line_width)
123 xlabel("Time [hours]", 'FontSize', FontSize_axis_title)
124 ylabel("Temperature [Celsius degrees]", 'FontSize', FontSize_axis_title)
125 title("Temperature vs time for two-phase 1D Stefan problem", 'FontSize',
    FontSize_title)
126
127 % Frontier position vs time
128 figure
129 hold on
130 grid on
131 plot(time/3600, Xt(time)/100, 'LineWidth',Line_width)
132 xlim([0 t_max/3600])
133 ylim([0 1])
134 ax = gca;
135 ax.FontSize = FontSize_axis;
136 xlabel("Time [hours]", 'FontSize', FontSize_axis_title)
137 ylabel("Melting frontier [m]", 'FontSize', FontSize_axis_title)
138 title("Frontier position vs time for two-phase 1D Stefan problem", 'FontSize
    ', FontSize_title)
```